Characteristics of Foreshocks and Short Term Deformation in the Source Area of Major Earthquakes

Peter Molnar

Massachusetts Institute of Technology
77 Massachusetts Avenue
Cambridge, Massachusetts 02139

USGS CONTRACT NO. 14-08-0001-17759
Supported by the EARTHQUAKE HAZARDS REDUCTION PROGRAM

OPEN-FILE NO.81-287

U.S. Geological Survey
OPEN FILE REPORT

This report was prepared under contract to the U.S. Geological Survey and has not been reviewed for conformity with USGS editorial standards and stratigraphic nomenclature. Opinions and conclusions expressed herein do not necessarily represent those of the USGS. Any use of trade names is for descriptive purposes only and does not imply endorsement by the USGS.

/

Appendix A

A Study of the Haicheng Foreshock Sequence

By Lucile Jones, Wang Biquan and Xu Shaoxie

(English Translation of a Paper Published in
Di Zhen Xue Bao (Journal of Seismology), 1980.)

Abstract

We have examined the locations and radiation patterns of the foreshocks to the 4 February 1978 Haicheng earthquake. Using four stations, the foreshocks were located relative to a master event. They occurred very close together, no more than 6 kilometers apart. Nevertheless, there appear to have been two clusters of foreshock activity. The majority of events seem to have occurred in a cluster to the east of the master event along a NNE-SSW trend. Moreover, all eight foreshocks that we could locate and with a magnitude greater than 3.0 occurred in this group. There also appears to be a second cluster of foreshocks located to the northwest of the first. Thus it seems possible that the majority of foreshocks did not occur on the rupture plane of the mainshock, which trends WNW, but on another plane nearly perpendicualr to the mainshock plane. This inference is supported by differences among the radiation patterns of the foreshocks.

We also examined the radiation patterns of the foreshocks, primarily through the amplitude ratios of P and S waves (Ap/As) recorded at each station. While the ratios were relatively constant at the more distant (Δ=100-200 kilometers) stations, two very different waveforms were recorded throughout the sequence at Yingkou (Δ=20 kilometers). Calculations of the amplitude ratios expected from the (not very different) fault plane solutions of the mainshock and some of the largest foreshocks showed that two different waveforms should be recorded at Yingkou. A definite correlation could not be made between the two mechanisms and the different location clusters.

1) Introduction

The successful prediction of the 4 February, 1975 Haicheng earthquake (M=7.3) was due, in a large part, to the occurrence of a large foreshock sequence of more than 500 events in the four days preceding the mainshock (Wu, 1976). Such a large sequence is a rare event - indeed, the Haicheng series is the only large foreshock sequence to have been well recorded - and we cannot hope that many other mainshocks will have such sequences.
Many large earthquakes are preceded by a few foreshocks (Jones and Molnar, 1979) but so far we have been able to recognize them only in hindsight. To increase the number of earthquakes that can be successfully predicted, we need to learn how to differentiate foreshocks from "normal" earthquake swarms before the mainshock occurs and when the shear number of events is not an overpowering consideration as it was at Haicheng. But precisely because of its great length, the Haicheng sequence provides a unique opportunity to study this problem. The large number of events allows the characteristics of this foreshock sequence to be seen more clearly. These characteristics could then be compared with those of earthquake swarms to the benefit of all people engaged in earthquake prediction research. Thus, the first part of the Chinese-American exchange in earth sciences has been a study of the Haicheng foreshock sequence resulting in this report.

There are two purposes of this research. There is, of course, the obvious application to earthquake prediction, attempting to determine characteristics of foreshocks that will allow them to be recognized before the mainshock occurs. This research also has application to the study of the earthquake mechanism, because the foreshocks are evidence of deformation of the earth occurring prepratory to the complete rupture. For both purposes, we have researched two primary characteristics of this foreshock sequence, the relative locations of the events and their radiation patterns - the latter principally by consideration of the ratio of the amplitudes of the P and S waves. Other characteristics of the sequence are studied in another paper (Xu et al, 1979).

2) Data and Techniques

A map showing most of the seismograph stations in operation in the Haicheng area during early 1975 is shown in Figure 1. All stations had three-component, short period instruments. During the two days before the mainshock, the seismographs were operated at a speed of 12cm/min. so that arrival times could be read easily with an uncertainty of less than 0.1 seconds. The amplification of all of the instruments was approximately 10^5.

The events were located relative to a master event. This event was chosen as master because when it was located using P arrivals at five stations (all except Lu Da whose clock was suspect), its residuals were all less than .03 seconds. P arrivals at four stations were used for the relative locations and the origin time of each event was assumed to differ from that of the master event by the average difference in arrival times of the event and the master. Four locations were found for each event by solving the four sets of three equations uniquely; the average was taken as the location of the event and the range of values was taken to be the error. The four stations used were Yingkou, FuXun, Zhuang He and Jin Zhou to supply maximum control on the locations.

3) Results of Locations

Although more than 500 foreshocks occurred, most were too small to be recorded at any stations except the nearest, Yingkou station. We were able to locate 34 events all of which occurred in the 26 hours immediately preceding the mainshock. Their locations relative to the master event and the errors in these locations are listed in Table 1. The relative epicenters are plotted in Figure 2.

All of the foreshocks occurred very close together, no more than six kilometers apart. The data in Figure 2 suggest that the foreshocks occurred in two clusters although it is possible that the apparent clustering is due to errors in the data. The majority of events appear to have occurred in a cluster to the east of the master event along a NNE-SSW trend (labeled A in Figure 2). Moreover, all eight foreshocks that were located and had a magnitude greater then 3.0 were located in group A. However, there also

appears to be a second cluster of foreshocks located to the northwest of the first (lableled B in Figure 2).

The rupture plane of the mainshock upon which most of the aftershocks occurred trends west-northwest, (Wu, 1976), not north-northeast like the main trend we found for the foreshocks. Because of their small size of the events, the fault plane solutions of the foreshocks are not well constrained and several researchers have determined somewhat different solutions (Figure 3). Nevertheless, all are roughly similar to that of the mainshock (Figure 3d). However, one can see from the solutions, that faulting along the WNW plane of the mainshock or the NNE plane suggested by our foreshock locations would produce similar fault solutions. Fault structures with both WNW and NNE trends are present in the Haicheng area. Moreover, although most of the aftershocks occurred in a WNW zone, a few defined a zone of activity trending NNE from the epicenter of the mainshock. Thus it seems possible that while some of the foreshocks occurred along the mainshock plane (group B), the majority and the largest of the foreshocks might have occurred along a plane roughly perpendicular to that of the mainshock.

To further consider this question, we examined the depth distribution of the foreshocks perpendicular both to the "foreshock plane" (thus, projected along N73°W) and the mainshock plane (projected along N28°E) (Figure 4). The most obvious feature of these plots is the apparent WNW dip of the NNE plane suggesting that the group B earthquakes may have occurred on a deeper part of the same plane on which the group A events occurred. However, the depths are not well constrained, and in general have errors three times as large as the horizontal directions (see Table 1). Thus, this apparent result is not dependable. Since the only nearby station, Yingkou (Δ=20km), is located almost due west from the foreshocks, this apparent westward dip could be due in part to its influence. In general, however, the A group of foreshocks appear to be located along a NNE trending, approximately vertical plane within a very small depth range and the B group occurs in a more dispersed pattern but in the direction of the mainshock from the A group.

b) Amplitude Ratios

Since it is often assumed that all of the events within a foreshock sequence have the same mechanisms, many researchers have examined the question of whether or not the ratio of the amplitudes of the P and S waves varies within a sequence (Jin et al, 1976; Lindh et al, 1978; Jones and Molnar, 1979; Bolt et al, 1977; Engdahl and Kissinger, 1977; Chen et al,1978) with differring results. Again, the Haicheng sequence, because of the large number of events and stations, provides a good opportunity to study this question. The amplitudes of the P and S waves of the foreshocks in the last day recorded at all six stations are shown in Figures 5 and 6 (events occurring before the largest foreshock in Figure 5 and after in Figure 6). The average ratios and standard deviations from them are listed for all stations in Table II.

For all stations except the nearest, Yingkou, the foreshock waveforms are very similar and the amplitude ratios relatively constant until the largest foreshock (M=4.7 at February 4 07^h50^m) occurred. After the largest foreshock occurred, the waveforms began to differ (for example see the two events recorded at Jin Zhou in Figure 7a, and two others at Fu Xun in Figure 7b) and the ratios became more dispersed (Figure 6).

The amplitude ratios recorded at Yingkou differed even more markedly than those at the more distant stations. Through the entire foreshock sequence, two definitely different waveforms were recorded. One had a relatively large, sharp P wave arrival while the other had a much smaller one (Figure 8). Within these two groups, the amplitude ratio were relatively constant and stayed so after the largest foreshock occurred. It proved impossible to correlate the two waveforms at Yingkou with events at other stations. In general, if an event was large enough to be recorded at the distant stations, the arrivals at Yingkou were too large and the waveforms were clipped. Six events recognizable as small or large P events were located (see Table I) but at each of the other stations, only two or three of those had amplitude ratios recorded so no reliable comparison of radiation patterns recorded at Yingkou and other stations could be made.

4) Discussion

Since both the locations and amplitude ratios suggest that there were two types of foreshock activity, we hoped to find a correlation between the two groupings. The obvious assumption was that the foreshocks indeed occur on two planes resulting in two different waveforms at Yingkou. Unfortunately, while the possibility of a relationship between the two phenomena exists, the results are by no means conclusive.

The first step was to compare the recorded amplitude ratios with those expected from the fault plane solutions determined for the mainshock and foreshocks using the double-couple formula of Ben-Menahem et al, (1965) (Table IV). We included the effect of the angle of incidence at the surface and instrument response but since the velocity structure of the Haicheng area is not well known, we could not examine the possibility of refraction changing the angle of incidence. Also, the fault plane solutions of the foreshocks and mainshock are not very well constrained so there are a range of possible amplitude ratios. The amplitude ratios at Zhuang He and Cao He Zhuan were particularly sensitive to variations in orientation of the focal planes and location. Thus the calculated ratios can be used only as a guide. Fortunately, however, at Yingkou where we recorded the two very different mechanisms, the calculated amplitude ratios are sensitive to focal plane variations but not to changes in location. Of all the fault plane solutions determined for the foreshocks and mainshock, the fault plane solution for the mainshock (Wu et al, 1976) agreed best with the small P values and that for the largest foreshock, determined by Gu (1976), was the best fit for the large P events. Thus, if the two radiation patterns were the result of two fault planes, the Yingkou response would indicate that the large P events correspond to the A cluster events and small P to the B cluster.

Several pieces of circumstantial evidence support this supposition. As mentioned before, the ratios at the other stations were more dispersed after the largest foreshock occurred which was when more events were located in the B cluster. As well, in determining the fault plane solutions, the station at Lu Da in the southwest quadrant was crucial in determining the exact placement of

the NNE plane. We examined the first motion at Lu Da for several of the largest foreshocks and found that while in most cases the first motion was dilational (causing the NNE plane to be vertical or dip to the northwest), it was compressional (resulting in a southeasterly dip) for the mainshock and one B group foreshock (no. 34, Table I). Another piece of supporting evidence is that all the large P events had S-P times at Yingkou of 2.5 or 2.6 seconds which is the S-P time of the southern end of the A cluster. The S-P times of the small P events, on the other hand, were quite dispersed ranging from 2.2 to 2.8 seconds.

In spite of these suggestive data, a direct correlation between the mechanisms and the clusters could not be made. The six events with definite large P of small P radiation patterns that were located do not correlate with the clusters - two each of the large P and small P events are in the A cluster and one each in the B cluster (Table I). It is possible that the interlocking of the planes allows different faulting mechanisms to occur very near to each other, but it is also possible that the errors in the data have created illusionary relationships.

5) Conclusion

This report has considered the locations and mechanisms of the foreshocks of the Haicheng earthquake. The foreshocks all occurred within 6 km of each other. It is possible though not definite that the foreshocks occurred in two clusters of activity, the majority not occurring on the rupture plane of the mainshock but on another plane nearly perpendicular to the plane of the mainshock. The ratios of the P and S amplitudes was less constant than those of a nearby swarm, especially after the largest foreshock had occurred. At the nearest station, two very different waveforms were recorded both before and after the largest foreshocks. Thus the P/S ratio does not seem to be an accurate means of identifying foreshocks as has been previously suggested. A definite correlation could be made between the two mechanisms and the different location clusters.

Figure 1. The locations of the Haicheng foreshock sequence and the seismograph stations in the Haicheng, Liaoning Province area.

Figure 2. The epicenters of the foreshocks to the 1975 Haicheng earthquake relative to the foreshock occurring at February 03 19^h13^m. The error bars show the standard deviation of the locations. The events shown by open circles had a standard deviation greater than 2 km.

Figure 3. Fault plane solutions determined for the February, 1975, Haicheng mainshock (a) and for the foreshocks (b,c,d,e) by Wu et al (1976), (b), Jin et al (1976), (c,d), Gu et al, (1976), (e).

Figure 4a. The depth distribution of the foreshocks to the 1975 Haicheng earthquake projected along a plane trending N73°W. Closed circles represent events located in the A cluster and open circles represent events located in the B cluster. Crosses represent events with an epicentral error greater than 2 km.

Figure 4b. The depth distribution of the foreshocks to the 1975 Haicheng earthquake projected along a plane trending N28°E. Symbols as in figure 4a.

Figure 5. The amplitudes of the P waves versus the amplitudes of the S waves for the foreshocks to the Haicheng earthquake that occurred before the largest foreshock recorded at Yingkou (a), Fu Xun (f), Zhuang He (b), Lu Da (d), Cao He Zhuan (e) and Jin Zhou (c).

Figure 6. The amplitudes of the P waves versus the amplitude of the S waves for the foreshocks of the Haicheng earthquake that occurred after the largest foreshock recorded at Yingkou (a), Fu Xun (f), Zhuang He (b), Lu Da (d), Cao He Zhuan (e) and Jin Zhou (c).

Figure 7a. Seismograms for two foreshocks (Feb. 4 10:47 and 10:34) of the Haicheng earthquakes recorded at Jin Zhou.

b. Seismograms for two foreshocks (2/4 09:05 and 16:25) of the Haicheng earthquake recorded at Fu Xiin.

Figure 8. Seismograms for two foreshocks (4A 08:16 and 08:31) of the Haicheng earthquake recorded at Yinkou.

Figure 9. The epicenters of the Haicheng foreshocks relative to the foreshock occurring at February 03 19^h13^m as determined using both P and S waves.

References

1 Wu Kaitong, Yue Mingsheng, Wu Huanying, et al, Certain characteristics of the Haicheng earthquake (M=7.3) sequence, Acta Geophysica Sinica, Vol. 19, No. 2, p. 95-109, 1976.

2 Jones, L.M. and P. Molnar, Some characteristics of foreshocks and their possilbe relations to earthquake prediction and premonitory slip on faults, Journal of Geophysical Research, Vol. 84, No. B7, p. 3596-3608, 1979.

3 Xu Shaoxie, Wang Biquan, Lucile Jones, Ma Xiufang and Shan Fengwen, The Haicheng foreshock sequence and earthquake swarms, Acta Geophysica Sinica, in press.

4 Jin Yan, Zhao Yi, Chen Yong, Yang Jiaguan, and Zhou Yuru, A characteristic feature of the dislocation model of foreshocks of the Haicheng earthquake, Liaoning Province, Acta Geophysica Sinica, Vol. 19, No. 3, p. 156-164, 1976.

5 Gu Haoding, Chen Yuntai, Gao Xianglin, Zhao Yi, Focal Mechanism of the Haicheng, Liaoning Province, earthquake of Febraury 4, 1975, Acta Geophysica Sinica, Vol. 19, No. 4, p. 270-285, 1976.

6 Chen Rong, Consistency of focal mechanism as a new parameter in describing seismic activity, Acta Geophysica Sinica, Vol. 21, No. 3, p. 142-159, 1978.

7 Bolt, B.A., J. Stifler, and R. Uhrhammer, The Briones Hills earthquake swarm of January 8, 1977 Contra Costa County, California, Bull. Seismol. Soc. Amer., 67, p. 1555-1564, 1977.

8 Engdahl, E.R., and C. Kisslinger, Seismological precursors to a magnitude 5 earthquake in the central Aleutian Islands, J. Phys. Earth, 25, S243-S250, 1977.

9 Lindh, A., G. Fuis, and C. Mantis, Foreshock amplitudes and fault plane changes: A new earthquake precursor? Science, 201, p. 56-59, 1978.

Articles 1, 4, 5, and 6 are in Chinese.

The foregoing text is a direct translation from Chinese of a paper that was written in May 1979 immediately upon completion of the first stage of the research. The locations were determined using only P arrivals from four stations and a simple program involving simultaneous equations on a HP-67 calculator. In September, 1979, the data (P and S arrivals for five stations) was brought to M.I.T. and the events were located using a computer program that computes relative locations and standard deviations using both P and S waves. These locations are shown in Figure 9. The two sets of locations do not differ greatly but some events have shifted enough to make the conjugate fault plane not quite as likely.

The reader has undoubtedly noticed that no mention was made of the mainshock location in this paper. At several of the local stations, the arrival of the mainshock was obscured by an aftershock so it was not possible to locate the mainshock in the same manner as the foreshocks. This fall, we relocated the mainshock with respect to the largest foreshock using what local data was available, data from the Chinese standard network and teleseismic data from ISC. We found that the hypocenters of the foreshock and mainshock were indistinguishable but the mainshock was definitely several kilometers deeper than the foreshock.

Table I. Locations of the foreshocks of the 04 Feb 1975 Haicheng earthquake

Hypocenters　　Depth　Error

No. Date　　表一、1975年2月4日海城地震前震位置 Mag.

编号	日期	Origin Time 发震时刻	震中位置 相对位置(KM) E-W	相对位置(KM) N-S	E°	N°	震源深度(KM)	定位误差 E-W	定位误差 N-S	定位误差 深度	震级	备注
			Relative									
1	3	19-13-39.5	0	0	122°49'27"	40°40'46"	14.9					
2		21-22-57.2	2.32	-2.04	51'07"	39'40"	11.5	.64	.55	2.0	3.1	
3		23-50-14.1	-.19	-.60	49'19"	40'27"	14.8	.05	.05	.2	1.6	
4		23-55-11.0	1.24	-1.18	50'20"	40'08"	12.9	.61	.52	1.71	1.5	
5		23-56-00.7	1.12	-1.28	50'15"	40'05"	14.1	31.2	1.1	3.5	1.5	
6	4	00-02-08.3	1.65	-.39	50'38"	40'33"	13.3	.5	.4	1.5	1.5	
7		00-58-50.2	2.11	-.12	50'58"	40'42"	12.8	.3	.2	.6	3.0	
8		02-18-16.0	.29	-.21	49'39"	40'39"	15.7	2.0	1.7	6.2	1.6	
9		03-22-14.6	.22	-2.03	49'36"	39'40"	14.8	1.0	.8	3.0	2.4	
10		03-54-43.1	1.86	.23	50'4)"	40'53"	12.9	.05	.05	.1		
11		04-17-51.8	-.44	-.37	49'08"	40'34"	16.6	2.1	1.8	6.5	1.7	
12		05-33-19.5	-.84	-.71	48'51"	40'23"	15.1	1.0	.8	2.9		
13		06-11-47.2	-1.18	-.11	48'36"	40'42"	16.6	.6	.5	1.9	2.8	
14		06-13-05.7	.93	-2.32	50'07"	39'31"	12.5	1.6	1.4	4.9	3.1	
15		06-53-20.8	1.67	-1.26	50'39"	40'05"	12.3	.8	.7	2.4	3.3	
16		06-58-21.0	2.63	-1.34	51'20"	40'03"	12.8	2.0	1.7	5.8	3.7	
17		07-14-33.3	3.00	1.19	51'36"	41'25"	12.4	1.1	.9	3.3	1.2*	
18		07-50-48.2	1.68	-1.69	50'37"	39'51"	13.2	.8	.7	2.5	4.7	
19		08-11-12.4	-.98	.95	48'45"	41'17"	15.3	1.4	1.2	4.4	1.3*	
20		08-13-04.8	.05	-.85	49'29"	40'18"	16.4	2.8	2.4	8.7	2.3	
21		08-14-45.4	-.35	-.29	49'12"	40'37"	15.6	.7	.6	2.0	1.5*	
22		08-57-14.7	1.57	-1.34	50'34"	40'03"	13.3	.7	.6	2.1	3.3	

23	4	09-17-54.1	-2.88	.24	47'23"	40'54"	18.7	.8	.7	2.6	1.3*	
24	4	09-36-42.6	-1.58	-3.82	48'28"	38'42"	15.5	.4	.4	1.3		
25		10-28-32.2	-2.46	1.48	47'41"	41'34"	17.9	.01	.01	.04	2.6	
26		10-33-29.7	-.33	1.06	49'13"	41'20"	14.6	.4	.3	1.2	1.8	
27		10-35-23.9	-.34	.19	51'07"	40'52"	11.8	1.0	.7	2.5	4.3	
28		10-47-19.1	1.34	-.20	50'25"	40'40"	12.7	1.2	1.0	3.4	2.0	
29		11-25-17.9	1.35	-2.85	50'25"	39'14"	13.0	.2	.2	.7	2.3	
30		13-08-06.5	.73	-2.05	49'58"	39'40"	13.5	.3	.2	.8	1.6	
31		13-53-58.7	3.24	-.42	51'46"	40'32"	11.5	.5	.4	1.4	0.9*	
32		14-56-24.4	.28	.69	49'39"	41'03"	13.8	1.5	1.3	4.7	1.1*	
33		16-23-13.7	1.64	-1.28	50'37"	40'05"	12.5	.4	.3	1.1	0.8*	
34		16-24-39.5	-.73	2.05	48'56"	41'52"	16.3	.3	.2	.9	2.6	

** 震级数据取自辽宁地震队所定震级（除 * 者外）

** Magnitude determined by Liaoning Seismology Bureau (except *)

* 带*号地震的震级取自营口台所定震级

* Magnitude determined by Yingkou Seismic Station.

Table II
Average recorded amplitude ratios and standard deviation

		Yingkou		Fuxun	Zhuang He	Luda	Caohezhuan	Jinzho
		Big P	Small P					
Before the largest foreshock	Ratio	0.30	0.08	0.36	0.28	0.20	1.01	0.11
	error	0.10	0.04	0.12	0.14	0.10	0.17	0.07
After the largest foreshock	Ratio	0.35	0.06	0.35	0.31	0.26	1.03	0.12
	error	0.04	0.03	0.14	0.19	0.07	0.28	0.10

Table III
Calculated Amplitude Ratios

No.	Earthquake	Calculated Amplitude ratio Ap/As at						Notes
		Yingkou	Fuxun	Zhuanghe	Luda	Caohezhuan	Jinzhou	
1	Mainshock	0.11	0.53	2.47	0.36	0.76	0.03	Using fault plane solution and location of Gu (5)
2	Foreshock	0.47	0.24	0.92	0.38	0.75	1.14	Using fault plane solution and location of Wu (1) for composite of foreshocks
3	Foreshock	0.17	0.50	0.35	0.22	1.22	0.19	Using fault plane solution and location of Gu (5) for largest foreshock
4	Foreshock	0.15	0.53	0.38	0.22	1.48	0.07	Same as No. 3 but located shifted 3km to west, 2km to north and 2km deeper

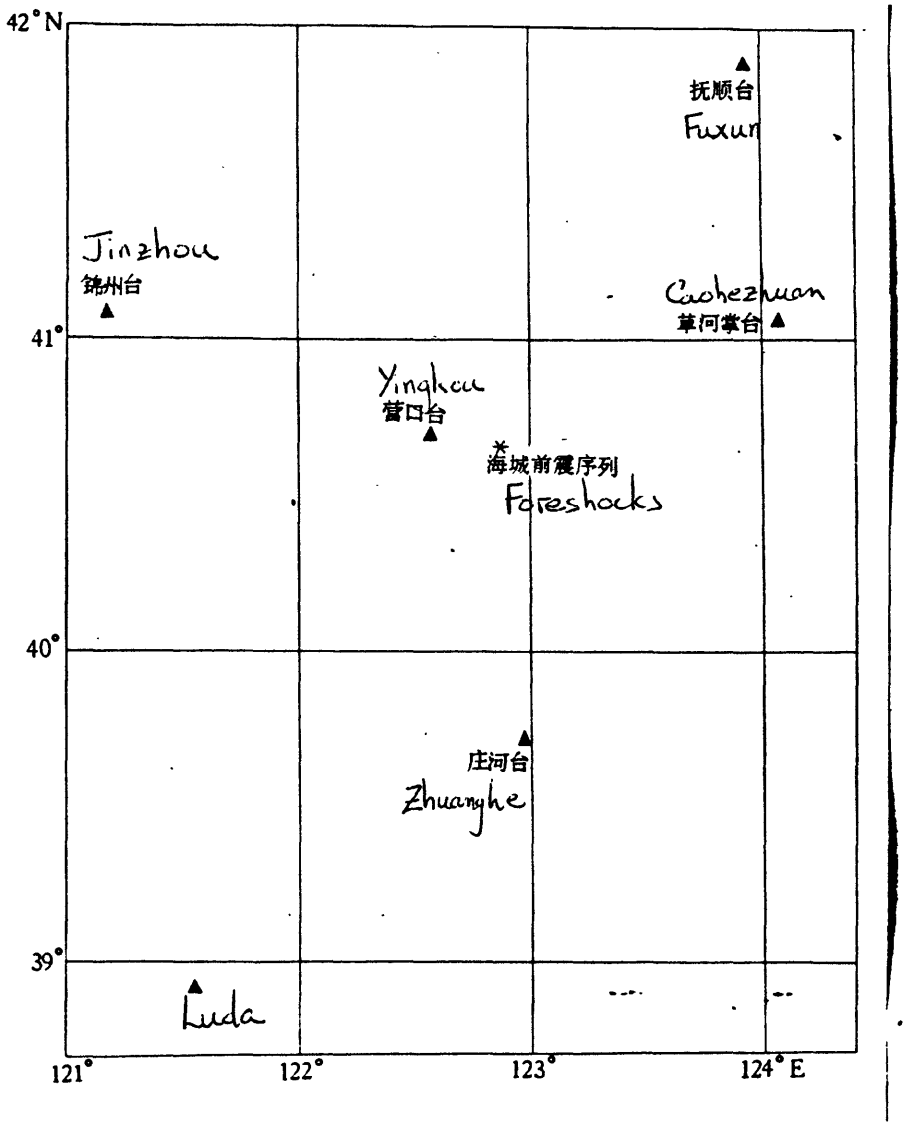
42°N
抚顺台
Fuxun
Jinzhou
锦州台
Caohezhuan
草河掌台
41°
Yingkou
营口台
海城前震序列
Foreshocks
40°
庄河台
Zhuanghe
39°
Luda
121°
122°
123°
124° E

Fig. 1

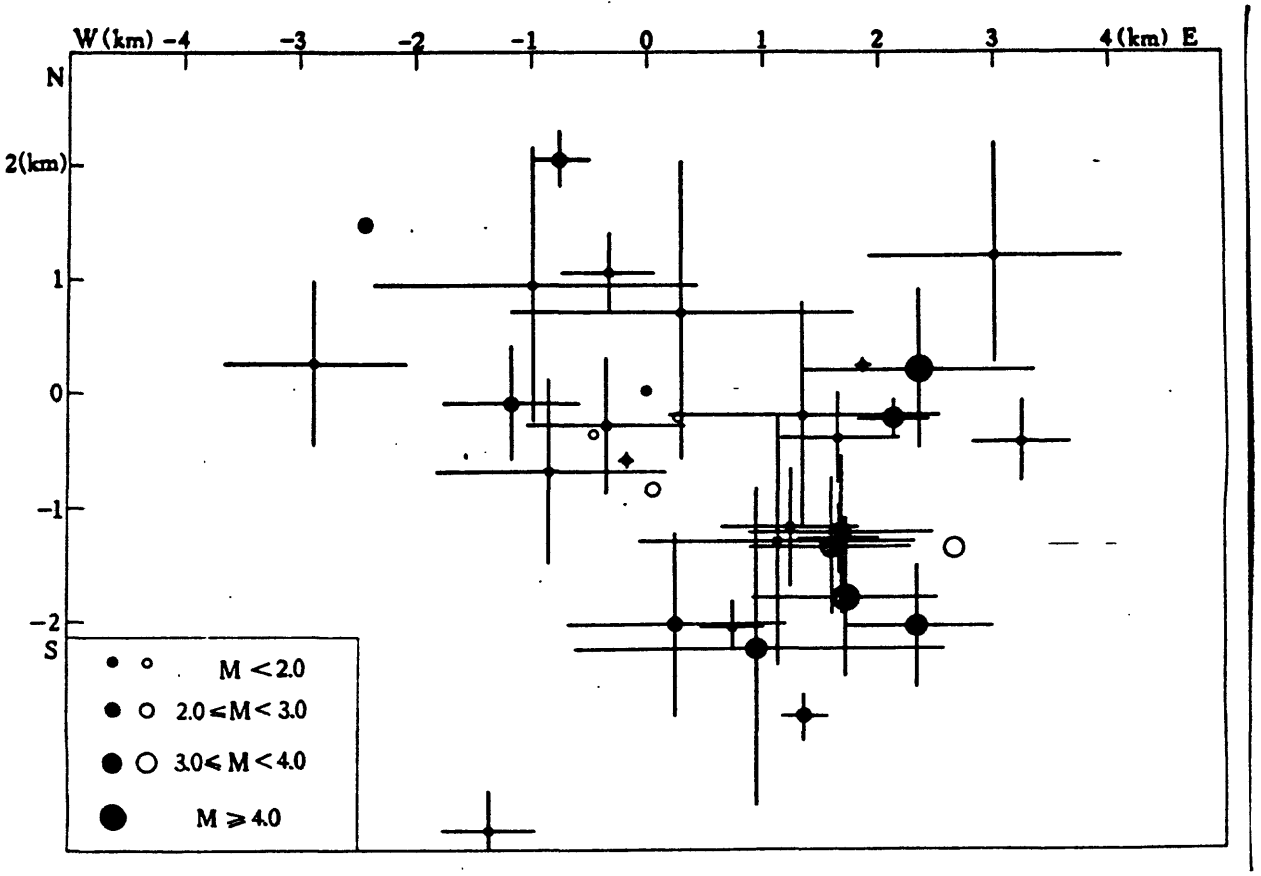

Fig. 2

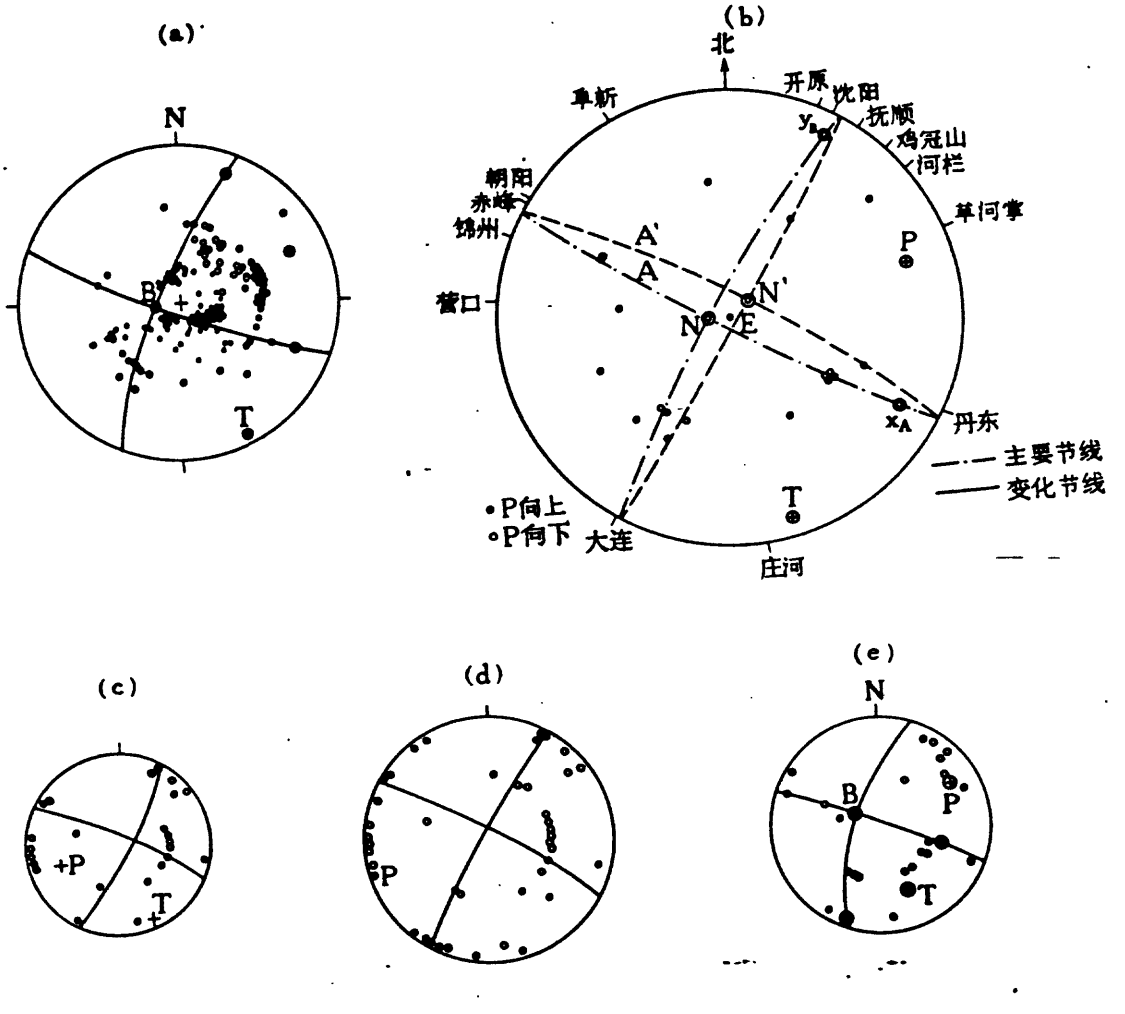
(a)
N
B
T
(b)
北
阜新
开原
沈阳
抚顺
鸡冠山
河栏
铜阳
赤峰
锦州
营口
A'
A
N'
N
E
P
单河掌
丹东
大连
庄河
主要节线
变化节线
•P向上
◦P向下
(c)
+P
T
(d)
P
(e)
N
B
P
T

图三

Fig 3

Figure 4

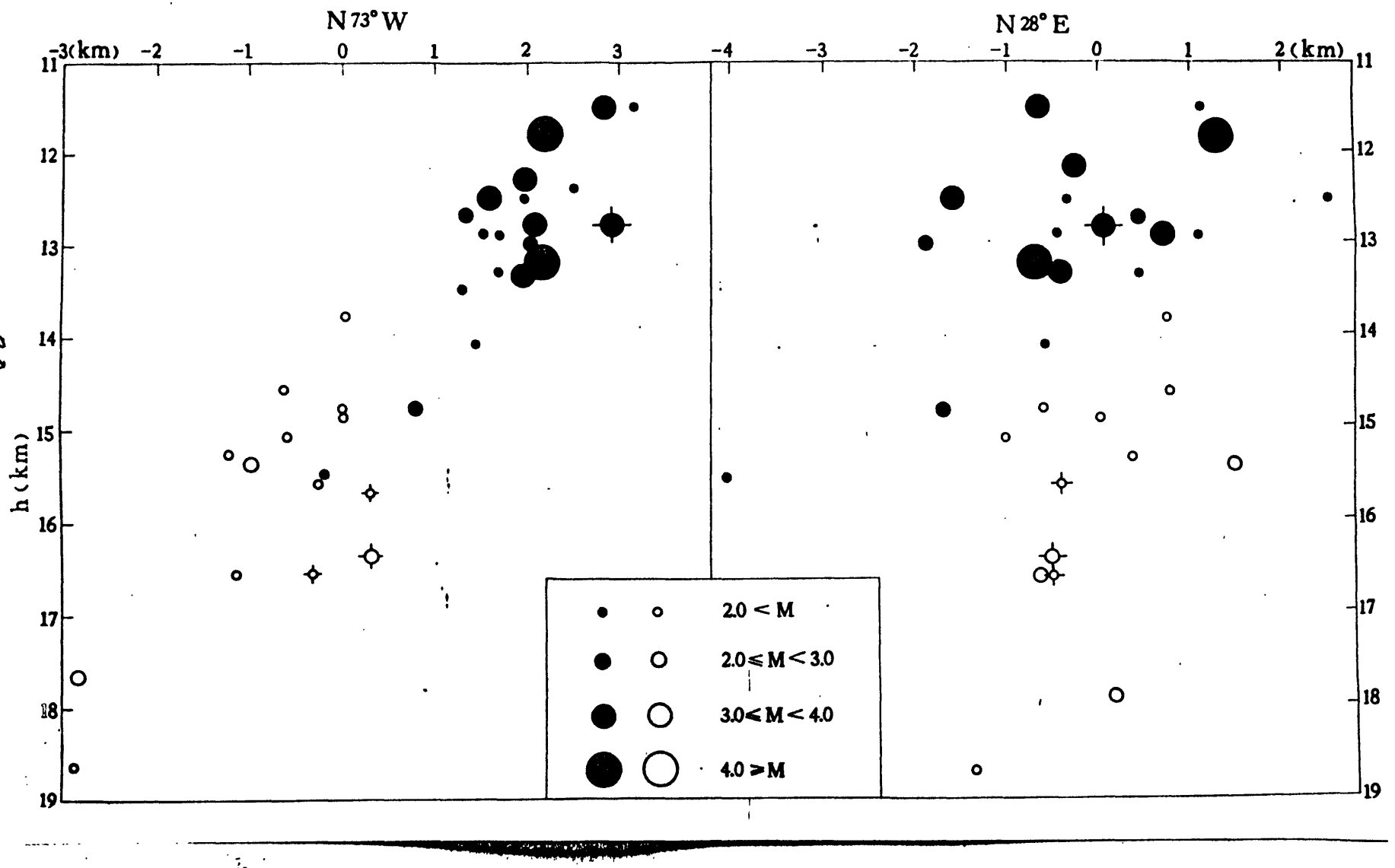
N 73° W
N 28° E
-3(km) -2 -1 0 1 2 3
-4 -3 -2 -1 0 1 2 (km)
h (km)
11 12 13 14 15 16 17 18 19
2.0 < M
2.0 ≤ M < 3.0
3.0 ≤ M < 4.0
4.0 ≥ M

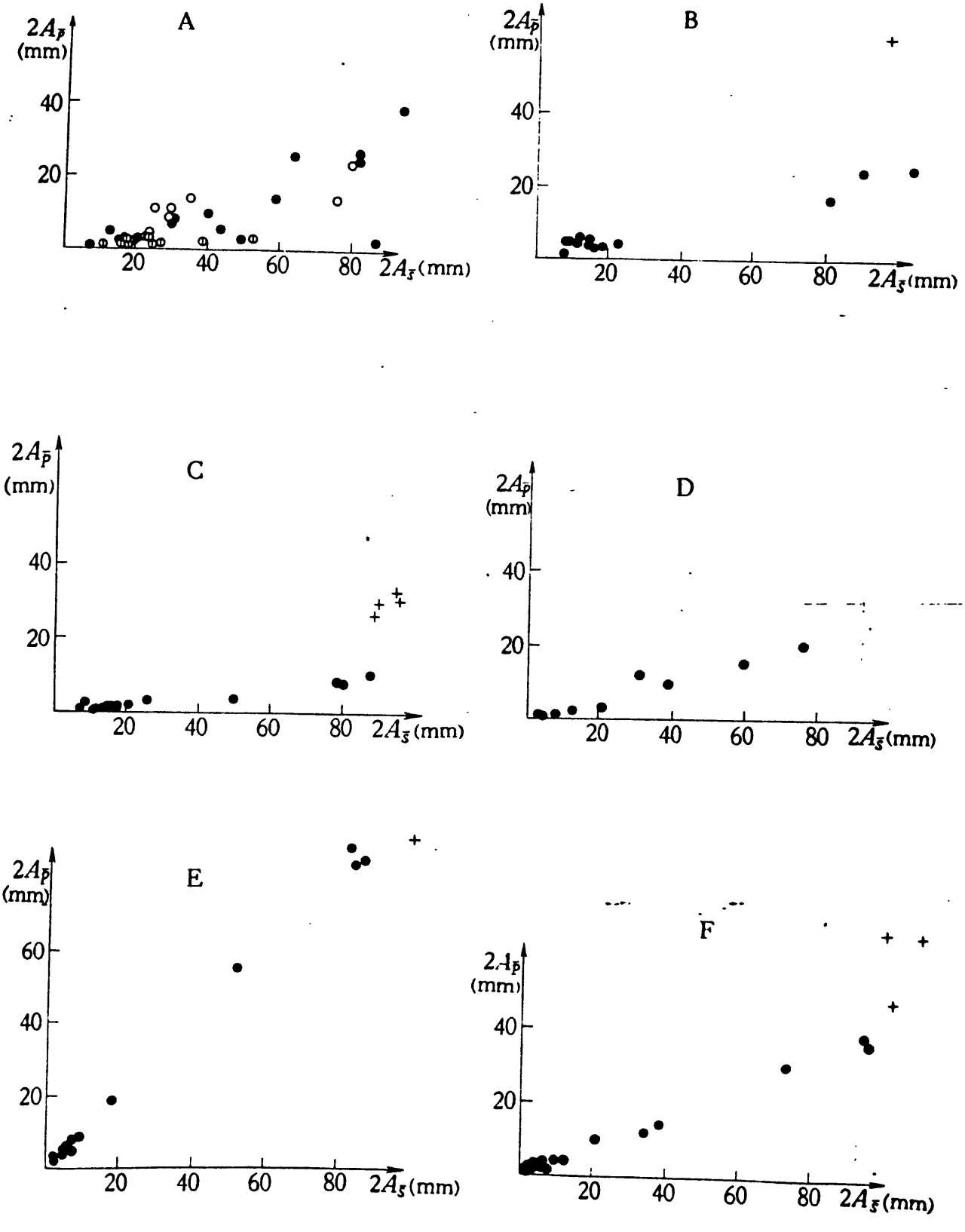

Figure 5

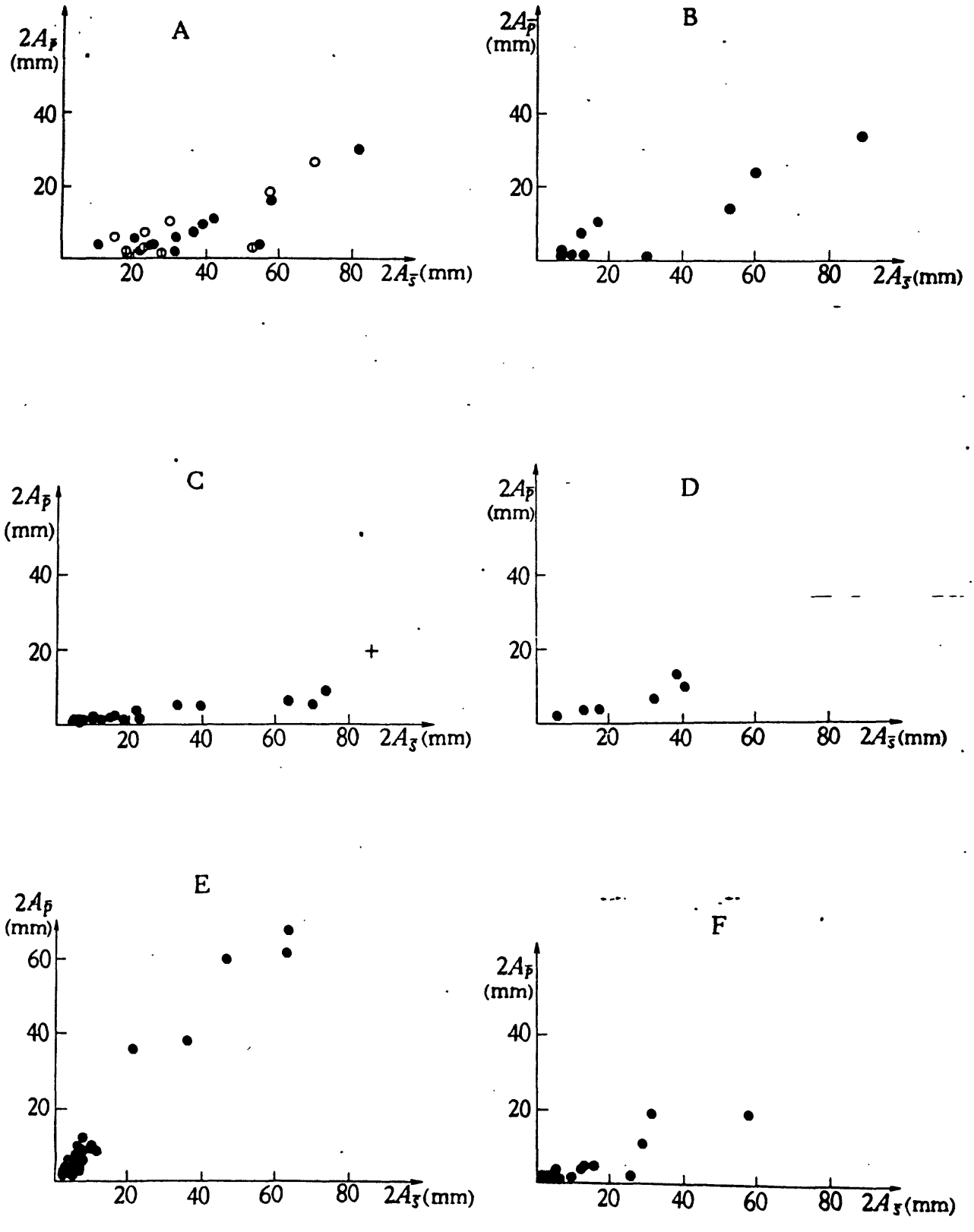

Figure 6

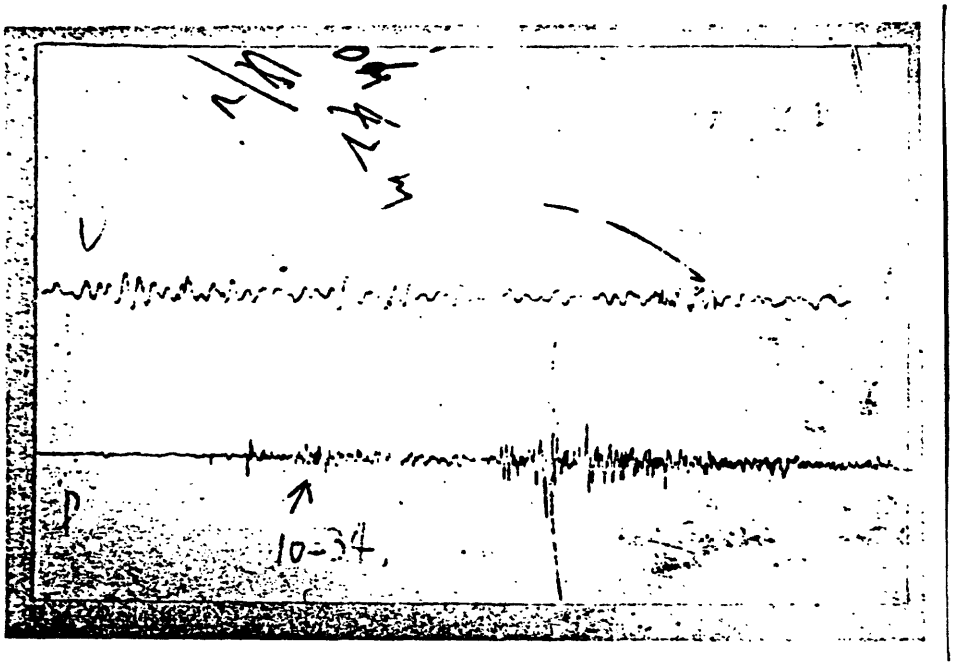

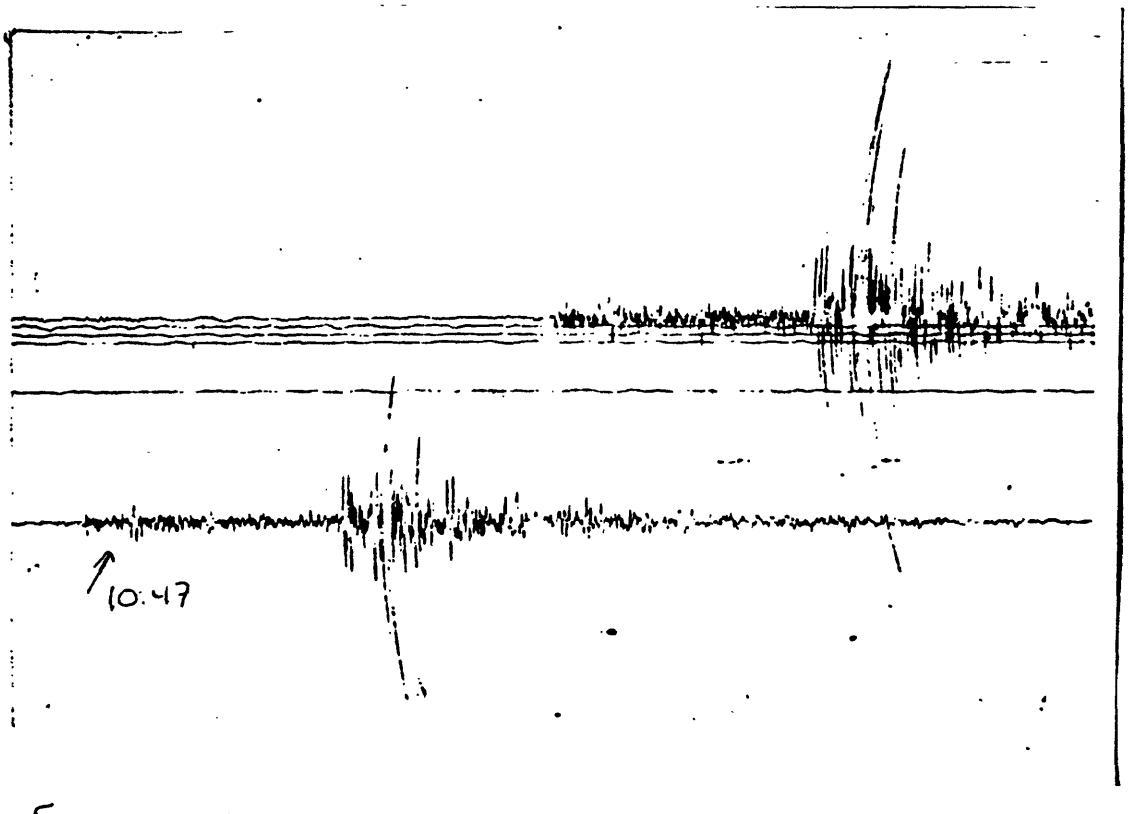

Figure 7 (a)

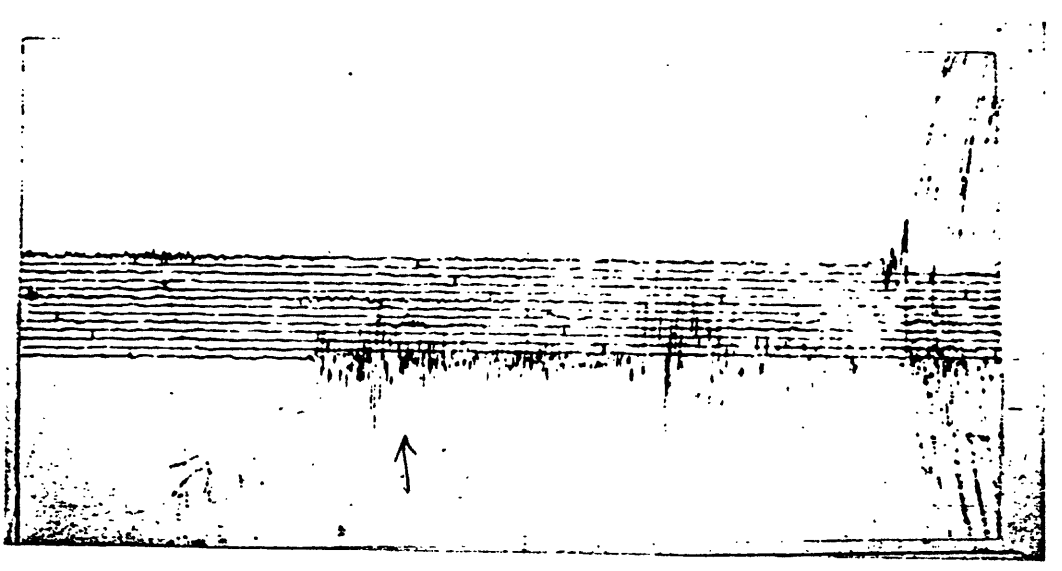

図 七 (b)

Figure 7(b)

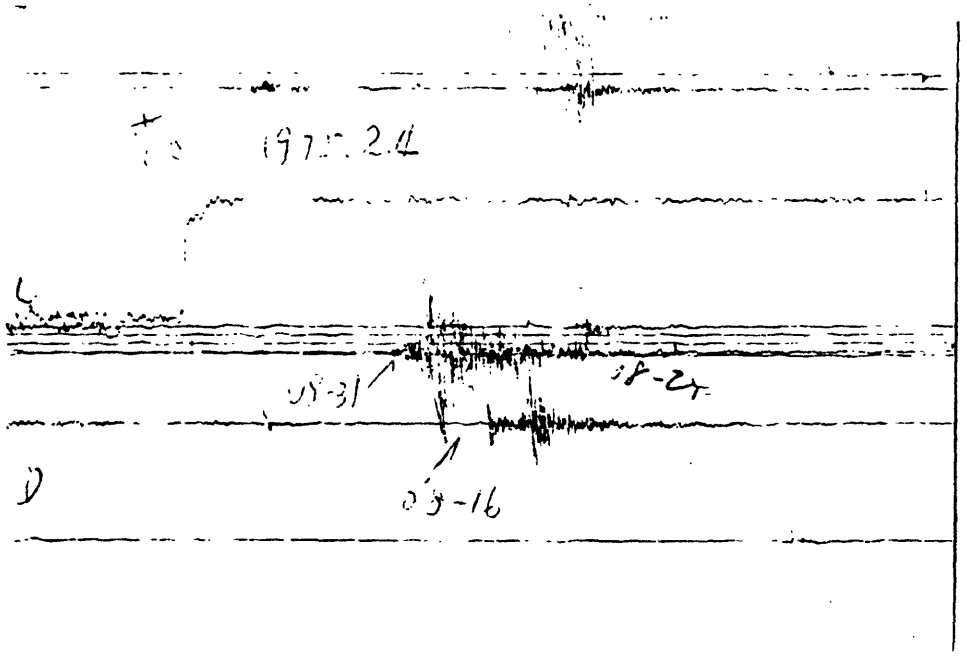

Figure 8

Revised 2
Aut. 6/30/80

2

AN INTERMEDIATE DEPTH EARTHQUAKE BENEATH TIBET: SOURCE CHARACTERISTICS OF THE EVENT OF SEPTEMBER 14, 1976

Wang-Ping Chen
Department of Earth and Planetary Sciences
Massachusetts Institute of Technology
Cambridge, MA 02139

John L. Nabelek
Department of Earth and Planetary Sciences
Massachusetts Institute of Technology
Cambridge, MA 02139

Thomas J. Fitch
Applied Seismology Group, Lincoln Laboratory
Massachusetts Institute of Tchnology
Cambridge, MA 02139

Peter Molnar
Department of Earth and Planetary Sciences
Massachusetts Institute of Technology
Cambridge, MA 02139

ABSTRACT

This paper presents the results of a detailed study of an intermediate depth earthquake beneath southern Tibet (September 14, 1976; 06 h 43 m 51.6 s; 29.81°N, 89.57°E; focal depth 90±10 km; m_b = 5.4). From the differences in arrival times of P, pP, and sP and from Rayleigh wave spectral densities the focus is estimated to be at depth of 90±10 km and therefore in the uppermost mantle. From the polarities of the first motions of P waves, inversion of the relative amplitudes of P, pP, and sP and synthesis of their waveforms, the source mechanism is constrained to be predominantly normal faulting with the T-axis approximately horizontal and trending east-west. This mechanism is similar to those of shallow earthquakes in Tibet. The occurrence of an earthquake at depth of 90 km is consistent with rapid deformation at a temperature of about 700 to 800°C in the mantle beneath the Tibetan crust. The seismic moment of an equivalent double couple point source is estimated to be about 9 x 10^{24} dyne*cm (with an uncertainty factor of 1.3) from the sP amplitudes in the period range near 10 sec, and 5 x 10^{24} dyne*cm (also with an uncertainty factor of 1.3) from the spectral density of Rayleigh waves with periods of 50 sec.

INTRODUCTION

Intermediate and deep focus earthquakes are typically associated with the subduction of oceanic lithosphere and rarely occur beneath continents. Although intermediate depth earthquakes in the Hindu Kush, the Carpathians, Burma and the deep Spanish earthquake of 1954 are good examples of such events beneath continents, they are generally considered to be evidence for sinking slabs of oceanic lithosphere from a past subduction zone [e.g., Chatelain et al., 1980; Chung and Kanamori, 1976; Isacks and Molnar, 1971; Roecker et al., 1980]. Presumably, material at intermediate depths can be strong enough to support the stresses needed to cause earthquakes only where cold lithosphere is subducted into asthenosphere.

The hypocenter distributions and fault plane solutions of deep and intermediate earthquakes have been used extensively to study the state of stess in subducted oceanic slabs [e.g., Isacks and Molnar, 1971]. Nevetherless, controversy remains about the physical mechanisms of these earthquakes. Do they result from deformation processes analogous to brittle failure or stick-slip of earth materials as observed in laboratory experiments or from some other physical processes? In order to answer these questions, studies employing more sophisticated methods of source analysis than presently available may be needed.

In this study, we present seismic evidence of an earthquake with a focal depth of about 90 km beneath southern Tibet where active subduction of oceanic lithosphere presumably ceased several tens of millions of years ago [Molnar and Tapponnier,

1975]. To our knowledge this is the first study of an earthquake which occured at an intermediate depth but cannot be directly ascribed to the subduction of an oceanic slab. An earthquake taking place under such circumstances provides an unique opportunity to study the stress regime deep in the continental lithosphere.

An understanding of the high Tibetan Plateau, north of the Himalayan moutain belt, is critical to an understanding of the relationship between the continental collision between India and Eurasia beginning 40 to 50 m.y. ago and the active tectonics of much of Asia [Dewey and Burke, 1973; Molnar and Tapponnier, 1975, 1978]. South of the Tibetan Plateau, deformation seems to occur primarily by low-angle underthrusting that is presumably responsible for the high moutain ranges of the Himalaya [Fitch, 1970; Molnar et al., 1977]. Large left-lateral strike slip faults extend eastward across China from the northern and northeastern boundaries of Tibet. In the plateau itself, however, the active deformation takes place primarily by widespread normal faulting with an approximately east-west trending T-axis [Molnar and Tapponnier, 1975, 1978; Ni and York, 1978]. It is particularly interesting to note that the active normal faults extend south of the suture into the high Himalaya so that the boundary of the Tibetan plateau, as defined by its present tectonics, appears to have grown in that direction [Molnar and Tapponnier, 1978]. The epicenter of the earthquake of September 14, 1976 was approximately 50 km north of the Indus Tsang-Po suture and 300 km north of the Himalayan main boundary

fault (Fig. 1).

Seismicity in Tibet is quite scattered. The focal depths are not well determined because in the absence of a local seismograph network these events have to be located teleseismically, resulting in a strong trade-off between the focal depth and origin time. The frequent observation of large short-period Rayleigh waves on the short-period seismograms of the World Wide Standardized Seismograph Network (WWSSN) [Chen and Molnar, 1975] suggests occurrence of very shallow earthquakes.

In the following sections, we present the methods used to constrain the focal depth and source mechanism of the September 14, 1976 earthquake. We show that this earthquake occurred in the upper mantle at a depth of 90 km and was caused by a normal faulting with an east-west trending T-axis. The occurrence of an earthquake at such depth has important implications for possible modes of deformation at high temperatures and pressures. The source mechanism is similar to those obtained for shallow earthquakes in Tibet and may represent the general style of deformation in the region.

DATA AND ANALYSIS

We examined the WWSSN seismograms available for this earthquake and selected those with signal to noise ratios adequate for quantitative analysis. The velocity structure used both in the surface and body wave analysis (Table I) was based on the S wave velocity model SE of Chen and Molnar [1980]. This model indicates a 70 km thick crust beneath Tibet. The P wave velocity was assumed to be 1.73 times that of the S wave velocity (Poisson's ratio of 0.25) except for the Pn velocity which was measured independently by Chen and Molnar [1980]. Below 90 km, where few observational constraints are available, the density and the P and S wave velocity structures were extended using Gutenberg's continental model [Dorman et al., 1960].

1. Differential Travel Times Between Direct P Waves and Depth Phases.

The body wave magnitude (m_b) given by the International Seismological Center (ISC) for this event is 5.4. Earthquakes of this size are marginal for first motion studies because, in general, their direct P phases are obscured by microseismic noise. For this event the observed P phases are especially weak because most of the WWSSN stations seem to be near nodes of the radiation pattern. One later phase which we identified as the sP phase, however, can be clearly observed on many long-period and several short-period seismograms. The travel time difference (δT) between P and sP is about 38 sec. Another apparent depth phase (pP) which arrives with a δT of about 27 sec can be also

recognized. Examples of the original seismograms are shown in Figure 2. The measured differential travel times are summarized in Table II.

A focal depth of 90 km is consistent with both a 28 sec travel time difference between P and pP (δT pP-P) and a 38 sec travel time difference between P and sP (δT sP-P), assuming vertical ray paths and an average crustal velocity corresponding to model SE. If the crustal thickness were 80 km instead of 70 km, with the same average crustal velocity, these differential travel times would indicate a focal depth of 85 km. In an extreme case in which the values of δT sP-P are systematically overestimated by 2 sec and the average crustal velocity is overestimated by 5% the focal depth could be as shallow as 75 km with the source located at the bottom of the crust. On the other hand, the assumption of vertical ray paths causes an underestimate of the focal depth by a few kilometers. Thus, given the uncertainties in both the differential travel times and the velocity structure, we conclude that this earthquake occured in the uppermost mantle with a focal depth of 90$\pm$10 km.

This conclusion is based on the assumpion that the apparent depth phases were correctly identified as pP and sP. In sections 4 and 5 we shall show that the polarities and amplitudes of the assumed pP and sP are consistent with those of the direct P arrivals.

2. Fault Plane Solutions From P Wave First Motions.

Figure 3 shows a range of possible fault plane solutions

which satisfy the observed P wave first motion polarities. The projections of the rays onto the focal sphere are based on take-off angles calculated from the P travel time tables of Herrin [1968] for a source located in the upper mantle. Whenever possible, the short-period seismograms were used to pinpoint the exact arrival of the P wave; long-period seismograms were used to determine the polarity of the first motion. The P arrivals at stations close to the nodes, e.g. JER and HKC, show oscillations which are not observed at the non-nodal stations. These oscillations may result from small precursor with slightly different orientation than the main event. (The polarity of reflections from the bottom of the crust or of converted phases due to impedance contrasts below the source would be inconsistent with the observed polarity of the slightly delayed arrivals.) Stations which display this oscillating behavior are marked as nodal or as uncertain readings in Fig. 3.

In the fault plane soulution, one nodal plane is fairly well constrained with a strike of 190° and dip of 57°W. To parametrize the solution, we can treat this plane as the fault plane without loss of generality. The slip angle in this plane is constrained to be between 232° and 270° indicating a large component of normal faulting. In order to further constrain the source mechanism we must use information contained in the amplitudes of the individual P phases. In subsequent sections we shall refer to the results of the first motion analysis as solution 1 and that of the following moment tensor inversion and waveform modelling as solution 2 (Table III).

3. Rayleigh Wave Amplitude Spectra.

An obvious indication of the depth of this event is the lack of Rayleigh waves with periods less than 20 sec on almost all the WWSSN long-period seismograms (Fig. 4). Not surprisingly, no surface wave magnitude was assigned by the ISC. Tsai and Aki [1970] demonstrated that in the period range of 10 to 50 sec, where the Rayleigh wave attenuation is nearly independent of period, the Rayleigh wave excitation depends mainly on the properies of the source. In particular, they showed that the shape of the Rayleigh wave amplitude spectra could be used to determine the focal depth without exact knowledge of the attenuation coefficient.

Thirteen WWSSN vertical component seismograms with visible Rayleigh wave signals of 50 sec period were digitized in the group velocity window of 2.8 to 4.0 km/sec. The amplitude spectra in the period range of 10 to 50 sec, with the effect of instrument response removed, are shown in Figure 5. Because we are only interested in the shapes of the amplitude spectra, the spectra were not corrected for attenuation. The spectra show a rapid decrease toward the short periods although periods less then 20 sec appear to be somewhat contaminated by short-period noise (probably due to higher modes) which is clearly visible on the seismograms (Fig. 4).

Tsai and Aki [1970] discussed in detail the possible effects of various source and propagation parameters on the determination of source depth from Rayleigh wave amplitude spectra. In our case, the assumption of a point source is a good approximation

considering the small magnitude of this earthquake. Since a duration of far-field source time function of 2.6 sec gives satisfactory results for the synthetic P waveforms (section 5), the effects of the source time-function on the surface wave spectra are negligible. The numerical experiments of Tsai and Aki [1970], which explored the effects of different velocity structures, indicate that errors due to an uncertainty in our knowledge of the crustal and upper mantle velocity structure beneath Tibet should be small.

We examined the effects of the different fault plane solutions obtained in this study (Table III) and found that adopting different solutions had a negligible effect on the shape of calculated Rayleigh wave amplitude spectra between 10 and 50 sec for a source depth around 90 km. Figure 5 shows that within the range of possible focal mechanisms the principal factor affecting the shapes of the spectra is the depth of the focus. It is clear that a source depth of 45 km will not fit the observations. The best overall fit was obtained for a source at a depth of 90 km, but the observed Rayleigh wave amplitude spectra between 20 and 50 sec cannot constrain the depth better than ± 10 km.

From the observed amplitude spectral densities at the 50 sec period the seismic moment is estimated to be about 5×10^{24} dyne*cm with an uncertainty factor of 1.3 estimated from the scatter of data (Fig. 6). In the moment calculation we have assumed the fault plane solution 2 at 90 km depth and an attenuation coefficient of 1.5×10^{-4} km^{-1} [Ben-Menahem, 1965; Tsai

and Aki, 1970]. Other combinations of possible source depths from 85 to 95 km and fault plane solutions shown in Table III also give seismic moment between 5 and 6 x 10^{24} dyne*cm and an estimated uncertainty factor of 1.3.

4. Seismic Moment Tensor Inversion of P Wave Amplitudes.

Since the fault plane solution obtained from P wave first motion polarities alone is not tightly constrained, the amplitudes of the P phases are employed to provide additional constraint on the focal mechanism.

The response of an elastic body to an arbitrary static seismic moment tensor at a point source can be found by differentiating the Green's function with respect to the source coordinates. Suppose we have a force couple at the source position $\underline{\xi}$ with the force pointing in the $\hat{\imath}$ direction and the moment arm pointing at the $\hat{\jmath}$ direction. (This corresponds to a M_{ij} term in the moment tensor.) If the Green's function $G_{ni}(\underline{x}, \underline{\xi}, t)$ is known, where $\underline{x}$ is the receiver position and t is the time, then the displacement response u_n at $\underline{x}$ in the $\hat{n}$ direction, due to M_{ij}, is simply

$$u_n = \sum_{i,j} M_{ij} \frac{\partial}{\partial \xi_j} G_{ni}(\underline{x}, \underline{\xi}, t)$$

For a given set of observed displacements $\underline{u}$, M_{ij} can be found by applying the linear inverse operator $\left(\frac{\partial}{\partial \xi_j} G_{ni} \right)^{-1}$.

Recently, Fitch et al. [1980] developed an inversion to obtain the static seismic moment tensor from the amplitude of body waves. We briefly review the procedures. The problem is

simplified by equalizing the amplitude data onto the focal sphere and simply using the inverse operator of the elastic response for a whole space to perform the inversion. Usually body wave data are deconvolved in the time domain to remove the instrument response and attenuation effects. The amplitudes of identified P, pP and sP pulses are then corrected for geometrical spreading from empirical amplitude-distance curves and for reflection at the free surface over the source region. Finally, these data are projected back onto the focal sphere using take-off angles determined from standard travel time tables. Expressions for the elastic response on a focal sphere due to a point seismic moment tensor can be found in McCowan [1977].

If we assume that the principal stress axes of the various moment tensor components are coincidental, the moment tensor obtained can be uniquely decomposed into a volumetric component: the monopole; and two non-volumetric components: the double couple and the compensated linear vector dipole (CLVD) [Knopoff and Randall, 1970]. Physically, the monopole may be related to an explosion or implosion, the double couple to a shear dislocation and the linear vector dipole (combination of the monopole and the compensated linear vector dipole) to a tension crack. The interpretation of the moment tensor in terms of physical mechanism, however, is not unique.

Since for the event of September 14, 1976 the depth phases are well separated from the direct P phase and from each other, deconvolution in order to obtain their uncontaminated amplitudes was not necessary; we simply measured the peak amplitudes of P,

pP and sP with a digitizing table. Records from long-period WWSSN stations within the distance range of 30° to 80° and with good signal-to-noise ratios for at least one of the P phases were used (Table IV). The amplitudes of pP and sP were corrected for conversions at the free surface using reflection coefficients calculated for free surface P wave velocity of 6 km/sec and Poisson's ratio of 0.25. The angles of incidence at the surface were calculated for the same ray parameter as the take-off angles [e.g. Richter 1958]. The source was assumed to be in the upper mantle.

Because several stations had rather low direct P signal-to-noise ratio, we performed the inversion using the L1 norm [Clęarbout and Muir, 1973]. The L1 norm, in addition to being less sensitive to errors in the data, allows incorporation of first motion polarities into the inversion. [Fitch et al., 1980]. The moment tensor resulting from the inversion of the amplitude data and first motion polarities has 32.6% double couple, 55.8% CLVD and 11.7% monopole components. The orientation of the double couple component corresponds to a fault plane solution with $\phi = 232°$, $\delta = 64°$ and $\lambda = 318°$ (Fig.8). On the other hand, if the source is constrained to be a double couple [Strelitz, 1978], the solution of the least squares inversion (L2 norm) of the amplitude data gives the source orientation with $\phi = 215°$, $\delta = 52°$ and $\lambda = 292°$ (solution 2b, table IV). Inspection of the residuals from these two different approaches does not reveal which data are responsible for the large CLVD component obtained from the unconstrained inversion.

This leads us to suspect that the large non-double couple component may be an artifact due to insufficient coverage of the focal sphere.

To further investigate this possibility, we extended the data set by adding first motion polarities reported in the ISC Bulletin for 9 stations located north of the source region in the U.S.S.R.. The solution of the unconstrained inversion using this extended data set has 94.2% double couple and only 1.1% CLVD and 4.7% monopole (solution 2a, Table IV). The orientation of the double couple component of this solution is $\phi = 216°$, $\delta = 55°$ and $\lambda = 295°$, almost identical to the solution of the constrained inversion.

In order to investigate the sensitivity of the solution to changes in the medium parameters we corrected the free surface reflectedions by assuming a near surface P wave velocity of 5 km/sec (instead of 6 km/sec); the unconstrained inversion of the extended data set gives a solution in which the nodal planes for the double couple component remain essentially unchanged, but the moment tensor has 83.8% double-couple and 8.9% CLVD and 7.3% monopole components. On the other hand, if the take-off angles are adjusted by increasing the velocities in the source region by 4%, the resulting solution approaches a pure (96.3%) double couple with only 2.7% CLVD and 1% monopole and the same orientation as before.

As we have demonstrated, there is no convincing evidence for large departure from the double couple mechanism. Furthermore, systematic errors arising from the assumptions involved in the

moment tensor analysis as well as the quality and size of our data set preclude an accurate measure of the non-double couple components. The most important result of this analysis is the knowledge of the orientation of the P, T and B axes in the source region. All the inversions of our dataset discussed above, resulted in essentially same orientations of these axes. The double couple fault plane solution corresponding to these axes (solution 2) is similar to the solution 1 ($\lambda = 270^{\circ}$) based only on the first motion data, indicating predominantly normal faulting mechanism. A fault plane solution with large right lateral strike slip component, similar to the solution 1 ($\lambda = 232^{\circ}$) is clearly not consistent with the amplitude data.

5. Waveform Matching of P phases.

In this section we shall use waveform modelling to further investigate the source mechanism of the September 14, 1976 earthquake. Synthetic seismograms provide visual means for displaying the sensitivity of the solution to variations in different parameters. In contrast to the moment tensor inversion they allow use of stations with low signal-to-noise ratio but which can stil qualitatively provide constraints on the solution.

The body wave seismograms are sensitive to the details of the crustal structure because of their high frequency content. Large impedance contrasts over a short depth range can produce reflections and phase conversions which can be seen on the seismograms. It is therefore important to find a proper

approximation to the crustal structure in the vicinity of the source. In our case we want to model only amplitudes and polarities of P, pP, and sP and thus we must be particularly careful about the choice of take-off angles at the source and incidence angles at the free surface. Because there are large differences in impedance in the immediate vicinity of the source and near the free surface, a homogeneous halfspace model is inadequate. One approach would be to directly introduce a layered model and calculate the response of the medium using Haskell's algorithm. This technique will give correct take-off angles and the incidence angles at the free surface, if the velocities of the top layer and the layer containing the source are properly specified. A discreetely layered model, however, has two major drawbacks: 1) a smoothly varying structure must be approximated by a large number of layers, and 2) unless the layer parameters are well determined, the discreet impedance boundaries between the layers cause phase reflections and conversions which add undesirable noise to the analysis.

An alternative approach, which we also followed in the moment tensor inversion, is to calculate the take-off angles for P, pP and sP for the medium parameters in the immediate vicinity of the source and then to correct the pP and sP only for the free surface effect with appropriate physical parameters of the medium near the free surface. The crust between the free surface and the source can be substituted by an average crust influencing only the travel times. This approximation is equivalent to a smoothly varying crustal structure in which rays refract but do

not loose energy due to internal reflections and conversions. In the absence of both a detailed knowledge of the crustal structure in the vicinity of the September 14, 1976 earthquake and large internal crustal reflections visible on the seismograms the second alternative appears to be more appropriate for our problem.

The method used to calculate the theoretical seismograms was adapted from Langston and Helmberger [1975] and Kanamori and Stewart [1976]. We have incorporated the physical parameters of the medium near the free surface in the reflection coefficients. We assume that the source acts as a pure double couple. The P-wave vertical seismogram at the receiver is given by the following equation

$$U^P = \frac{M_o}{4\pi\rho\alpha} G * C(p) \left[R^P(p,\alpha) + R^P(-p,\alpha) \Pi^{PP}(p,\alpha_1,\beta_1)\, H(t-\Delta t_1) \right.$$
$$\left. + R^{SV}(-p,\beta)\, \Pi^{SP}(p,\alpha_1,\beta_1)\, H(t-\Delta t_2)\, \frac{\eta_\alpha}{\eta_\beta} \right] * S(t) * A(t) * I(t) \qquad (1)$$

where ρ, α and β are respectively the density, compressional and shear velocities in the source region and α_1 and β_1 the compressional and shear velocities near the free surface. η_ν is defined by $\left(\frac{1}{\nu^2} - p^2\right)^{\frac{1}{2}}$; the ray parameter p is constant for a given station.

R^P and R^{SV} are the radiation patterns of P and SV expressed by

$$R^{P} = -a_1 p^2 - a_2 \eta_\alpha^2 - 2a_3 p \eta_\alpha$$

$$R^{SV} = a_3 (\eta_\beta^2 - p^2) + (a_1 - a_2) p \eta_\beta \qquad (2)$$

where a's, defined by Bouchon [1976], are functions of only source orientation.

Π^{PP} and Π^{SP} are coefficients of P to P and S to P reflections at the free surface and can be written in the following form (derived from Richter [1958])

$$\Pi^{PP} = \frac{4p^2 \eta_\alpha \eta_\beta - (\eta_\beta^2 - p^2)^2}{4p^2 \eta_\alpha \eta_\beta + (\eta_\beta^2 - p^2)^2}$$

$$\Pi^{SP} = \frac{4p \eta_\beta (\eta_\beta^2 - p^2)^2}{4p^2 \eta_\alpha \eta_\beta + (\eta_\beta^2 - p^2)^2} \qquad (3)$$

The terms M_o, G, A, C, I and S are, respectively, the seismic moment of the double couple, geometrical spreading, attenuation operator, free surface effect at the receiver, receiver response and source time function. Finally, $H(t - \Delta t_{1(2)})$ is Heaviside step function delayed by $\Delta t_{1(2)}$, the time delay of pP (sP) relative to the direct wave.

Following the procedure outlined above we generated synthetic seismograms for several stations representative of those used in the seismic moment tensor inversion of section 4.

The structure in the source region was specified by following parameters: α = 8.12 km/sec, β = 4.8 km/sec, ρ = 3.365 g/cm^3, α_1 = 6.1 km/sec and β_1 = 3.53 km/sec. The receiver region consits of a half space with P wave velocity of 6.1 km/sec and Poisson's ratio of 0.25. The correction for geometrical spreading in the mantle (G) and the ray parameter (p) appropriate for each station were determined from the P travel time tables of Herrin [1968]. A causal attenuation operator with t* (travel time/quality factor) of 1 sec was used in all calculations. Because the earthquake was sufficiently small to be approximated by a point source, only one source time function, independent of the distance and azimuth between earthquake and receiver, was required for all three P phases. The far-field source time function was a box car of 2.6 sec duration.

In section 1 we have shown that the observed time delays of pP and sP relative to the direct wave are consistent with an earthquake hypocenter located at a depth of 90 km in the mantle below the Tibetan crust. Since it would serve no further purpose to recalculate the travel times we introduced the observed time delays directly into the synthetic seismograms.

The digitized records and the corresponding synthetic seismograms are shown in Fig. 7. All of the observed wave forms were normalized to an instrumental peak magnification of 3000 while the synthetic seismograms were scaled to the largest phase seen in the observed waveforms. The best overall match between the observed and synthesized seismograms was achieved for a

source orientation given by solution 2b. For the seismograms shown, the ray parameter p was increased by 4% relative to the value based on Herrin's tables.

We consider the agreement between the observed and synthesized waveforms to be very good except at DAV where the observed P/sP ratio is especially small. The sesmic moment at DAV determined from the sP is twice as large as those from other stations. This indicates that an anomalously large sP amplitude is responsible for the discrepancy between the observed and synthesized waveforms. Although one cannot rigorously rule out unusual source or structural effects, in this case the anomalously large sP amplitude at DAV is probably due to the high noise level at the station. The signal and noise at DAV have similar frequency content and can therefore constructively interfere to produce the anomalous amplitude reading. Because station SNG lies at a distance of about 25° from the epicenter, the observed waveforms may be affected somewhat by the upper mantle structure. In absence of other good data from similar azimuth, we include this station for qualitative comparison.

We have calculated synthetic seismograms for four representative stations using also the other models discussed in the previous sections in order to display the sensitivity of our prefered solution to variation in different source and medium parameters. Seismograms a through d in figure 8 were calculated for the solutions 1 ($\lambda = 232°$), 1 ($\lambda = 270°$), 2a and 2b, respectively, using $\alpha_1 = 6.1$ km/sec for the ~~surface~~ compressional wave velocity near the free surface; seismograms e were obtained

using solution 2b and α_1 = 5.0 km/sec. Seismograms f, the prefered solution, were calculated using solution 2b with α_1 = 6.1 km/sec, but the ray parameter was increased by 4%. Clearly, solutions 1 (λ = 232°) and 1 (λ = 270°) based on only first motion data are not consistent with the observed amplitude data. The assumption of 5.0 km/sec for the ~~surface~~ compressional wave velocity near the free surface degrades the match. Solution 2b is slightly better than solution 2a but the differences are not significant when we consider uncertanties in the assumptions involved in calculation of the synthetic seismograms. The average seismic moment calculated by scaling the synthetic seismograms to the largest phase in the observed wave form is 1 x 10^{25} dyne*cm with an estimated uncertainty factor of 1.7. If we, however, ignore the anomalously large sP amplitude at DAV, the average moment is about 9 x 10^{24} dyne*cm with an uncertainty factor of 1.3. This value is in reasonable agreement with the seismic moment of 5 to 6 x 10^{24} dyne*cm estimated from the Rayleigh waves.

TECTONIC IMPLICATIONS

Normal Faulting at Depth

The epicenter of the earthquake of September 14, 1976 is about 50 km north of the suture where active subduction presumably ceased several tens of million years ago. The fault plane solution not only is very different from low-angle underthrusting, characteristic of earthquakes in the Himalaya, but is also difficult to fit into a simple scheme of a sinking slab or bending lithosphere. Therefore, although the earthquake may have occured in material that was once an oceanic lithosphere, its occurrence probably should not be taken as evidence for an actively sinking slab.

The approximately east-west trending T-axis is similar to the active normal faulting observed near the surface of Tibet. Since we studied only one event that occured in the mantle, it is risky to draw any firm conclusions about the style of deformation between the surface and this depth. If this event is representative of the deformation of the lower crust and upper mantle of Tibet, it suggests that the small amount of active east-west extention that occurs at the surface also occurs at depth.

Implications For the Temperature in the Mantle Beneath Tibet

Chen and Molnar [1980] suggested that the average temperature of the uppermost mantle immediately beneath the Tibetan Moho is likely to be about 250°C warmer than beneath stable platforms and shields [also see Chen et al., 1980]. Thus

the uppermost mantle temperature beneath Tibet could be about 750 or 800°C if that beneath the stable platforms and shields is about 500°C [Sclater et al., 1980].

To the best of our knowledge, the deepest intraplate earthquakes occur in periodic swarms about 60 km beneath the sumit of Kilauea in Hawaii [Eaton, 1962] and presumably are related to volcanic activity there. Using a cooling plate model for the thermal history of the oceanic lithosphere [Parsons and Sclater, 1977], the temperature at 60 km depth in a 100 m.y. old oceanic plate can be estimated to be about 750°C. A possible anomalously high rate of non-conductive heat transport from the asthenosphere might increase this temperature estimate somewhat. Morover, thermodynamic data indicate that the solidus for basaltic material under water saturated conditions (the lower bound of the solidus) is about 700°C at 20 kb corresponding to 60 km of lithostatic load [e.g., Merrill et al., 1970]. Thus even if magma exists at that depth, the temperature at 60 km beneath Kilauea should be at least 700°C. This suggests that earthquake activity can occur in mantle materials at temperatures near 750°C if there are sufficient stress differences at these depths.

The flow laws for olivine obtained from laboratory experiments [e.g., Goetze, 1978] indicate that at a strain rate of about 8×10^{-16} sec^{-1}, (100% strain over the past 40 m.y. since the onset of the continental collision between India and Eurasia) only 1.1 to 0.43 kb of differential stress are necessary to maintain steady state dislocation creep of olivine at

temperatures of 750 to 800°C, respectively [Chen and Molnar, 1980]. This estimate is very crude because of uncertainties in the activation energy and temperature. On the other hand, occurrence of an earthquake at 90 km beneath Tibet, indicates that deformation processes analogous to stick-slip observed at much lower P-T conditions in the laboratory are possible even at temperatures over 700°C and pressures of 30 kb, unless we have grossly over-estimated the mantle temperature or unless the source region is anomalously cool compared to the average temperature at that depth.

CONCLUSIONS

From the differences in arrival times of P, pP, and sP and from the shapes of the Rayleigh wave amplitude spectra the focal depth of the intermediate depth earthquake of Septempber 14, 1976 in southern Tibet is estimated to be 90 ± 10 km. The first motion polarities of P waves, inversion of the relative amplitudes of P, pP, and sP and matching of their waveforms with synthetic seismograms indicate predominatly normal faulting source mechanism with nearly north-south striking nodal planes. The seismic moment of an equivalent double couple source determined from the spectral densities of 50 sec Rayleigh waves and amplitudes of the sP phases is 5×10^{24} and 9×10^{24} dyne*cm, respectively. Both estimates are uncertain to about a factor of 1.3.

The essentially east-west trending T-axis is consitent with the active extention observed near the surface. If this event is representative of the deformation in the Tibetan mantle, then a small amount of the east-west extention also occurs at depth.

Since the average temperatures in the uppermost mantle beneath Tibet and 60 km beneath Hawaii could be 700 to 800°C, the occurrence of earthquakes in both regions indicates that rapid deformation can occur at these temperatures and at pressures over 20 kb.

Acknowledgements

We benefitted from several discussions with B. Evans on rock mechanics. This research was supported by the National Science Foundation Grant No. 77-23017 EAR and the United States Geological Survey Grant No. 14-08-0001-17759.

References

Ben-Menahem, A., Observed attenuation and Q values of seismic surface waves in the upper mantle, J. Geophys. Res., 70, 4641-4652, 1965.

Bouchon, M., Teleseismic body wave radiation from a seismic source in a layered medium, Geophys. J. Roy. Astr. Soc., 47, 515-530, 1976.

Chatelain, J.L., S.W. Roecker, D. Hatzfeld, and P. Molnar, Microearthquake seismicity and fault plane solutions in the Hindu-Kush region and their tectonic implications, J. Geophys. Res., 85, 1365-1387, 1979.

Chen, C.Y., W.P. Chen, and P. Molnar, The uppermost mantle P wave velocities beneath Turkey and Iran, Geophys. Res. Lett., 7, 77-80, 1980.

Chen, W.P. and P. Molnar, Short-period Rayleigh wave dispersion across the Tibetan Plateau, Bull. Seism. Soc. Amer., 65, 1051-1057, 1975.

Chen, W.P., and P. Molnar, Constraints on the seismic wave velocity structure beneath the Tibetan Plateau and their tectonic implications, (submitted to), J. Geophys. Res., 1980.

Chung, W.Y., and H. Kanamori, Source process and tectonic implications of the Spanish deep-focus earthquake of March 29, 1954, Phys. Earth Planet. Inter., 13, 85-96, 1976.

Claerbout, J.F. and F. Muir, Robust modeling with erratic data, Geophys., 38, 826-844, 1973.

Dewey, J.F., and K.C.A. Burke, Tibetan, Variscan, and Pre-Cambrian basement reactivation: Products of a continental collision, J. Geol., 81, 683-692, 1973.

Dorman, J., M. Ewing, and J. Oliver, Study of shear-velocity distribution in the upper mantle by mantle Rayleigh waves, Bull. Seism. Soc. Amer., 50, 87-115, 1960.

Eaton, J.P., Crustal structure and volcanism in Hawaii, in The Crust of the Pacific Basin, G.A. MacDonald and H. Kuno (ed.), Geophys. Monograph, 6, Amer. Geophys. Un., Washington, DC, 1962.

Fitch, T.J., Earthquake mechanism in the Himalaya, Burmese, and Andaman regions and continental tectonics in central Asia, J. Geophys. Res., 75, 2699-2709, 1970.

Fitch, T.J., D.W. McCowan, and M.W. Shields, Estimation of the seismic moment tensor from teleseismic body wave data with applications to intraplate and mantle earthquakes, J. Geophys. Res., in press, 1980.

Goetze, C., The mechanism of creep in olivine, Phil. Trans. Roy. Soc. Lond., 288, 99-119, 1978.

Herrin, E., Introduction to '1968 Seismological tables for P phases', Bull. Seism. Soc. Amer., 58, 1193-1241, 1968.

Isacks, B., and P. Molnar, Distribution of stresses in the descending lithosphere from a global survey of focal-mechanism solution of mantle earthquakes, Rev. Geophys. Space Phys., 9, 103-174, 1971.

Kanamori, H., and G.S. Stewart, Mode of the strain release along the Gibbs fracture zone, Mid-Atlantic ridge, Phys. Earth Planet. Int., 11, 312-332, 1976.

Knopoff, L., and M.J. Randall, The compensated linear-vector dipole: a possible mechanism for deep earthquakes, J. Geophys. Res., 75, 4957-4963, 1970.

Langston, C.A. and D.V. Helmberger, A prodedure for modelling shallow dislocation sources, Geophys. J. R. Astro. Soc., 42, 117-130, 1975.

McCowan, D.W., A moment-tensor representation of body wave displacement vectors on the focal sphere, in Semiannual Technical Summary, pp. 9-11, Lincoln Laboratory, M.I.T., Lexington, MA, March, 1977.

Merrill, R.B., J.K. Robertson, and P.J. Wyllie, Melting reactions in the system $NaAlSi_3O_8$-$KAlSi_3O_8$-SiO_2-H_2O to 20 kilobars compared with results for other feldspar-quartz-H_2O and rock - H_2O systems, J. Geol., 78, 558-569, 1970.

Molnar, P., W.P. Chen, T.J. Fitch, P. Tapponnier, W.E.K. Warsi, and F.T. Wu, Structure and tectonics of the Himalaya: A brief summary of relevant geophysical observation, in Himalaya: Sciences de la Terre, pp. 269-294, Centre National de la Recherche Scientifique, Paris, 1977.

Molnar, P., and P. Tapponnier, Cenozoic tectonics of Asia: Effects of a continental collision, Science, 189, 419-426, 1975.

Molnar, P., and P. Tapponnier, Active tectonics of Tibet, J. Geophys. Res., 83, 5361-5375, 1978.

Ni, J., and J.E. York, Late Cenozoic extensional tectonics of the Tibetan Plateau, J. Geophys. Res., 83, 5377-5387, 1978.

Parsons, B., and J.G. Sclater, An analysis of the variation of ocean floor bathymetry and heat flow with age, J. Geophys. Res., 82, 803-827, 1977.

Ritcher, C.F., Elementary Seismology, pp. 667-673, Freeman and Co., San Francisco, 1958.

Roecker, S.W., O.V. Soboleva, D. Hatzfeld, J.L. Chatelain, and P. Molnar, Seismicity and fault plane solutions of intermediate depth earthquakes in the Pamir-Hindu Kush region, J. Geophys. Res., 85, 1358-1364, 1979.

Sclater, J.G., C. Jaupart, and D. Galson, The heat flow through oceans and continents, Rev. Geophys. Space Phys., 18, 269-311, 1980.

Strelitz, R.A., Moment tensor inversions and source models, Geophys. J. Roy. Astr. Soc., 52, 359-364, 1978.

Tsai, Y.B., and K. Aki, Precise focal depth determination from amplitude spectra of surface waves, J. Geophys. Res., 75, 5729-5743, 1970.

Table I. Seismic Wave Velocity Structure Used For Tibet (Model SE)

Depth (km)	S wave velocity (β) (km/sec)	P wave velocity (α) (km/sec)	density (g/cm^3)
0-3.75	2.55	4.41	2.41
3.75-45	3.4	5.88	3.0
45-70	3.7	6.4	3.32
70-90	4.8	8.12	3.365
90-100	4.41	8.02	3.38

Table II. P Wave Travel Time Differences Between the Direct and Depth Phases at WWSSN Stations

Station	Δ(Deg.)	Azimuth (Deg.)	δT pP-P (sec)	δT sP-P (sec)	Instrument
AAE	51.7	257		38±2	L
ATH	54.3	297	26±2	38±2	L
COL	75.7	22	28±0.5		S
DAV	40.7	116		37±2	L
HKC	23.3	103		36±2	L
IST	49.7	300		37±1	L
JER	46.3	287	27±1	38±1	L
MAL	75.8	304	27±1		L
MAT	40.9	67		37±2	L
POO	18.2	235		38±2	L
SHI	32.1	279		38±2	L
STU	62.2	312	27±0.5		S
TRI	59.9	308	26±1	38±2	L

long period instrument: L
short period instrument: S

Table III. Possible Fault Plane Solutions From P Wave First-Motion Polarities And Inversion of Amplitude Data

No.	Strike (Ø)	dip (δ)	slip angle (λ)	Method of Analysis
1	190°	57°W	232°-270°	P wave first motion polarities, upper mantle depth.
2a	216°	55°W	295°	Double couple component of the moment tensor from linear inversion of amplitudes and polarity of P phases, upper mantle depth.
2b	215°	52°W	292°	Constrained inversion of the amplitudes of P phases.

For convention of defining the fault plane solutions, see Kanamori and Stewart (1976). $\lambda = 270°$ corresponds to pure normal faulting and $\lambda = 0°$ to pure left-lateral strike-slip faulting.

TABLE IV. P Phase Amplitude Data and the Results of the Moment Tensor Inversion

Station	Take-off Angle (deg.)	Azimuth (deg.)	Δ(deg.)	Amplitude[1] (0.01 cm)	Phase[2]	Solution 2 a. Linear Inversion Normalized Amplitude	Solution 2 a. Linear Inversion Residuals	Solution 2 b. Constra Double Co Residua
AAE	33.2	257.2	51.7	-4.8	0	-0.338	0.000	0.040
ATU	32.4	297.3	54.3	-3.9	0	-0.276	-0.212	-0.131
IST	34.1	300.3	49.7	-3.0	0	-0.210	-0.207	-0.121
LEM	37.3	151.6	40.3	-13.1	0	-0.834	-0.101	-0.115
MAL	25.3	304.2	75.8	-3.5	0	-0.285	0.000	0.071
SHI	40.3	279.1	32.1	3.1	0	0.159	0.046	0.125
TRI	30.2	308.2	59.9	-3.6	0	-0.257	-0.130	-0.048
AAE	146.8	257.2	51.7	3.9	1	-0.366	0.000	0.058
ATU	147.6	297.3	54.3	5.9	1	-0.550	0.000	0.024
IST	145.9	300.3	49.7	6.5	1	-0.615	-0.087	-0.064
JER	144.9	286.9	46.3	5.9	1	-0.557	-0.148	-0.110
MAL	154.7	304.2	75.8	5.7	1	-0.548	0.203	0.216
TRI	149.8	308.2	59.9	6.0	1	-0.542	0.140	0.151
AAE	162.2	257.2	51.7	16.5	2	-0.395	0.080	0.051
ATU	162.5	297.3	54.3	14.0	2	-0.344	-0.021	-0.020
DAV	160.2	116.5	40.7	50.3	2	-1.000	-0.191	-0.242
IST	161.7	300.3	49.7	14.1	2	-0.329	-0.000	0.003
JER	161.2	286.9	46.3	21.6	2	-0.481	-0.057	-0.068
MAL	166.1	304.2	75.8	3.0	2	-0.105	0.052	0.067
MAT	160.2	67.4	40.9	18.7	2	-0.373	0.060	0.058
SHI	158.7	279.1	32.1	24.9	2	-0.373	0.156	0.135
TAB	159.5	294.7	36.5	29.1	2	-0.515	-0.079	-0.086
TRI	163.6	308.2	59.9	10.5	2	-0.275	-0.065	-0.050
BUL	24.4	237.5	76.9	-1	3			
CHG	74.5	139.9	13.9	1	3	Moment Tensor[3]:		
COL	25.3	21.8	75.7	-1	3	M_{NN}	0.01	-0.01
DAV	37.3	116.5	40.7	-1	3	M_{NE}	-0.31	-0.28
HKC	44.9	102.9	23.3	-1	3	M_{EE}	1.00	0.89
KBL	62.5	290.5	18.0	1	3	M_{NZ}	0.39	0.32
KEV	32.9	337.2	52.9	-1	3	M_{EZ}	-0.10	-0.10
KON	30.2	324.6	59.8	-1	3	M_{ZZ}	-0.85	-0.88
MAT	37.3	67.4	40.9	-1	3			
NAI	30.2	248.2	59.0	-1	3			
NDI	83.3	267.1	10.8	1	3			
SHL	83.3	153.6	4.7	1	3			
SNG	43.7	153.0	24.8	-1	3			
BKR[4]	38.1	300.7	38.8	1	3			

TABLE 2.1 (cont'd)

GRS	38.8	297.2	36.6	1	3
ELT	44.9	355.0	23.5	1	3
SRI	39.8	292.5	34.1	1	3
SVE	39.4	331.4	33.8	1	3
TAS	52.4	310.4	20.0	1	3
YAK	37.1	27.3	41.5	-1	3
YSS	36.1	51.8	44.2	-1	3
ZAK	46.8	22.9	23.0	-1	3

[1]Vertical component, normalized to peak magnification of 1500. Integers are P wave first motion polarities, +1 for compression, and -1 for dilitation.

[2]0:P, 1:pP, 2:sP, 3:First motion polarity of P.

[3]Explosion is positive.

[4]First motion polarities for the following nine stations in the U.S.S.R. are obtained from the ISC Bulletins.

Figure Captions

Fig. 1. Simplified map of active tectonics of Tibet and surrounding regions (adapted from Molnar and Tapponnier [1978]) showing the epicenter of the earthquake studied (⊕). Heavy lines are major faults (dashed when less certain) recognized on the Landsat imagery. Dotted areas are sediment-filled basins presumably due to normal faulting. Thin dashed lines are a schematic outline of the 32°N fold belt. Cenonzoic volcanism is not represented. In fault plane solutions (lower hemisphere), solid areas are compressional quadrants and open areas are dilatational quadrants. The closed and open circles are historic earthquakes with $M > 7.8$ and with $7.8 > M > 7.0$, respectively.

Fig. 2. Examples of vertical component long-period WWSSN seismograms (top) which recorded clear sP phase and vertical component short-period WWSSN seismograms (bottom) where clear pP phase can be easily identified.

Fig. 3. Lower hemisphere equal area projections of the P wave first motion polarities. Take-off angles are based on the Herrin P travel time tables for a source located in the upper mantle. Solid and open circles represent compressional and dilatational first motions, respectively. Two different southeast dipping nodal planes are extreme solutions allowed by the data. The poles of these planes are indicated by large crosses.

Fig. 4. Examples of the digitized traces of the vertical component long-period WWSSN seismograms with clear Raileigh wave signals. Note the absence of Rayleigh wave energy with periods shorter than about 20 sec.

Fig. 5. Amplitude spectra of the vertical component of the observed Rayleigh Waves after correction for the instrument response. The spectra are not smoothed and only peaks and troughs are plotted. Theoretical spectra at four different source depths with different fault plane solutions are shown for comparison. Solution 1 ($\lambda = 270°$) was used for the focal depth of 85 km, and solution 2 for the focal depth of 70 and 95 km. For the 45 km depth, the source mechanism with

$\phi = 180°$, $\delta = 66°$W and $\lambda = 222°$ was used. This mechanism was obtained from a fault plane solution constructed for a focus located in the crust. The theoretical spectra were generated for the velocity model shown in Table I with a seismic moment of 1×10^{27} dyne*cm and were corrected for geometrical spreading. (No attenuation correction was applied.) In d) and j) the theoretical spectra for the 85 km depth were computed using solutions 1 ($\lambda = 270°$ and $232°$) showing that the effects of different source orientations on the shape of the theoretical spectra are negligible compared to the effect of the depth of the focus.

Fig. 6. Spectral densities of the vertical component of the observed Rayleigh waves at a period of 50 sec (solid circles) equilized to the source, assuming an attenuation

coefficient of $1.5 \times 10^{-4} km^{-1}$. The solid curve shows the theoretical spectrum predicted for a source with fault plane solution 2 (Table III) at 90 km depth. The dashed curve shows that for a source with fault plane solution 1 ($\lambda = 232°$) at 85 km depth. The theoretical spectra were calculated for a moment of 5.5×10^{24} dyne*cm. The assumed seismic velocity structure is shown in Table I. Station JER is not used in Fig. 5 because the later part of the dispersed Rayleigh wave train overlaps a calibration pulse.

Fig. 7. Examples of the observed P-wave seismograms (top trace) and corresponding synthetic seismograms (bottom trace). The amplitude of the observed seismograms was normalized to an instrument magnification of 3000; the synthetic seismograms were scaled to the largest observed phase. The beginning of the synthetic seismograms marks the onset of the direct P phase. Also plotted are the P-wave first motion polarities (solid circles for compressional, open circles for dilatational and X for nodal; small symbols for less certain readings), pP polarities (+ for compressional and - for dilatational), positions of the sP reflections (symbol "2") and the ISC data (C and D). The fault plane solutions (lower hemisphere) shown are (Table III): solution 2b (solid line) obtained by constrained double couple inversion of P-wave amplitudes and also used in the calculation of the synthetic seismograms; solution 2a (dotted line) resulting from unconstrained moment tensor inversion which included

first motion data reported by ISC; result of unconstrained moment tensor inversion without the ISC data (dashed line).

Fig. 8. Observed (top traces) and synthesized (lower traces) seismograms illustrating the sensitivity of the solution to changes in the source and medium parameters. The synthetic seismograms were calculated for a) solution 1 ($\lambda = 232°$), b) solution 1 ($\lambda = 270°$), c) solution 2a and d) solution 2b, using $\alpha_1 = 6.1$ km/sec and ρ determined from the Herrin tables. The remaining seismograms correspond to solution 2b where e) $\alpha_1 = 5.0$ km/sec and ρ is unchanged and f) $\alpha_1 = 6.1$ km/sec but ρ is increased by 4%.

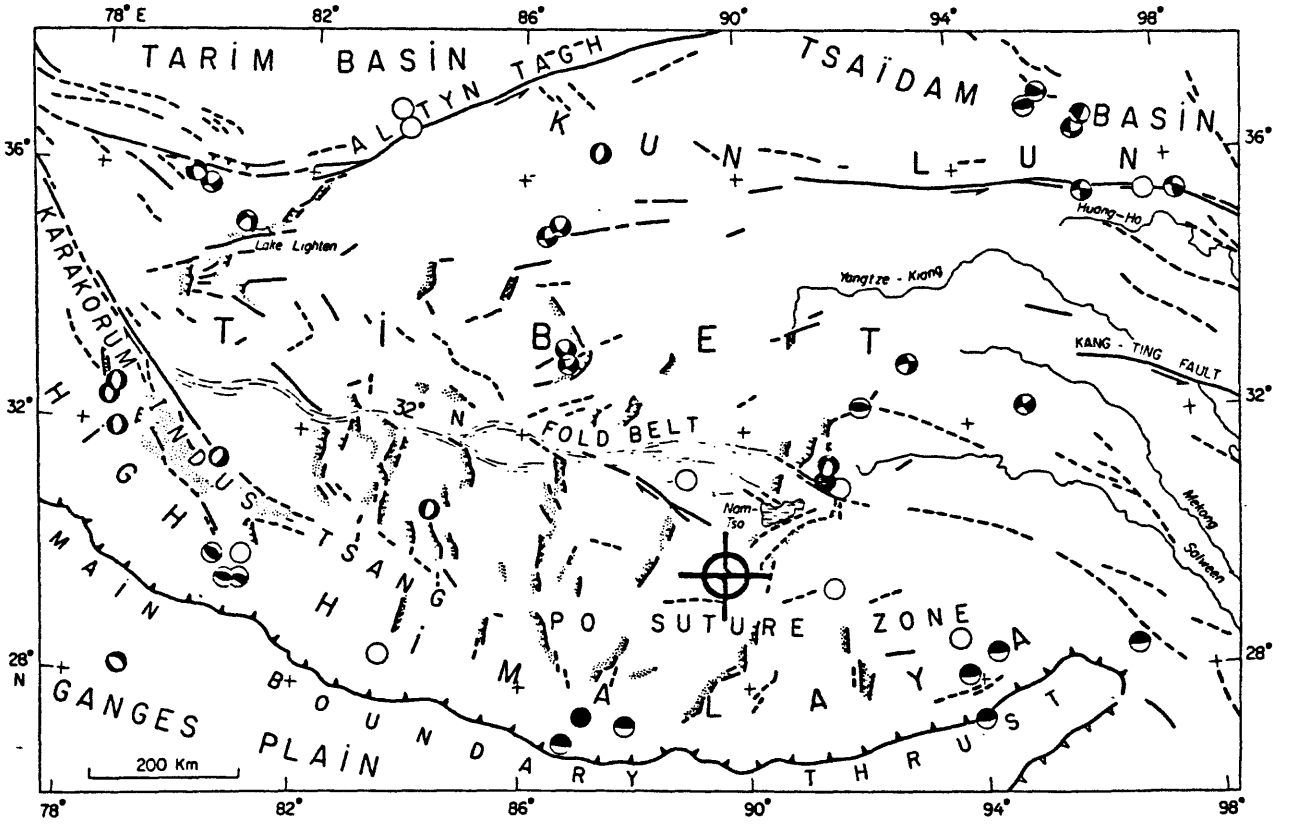
78° E
82°
86°
90°
94°
98°
36°
32°
28° N
TARİM BASİN
ALTYN TAGH
KOUN-LUN
TSAİDAM BASİN
KARAKORUM
Lake Lighten
Huang-Ho
Yangtze - Kiang
KANG - TING FAULT
T İ B E T
32° N
FOLD BELT
HIGH
INDUS
TSANG
PO
Nam-Tso
Mekong
Salween
MAIN
H İ M A L A Y A
SUTURE ZONE
GANGES PLAİN
BOUNDARY THRUST
200 Km

Fig. 1

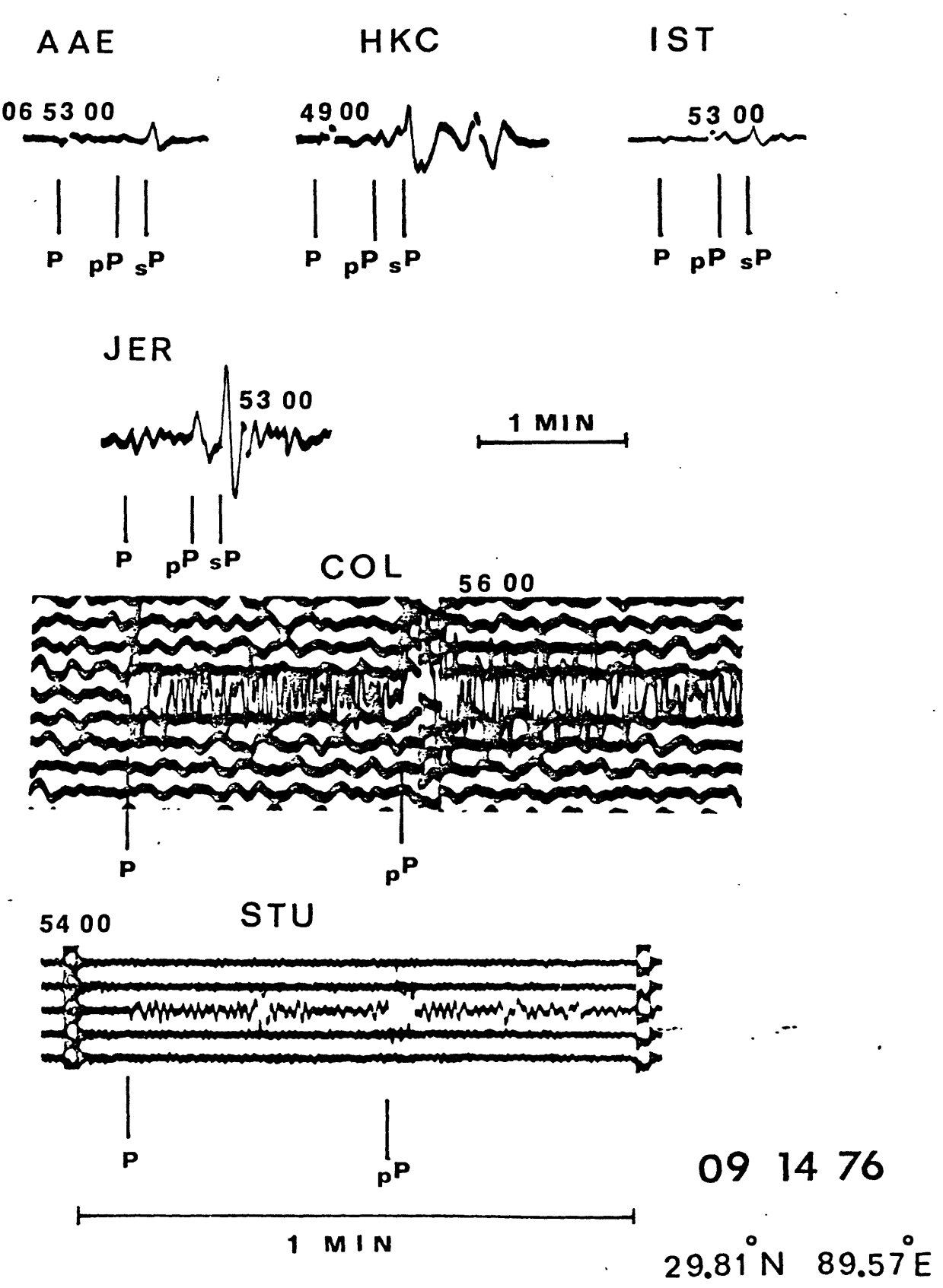
AAE
HKC
IST
06 53 00
49 00
53 00
P
pP
sP
JER
53 00
1 MIN
COL
56 00
54 00
STU
09 14 76
29.81°N 89.57°E
TIBET

Fig. 2

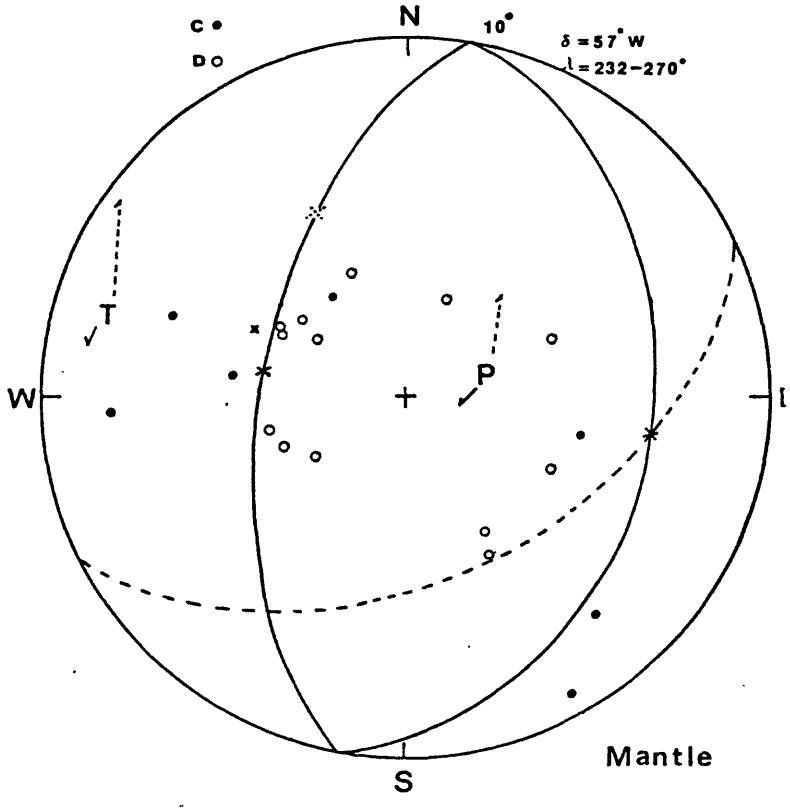

9 4 76 TIBET 29.81°N 89.57°E

FIG. 3

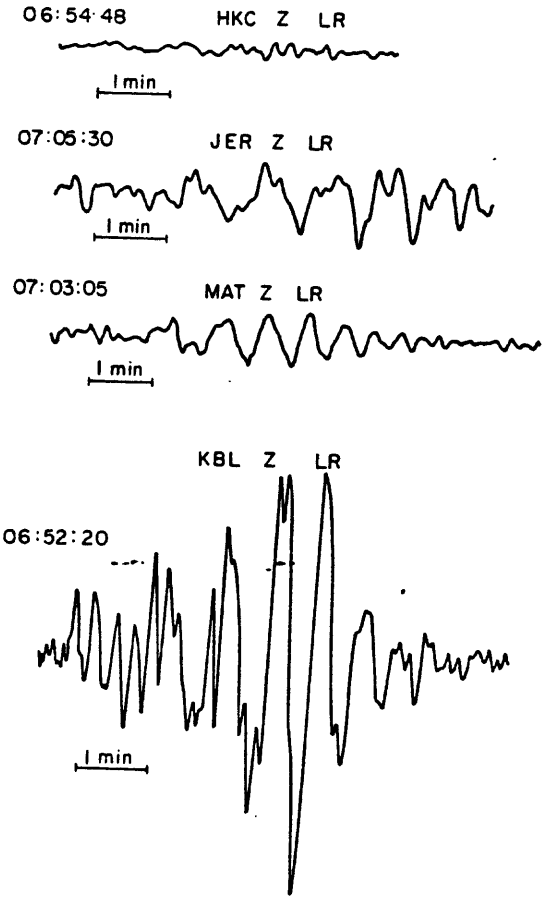

September 14, 1976 29.81°N 89.57°E
Tibet 90 km

Fig. 4

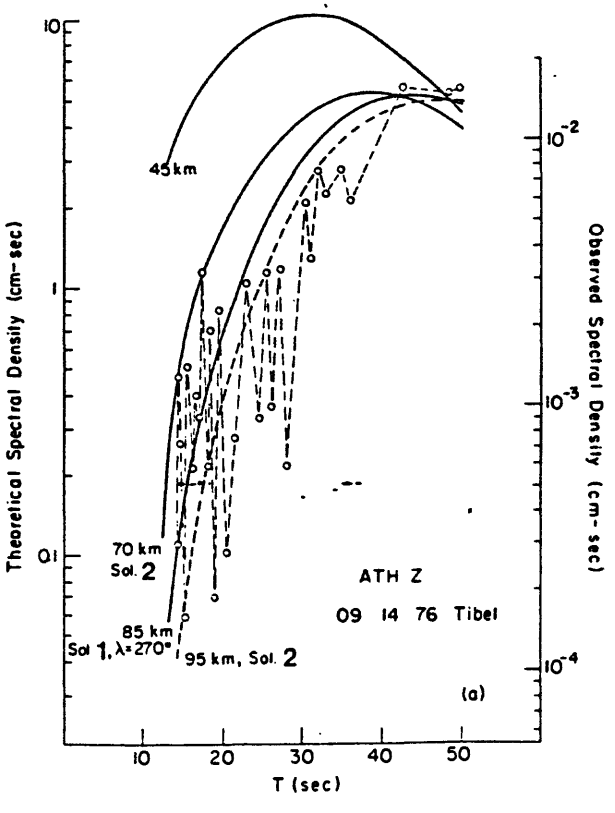
Theoretical Spectral Density (cm-sec)
Observed Spectral Density (cm-sec)
T (sec)
45km
70 km
Sol. 2
85 km
Sol 1, λ=270°
95 km, Sol. 2
ATH Z
09 14 76 Tibel
(a)

Fig. 5

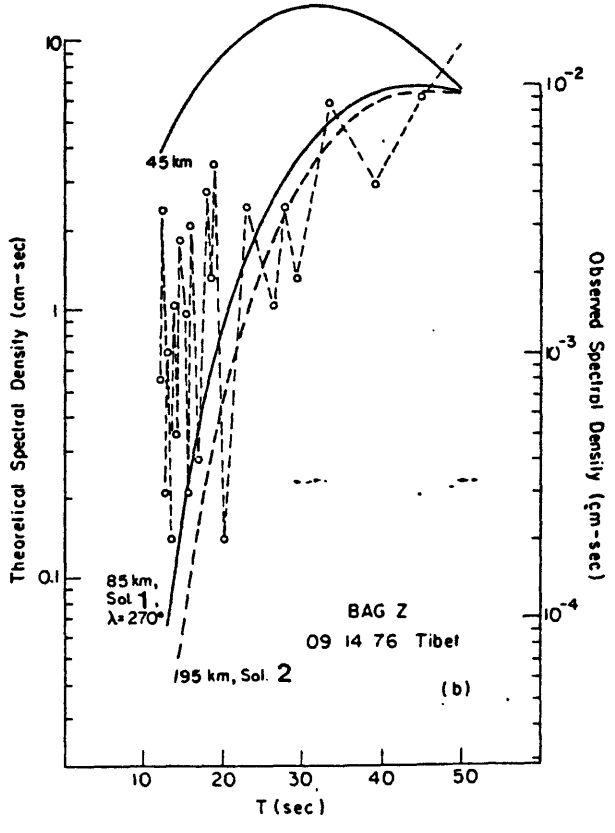
10
1
0.1
45 km
85 km,
Sol. 1,
λ=270°
195 km, Sol. 2
BAG Z
09 14 76 Tibet
(b)
10
20
30
40
50
T (sec)
Theoretical Spectral Density (cm-sec)
Observed Spectral Density (cm-sec)
10^{-2}
10^{-3}
10^{-4}

Fig. 5
(cont.)

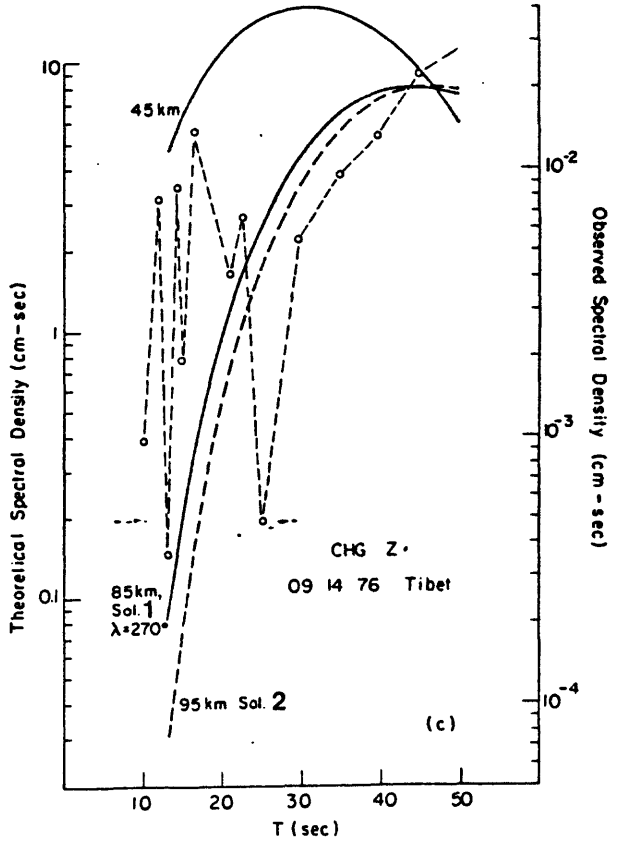
10
1
0.1
45km
85km,
Sol. 1
λ=270°
95km Sol. 2
CHG Z
09 14 76 Tibet
(c)
10
20
30
40
50
T (sec)
Theoretical Spectral Density (cm-sec)
Observed Spectral Density (cm-sec)
10-2
10-3
10-4

Fig. 5
(Cont.)

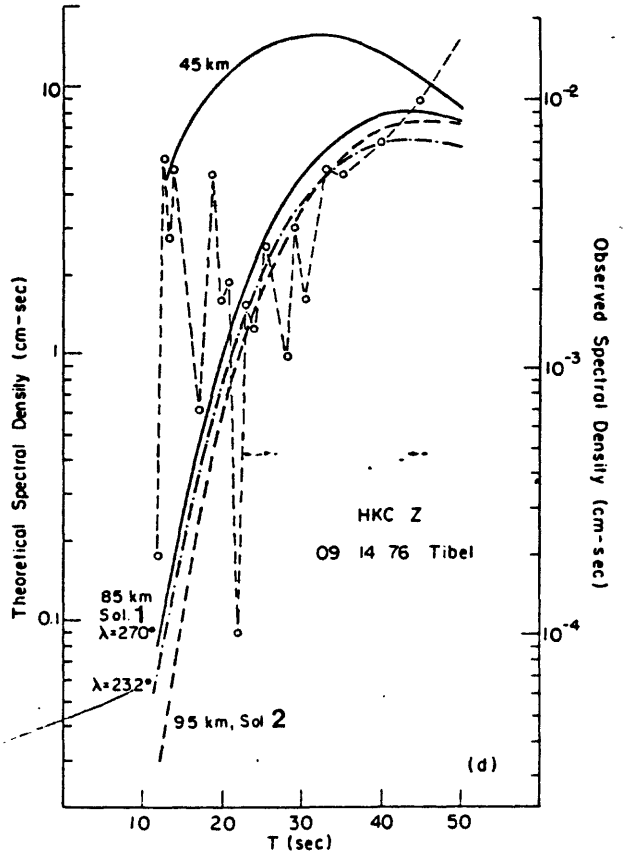
45 km
10
0.1
Theoretical Spectral Density (cm-sec)
Observed Spectral Density (cm-sec)
10^{-2}
10^{-3}
10^{-4}
HKC Z
09 14 76 Tibet
85 km
Sol. 1
λ=270°
λ=232°
95 km, Sol 2
(d)
10
20
30
40
50
T (sec)

Fig. 5
(Cont.)

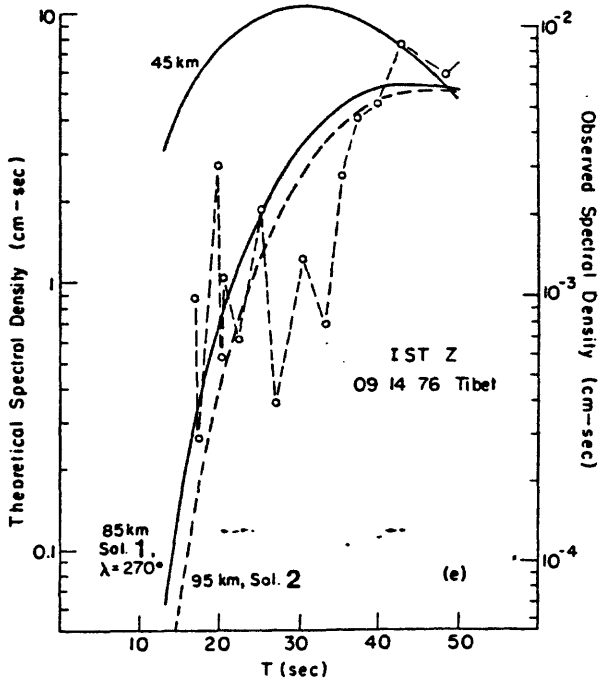
10
1
0.1
45 km
85km
Sol. 1.
λ = 270°
95 km, Sol. 2
(e)
IST Z
09 14 76 Tibet
10
20
30
40
50
T (sec)
Theoretical Spectral Density (cm-sec)
Observed Spectral Density (cm-sec)
10-2
10-3
10-4

Fig. 5
(Cont.)

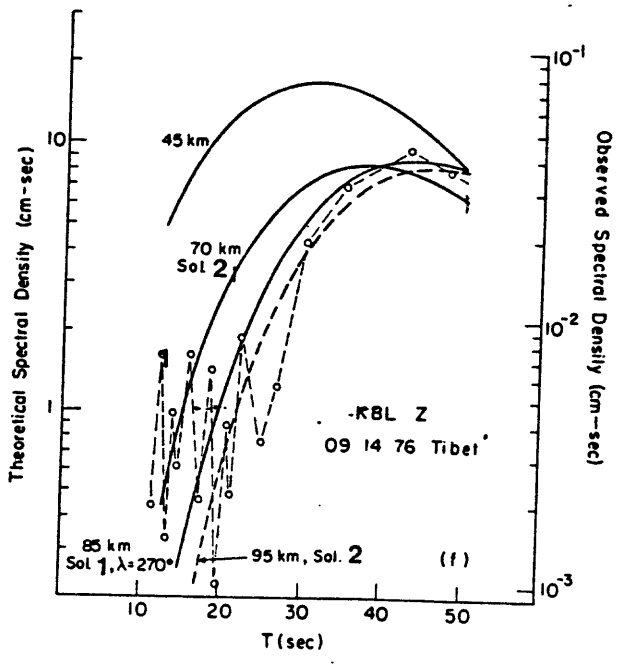
Theoretical Spectral Density (cm-sec)
Observed Spectral Density (cm-sec)
T (sec)
45 km
70 km
Sol 2
85 km
Sol 1, λ=270°
95 km, Sol. 2
KBL Z
09 14 76 Tibet
(f)
10
1
10^-1
10^-2
10^-3
10
20
30
40
50

Fig. 5
(Cont.)

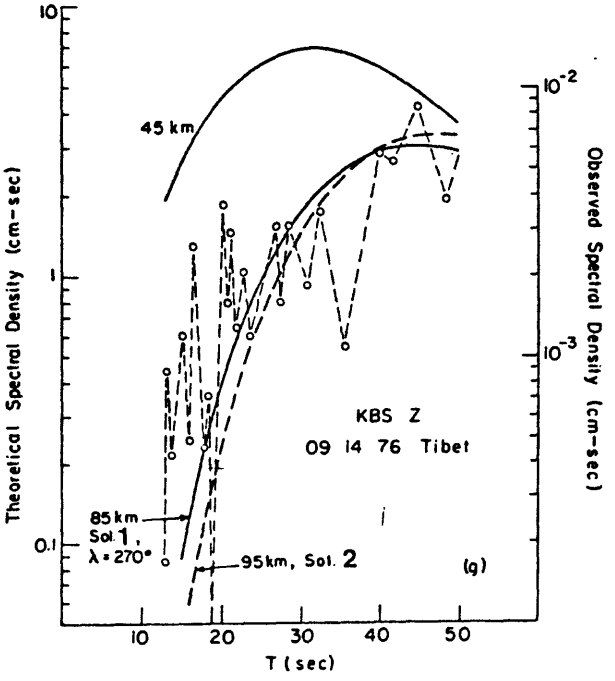
10
1
0.1
45 km
85 km
Sol. 1,
λ = 270°
95km, Sol. 2
KBS Z
09 14 76 Tibet
(g)
10
20
30
40
50
T (sec)
Theoretical Spectral Density (cm-sec)
Observed Spectral Density (cm-sec)
10^{-2}
10^{-3}

Fig. 5
(Cont.)

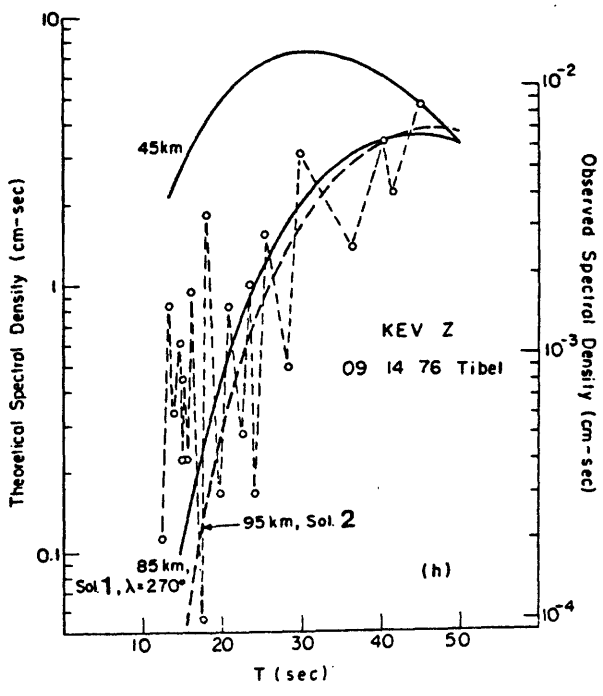
10
1
0.1
Theoretical Spectral Density (cm-sec)
45km
KEV Z
09 14 76 Tibet
95km, Sol. 2
85km,
Sol. 1, λ=270°
(h)
10
20
30
40
50
T (sec)
10^-2
10^-3
10^-4
Observed Spectral Density (cm-sec)

Fig. 5
(Cont.)

77

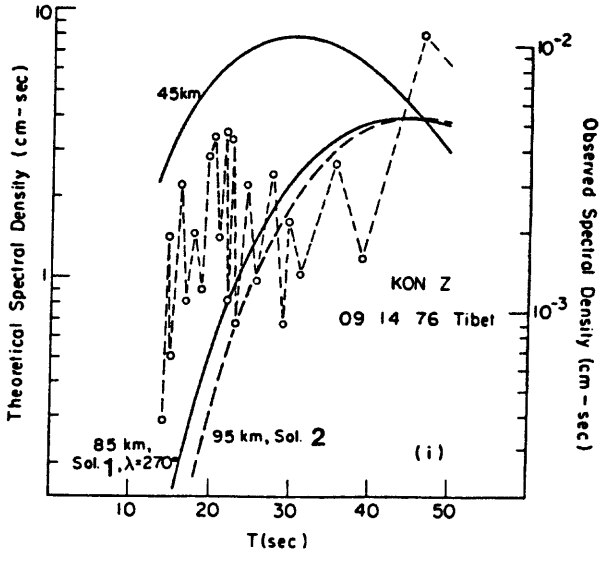
10
45km
10^{-2}
KON Z
09 14 76 Tibet
10^{-3}
95 km, Sol. 2
85 km,
Sol. 1, λ=270°
(i)
10
20
30
40
50
T(sec)
Theoretical Spectral Density (cm-sec)
Observed Spectral Density (cm-sec)

Fig. 5
(cont.

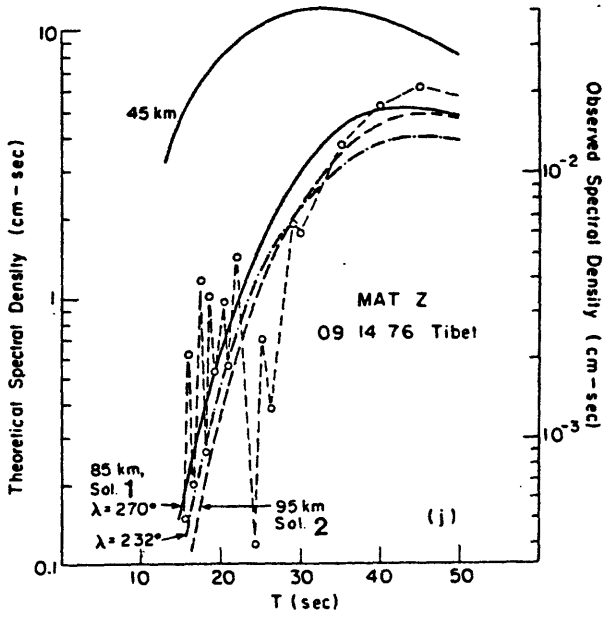
10
1
0.1
45 km
MAT Z
09 14 76 Tibet
85 km,
Sol. 1
λ = 270°
λ = 232°
95 km
Sol. 2
(j)
10
20
30
40
50
T (sec)
Theoretical Spectral Density (cm - sec)
Observed Spectral Density (cm - sec)
10^{-2}
10^{-3}

Fig. 5
(cont.)

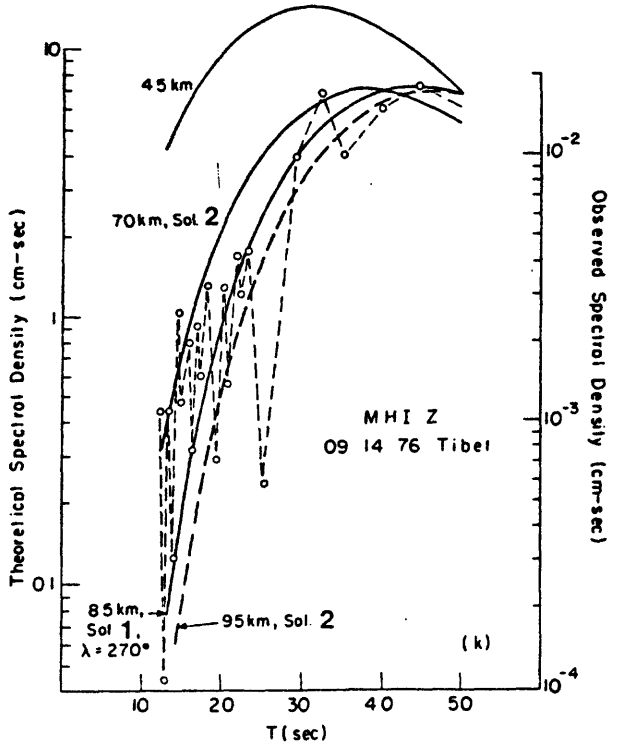
45 km
70km, Sol 2
85km, Sol 1, λ=270°
95km, Sol. 2
MHI Z
09 14 76 Tibet
(k)
Theoretical Spectral Density (cm-sec)
Observed Spectral Density (cm-sec)
T(sec)
10
1
0.1
10
20
30
40
50
10^{-2}
10^{-3}
10^{-4}

Fig. 5
(Cont.)

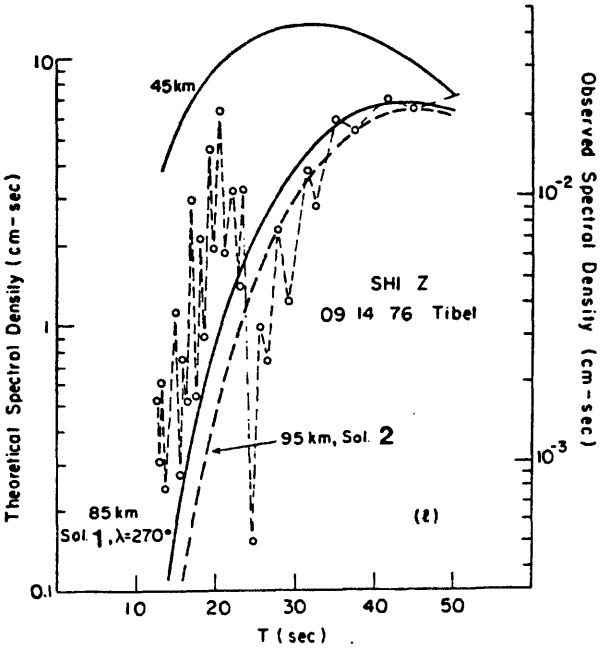
Theoretical Spectral Density (cm-sec)
Observed Spectral Density (cm-sec)
10
1
0.1
10^{-2}
10^{-3}
45km
SHI Z
09 14 76 Tibet
95 km, Sol. 2
85 km
Sol. 1, λ=270°
(ℓ)
10
20
30
40
50
T (sec)

Fig. 5
(Contd.)

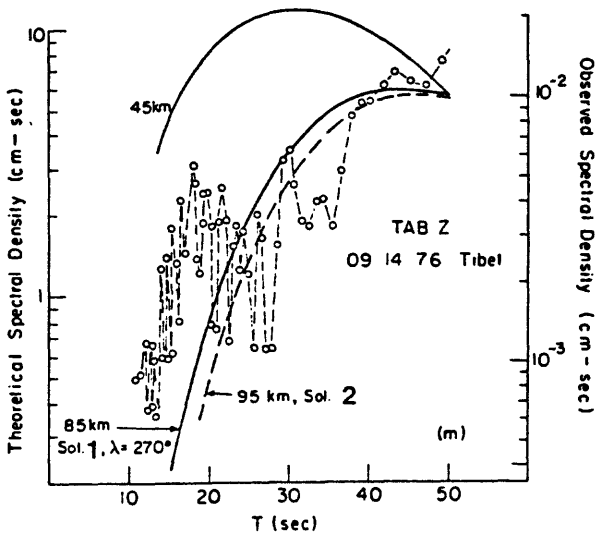
Theoretical Spectral Density (cm-sec)
Observed Spectral Density (cm-sec)
10
1
10^{-2}
10^{-3}
45km
TAB Z
09 14 76 Tibet
95 km, Sol. 2
85km
Sol. 1, λ= 270°
(m)
10
20
30
40
50
T (sec)

Fig. 5
(Cont.)

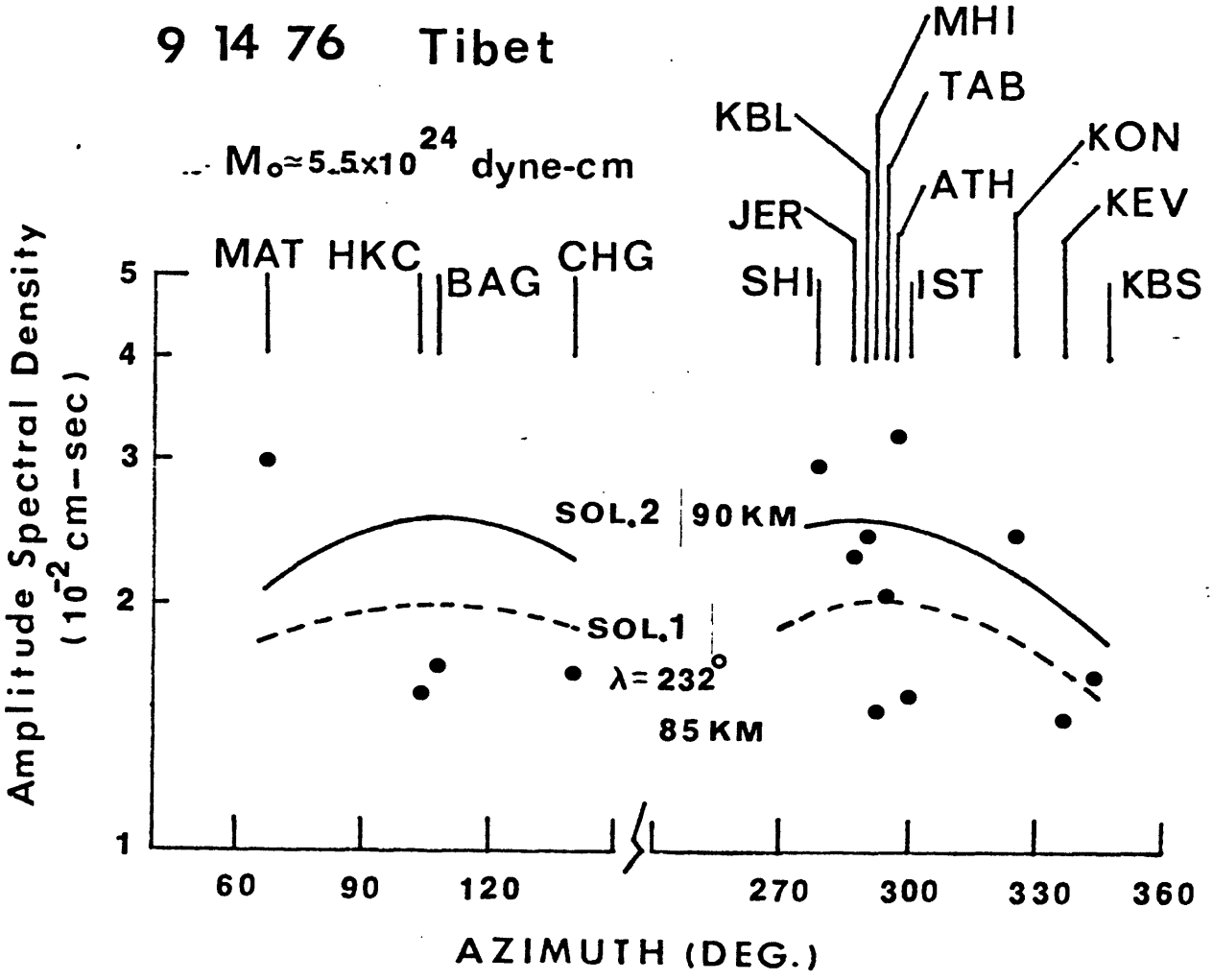
9 14 76 Tibet
$M_o \simeq 5.5 \times 10^{24}$ dyne-cm
MHI
TAB
KBL
KON
ATH
JER
KEV
SHI
IST
KBS
MAT
HKC
BAG
CHG
SOL.2
90 KM
SOL.1
λ = 232°
85 KM
Amplitude Spectral Density
(10^{-2} cm-sec)
5
4
3
2
1
60
90
120
270
300
330
360
AZIMUTH (DEG.)

Fig. 6

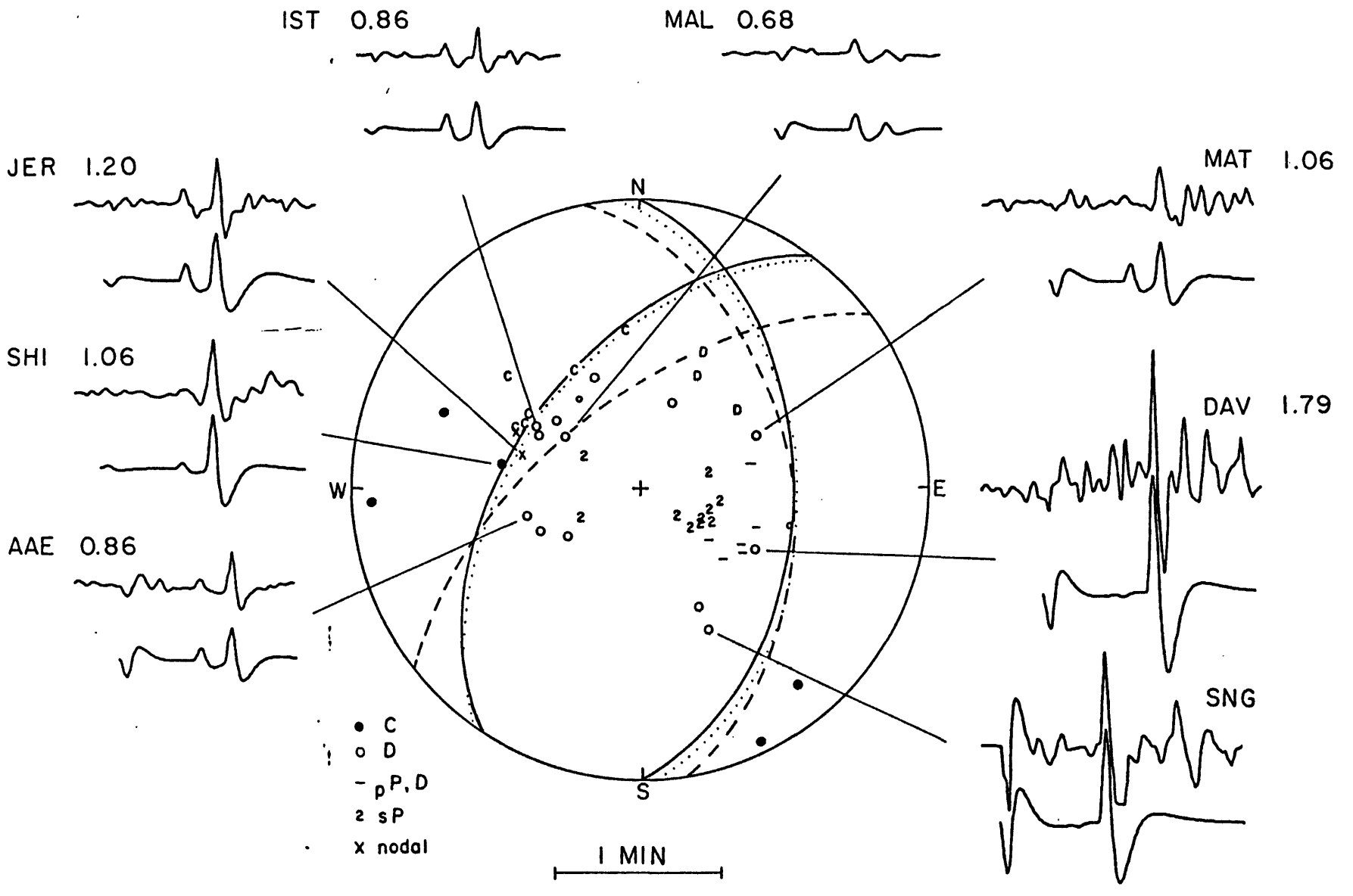

September 14, 1976 Tibet 29.81° N, 89.57°E 90 km

Fig. 7

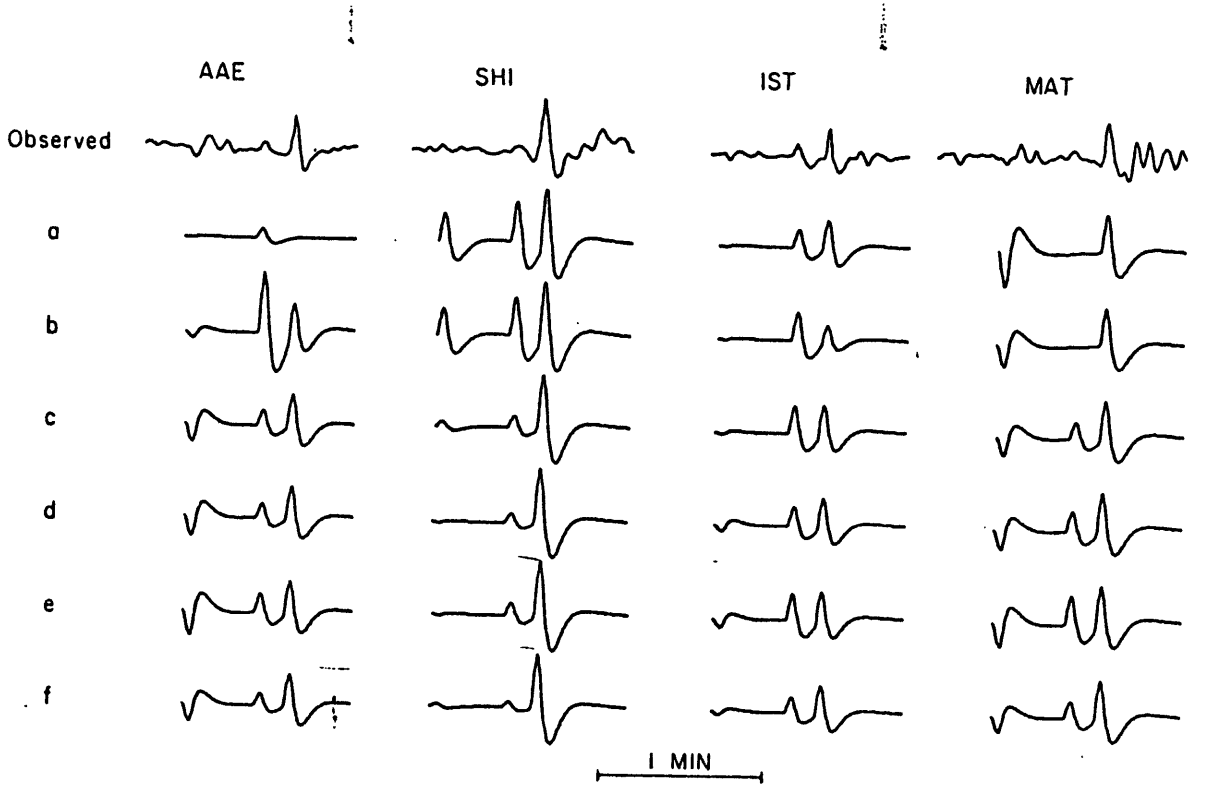

Fig. 8

The Geological Society of America
Telephone: (303) 447-2020

See instruction sheet for deadlines and addresses

CLASSIFICATION 3

You must specify one. If more than one category is of practical interest, indicate your order of preference by numbers. Be specific.

archaeological geology
coal geology
economic geology
engineering geology
extraterrestrial geology
general geology
geochemistry
geology education
geomorphology
(geophysics)
geoscience information
history of geology
hydrogeology
marine geology
mathematical geology
mineralogy/crystallography
paleontology/paleobotany
petrology
  experimental
  igneous
  metamorphic
Precambrian geology
Quaternary geology
sedimentology
  sedimentary petrology
stratigraphy
structural geology
(tectonics)
volcanology
OTHER
_____
_____
_____

ABSTRACT FORM

Exact format shown on instruction sheet must be followed.

Lucile Jones, Department of Earth and Planetary Sciences, Massachusetts Institute of Technology, Cambridge, Mass. 02139
Wang Biquan and Xu Shaoxia, Institute of Geophysics, Academia Sinica, Peking, People's Republic of China

We have examined the locations and mechanisms of the foreshocks to the 4 February 1975 Haicheng earthquake. The foreshocks were located using four stations relative to a master event. All occurred within 5 km of each other. There appears to be two clusters of foreshock activity. The largest with the larger foreshocks appears to form one trending north-northeast. The second cluster is more dispersed and lies to the northwest of the first. The mainshock rupture plane trends west-northwest but with a cluster of aftershocks trending north-northeast from the mainshock. Thus it is possible that the majority of the foreshocks occurred on a different plane from the mainshock.

We also examined the amplitude ratios (Ap/As) recorded at each station. While the ratios were relatively constant at the more distant (Δ=100-200 kilometers) stations, two very different waveforms were recorded throughout the sequence at Yingkou (Δ=20 kilometers). However, if the foreshocks did occur on two planes as suggested by the locations of the epicenters, because the two planes are almost but not quite perpendicular, the fault plane solutions for events on the two planes would be quite similar. Theoretically the slightly different fault plane solutions of the mainshock and the largest foreshock would produce relatively consistent ratios at the distant stations but two different ratios similar to ours at Yingkuo. However, a definite correlation between the different waveforms recorded at Yingkuo and the two clusters of activity could not be made.

☒ Oral ☐ Poster ☐ Either

☒ Symposium Earthquake Prediction
(title of symposium for which abstract was invited)

PLEASE NOTE: All invited symposium abstracts (original plus two copies) must be sent to the organizers of the respective symposia according to deadlines established by symposium organizers.

Speaker Lucile Jones

GSA Member ☐
GSA Student Associate ☐
Member of Society Associated with GSA ☐ Which _____
Nonmember ☒

I will be available to serve as a cochairman for a technical session on or concerning _____

For correspondence purposes (not to be published) my address is _____

Phone numbers and dates where speaker can be contacted _____

Final Technical Report

A. Same as Semi Annual.

B. With regard to foreshocks, Lucile Jones returned to China to work with Wang Biquan and Xu Shaoxie. They reread some seismograms for the Haicheng seires and obtained data from some other stations that they had not examined before. They are in the process of completing a study of the relative locations of foreshocks to the mainshock.

Rufus Catchings and Thomas Fitch studied seismicity preceding large events in the western Pacific. In some cases changes in the seismicity preceding large events can be seen, in others it cannot. They are in the process of finishing this study.

With regard to other precursors, Lucile Jones and Peter Molnar (supported separately from this grant), together with Deng Qidong and Jiang Pu, studied changes in ground water and anomalous animal behavior before the Haicheng earthquake. They made maps of their observations for different time periods and studied their possible interrelations. A manuscript was in the final throws of preparation when its preparation was interrupted by this report.

C. The major conclusion is that careful studies of individual earthquakes are essential. Detailed mapping of seismicity and other precursors are particularly important.

D. Bibliography: Nothing since the last report.

E.

F. One obvious implication is that more careful studies of ground water and animal behavior are needed if these observations are to be used in a quantitative understanding of earthquakes.

第2卷 第1期 地 震 地 质 Vol.2 No.1
1980年3月 SEISMOLOGY AND GEOLOGY Mar 1980

在地震孕育和发生过程中共轭断层活动的作用*

章光月 邓起东 蒋 溥

（美国，麻省理工学院）（中国，国家地震局地质研究所）

摘 要

根据海城、唐山和松潘—平武地震的地震前兆、地震序列和地质构造资料，提出了在地震孕育和发生过程中，不仅主震断层面有明显的活动，与之共轭的另一组断层面也有重要作用。在震中区，前震和余震可能分布于一对共轭断层面上，而不只是局限于主震断层面。地震前兆的分布范围存在于比震中区更为广大的一个区域内，该区内共轭断层网络中的某些断层带常成为前兆异常分布带或集中区。其形成原因可以用区域应力场中应力集中和沿共轭剪切网络所产生的破裂及滑动来解释。

中国板内主要地震的断层面解说明这些地震是它所在构造区应力场作用的结果[1,2]。它们大致可分成两种类型：第一种类型的地震发生于板内断块的主要边界断裂带上，它们与区域性活动深、大断裂带或断陷盆地带有明确的关系，如1973年2月7日四川炉霍7.9级地震发生于川滇断块北界的鲜水河断裂带中；第二种类型的地震并不发生在区域性活动断裂带上，而是发生于次级断裂带上，例如唐山地震（$M=7.8$级）就是这样。虽然唐山地区四条主要的断层自第四纪以来都有明显的活动，但1976年7月28日的大震却发生于这四条活动断裂所围限的菱形断块内部一条规模较小的（长40公里左右）断层上[3]。后一类地震多数发生在断块内部或地质结构复杂的构造部位。

值得注意的是，在整个地震序列孕育和发生的过程中，在震中区，似乎主震断层面并不是唯一活动的一个断层面，因为地震前兆、前震和余震除与主震断层面密切相关外，还常常沿着与之共轭的一组断层分布。地震前兆常有一个更广泛的分布范围，并与一定区域内不同方向的构造带及它们的组合特点密切相关。地震前兆场可能大大超过震源区的范围，其分布和演化特征则取决于该地区构造应力场及具体的地质结构。

本文的前一作者与国家地震局地球物理研究所王碧泉、许绍燮共同研究了海城地震前震特点[1]，并在后两位作者研究的基础上[1,2]，共同研究了辽宁海城、河北唐山和四川松潘—平武等地震短临前兆的空间分布与地质构造的关系，这些地震均为第二种类型的地震。

---

* 据中美两国科学交流协定，美国麻省理工学院交流学者L.琼斯女士（Lucile, M. Jones，汉名章光月），于1979年5—7月在中国国家地震局地质研究所，与副研究员邓起东和助理研究员蒋溥共同进行了地震前兆和地质构造关系方面的合作研究，本文即为研究成果之一。——编者注。

1) 章光月等，1979，海城地震前震系列的研究。

2) 蒋溥、邓起东，1979，海城—唐山地震系列孕育过程中前兆场演化特点及其构造力学条件。

1975年2月4日海城地震($M=7.3$)

辽宁地区的地质构造受两组近于相互垂直的活动断裂所控制(图1)，其中最基本的断裂系的走向为北北东向，它是中国东部主要构造方向之一；另一组方向的断裂为北西向，这是一组规模相对较小的破裂，它常常被北北东向断层所限制。

下辽河断陷受北北东向断层所控制，其中牛居—油燕沟深断裂是最主要的一条。震区内，在下辽河断陷和辽东隆起边界上有金山岭和双台子河—赵家堡子断裂。它们可能是纵贯华北和东北断块区的郯城—庐江深断裂的一部分。在辽东隆起的内部，还有其他北北东向断裂分布(图1)。震区附近的北西向断裂有大洋河断裂，其西端终止于震区。

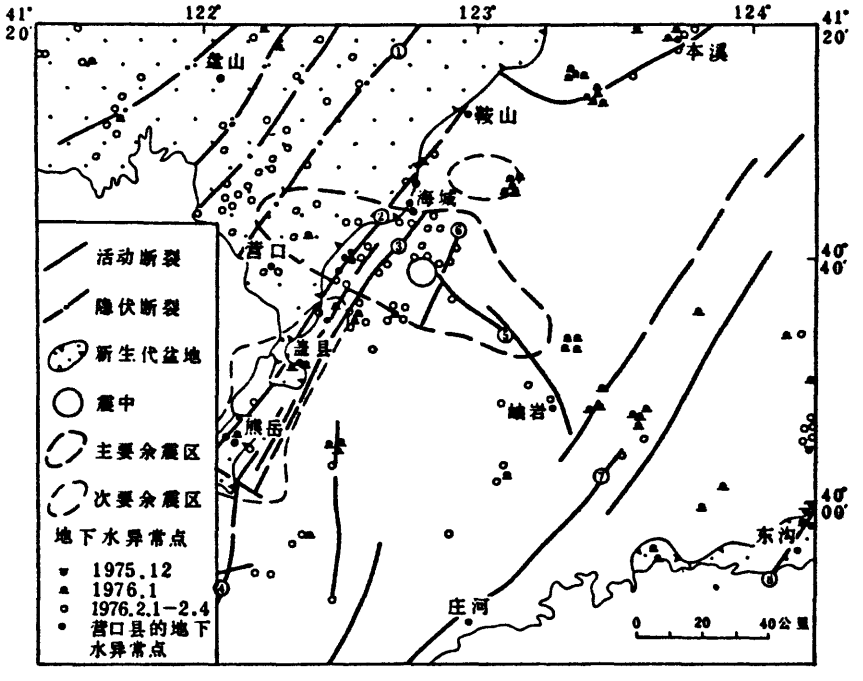

图1 海城地震区地质构造与地下水异常点及余震分布图

①牛居—油燕沟深断裂，②金山岭断裂，③双台子河—赵家堡子断裂，④金州大断裂，⑤大洋河大断裂，⑥析木河断裂，⑦庄河大断裂，⑧鸭绿江大断裂

海城地震发生于北西向大洋河大断裂与牛居—油燕沟深断裂的一个"汇而不交"的构造部位，主震微观震中正好位于大洋河断裂的西北端，而余震主要分布于主震震中的北西西方向(图1)，它与主震等震线极震区长轴的走向一致。此外，沿这一北西西方向，还产生了几条雁行式排列的地震裂缝带，其位移方向表明这条北西西向构造发生了左旋错动。所以，可以认为北西西方向是这次地震的主要断层面，可视其为一条新的破裂[1]。

海城地震P波初动解求出的两组节面走向分别为北22°东和北68°西，主压应力方向为北67°东。前者为右旋滑动，后者为左旋滑动[1]。这两组方向与前述北西西向地震破裂和北北东向区域断裂方向大体一致。

虽然，主要的断层活动是北西西向，但以下证据说明北北东向断层在地震前、后也曾经

发生活动，或者至少受到应力集中的影响。

首先，一部分前震与余震发生在北北东向面上。前震虽然集中发生在主震震中附近的五公里范围内，但它们却成独立的两个条带分布，其中的一个条带即成北北东向延伸，条带长度达 3 公里[1]，其位置大致在析木河谷以西。此外，虽然主要余震沿北西西方向发生，但也有少量余震在区内成北北东向分布，如主震震中东北的什司及西南的盖县、熊岳等地均有2—3级左右的余震分布(图 1)。前者的位置正好与北北东向前震条带向北的延伸方向一致，后者则分布在金山岭北北东向断裂的南段。

北北东向前震条带分布区出露元古代片岩系，虽然断层存在的证据还有待进一步研究，但该地区存在一条走向北北东的直线型河谷，并有明显的三角面存在，河谷旁的片岩中有走向北 20°东左右的较为发育的节理和小的破碎带。所以，沿析木河谷可能存在一条北北东向的断层。

其次，海城地震前兆场具有相当大的范围，其半径可达 400—500 公里，异常点的分布主要受区内北北东向和北西向断裂带所控制[1]。从短临前兆来看，辽宁地区的前述两组构造的控制作用十分明显，一个非常明显的现象是地下水异常，包括水位变化、水味和颜色的改变、冒气泡、水变浑及水打漩等等[3]。这些现象开始于主震前 10 周，但集中于震前几天。主要的异常沿着主震断层面成北西西向分布(约占总异常点 241 个中的 74%)，但也有许多异常点分布于北北东方向，与金山岭、双台子河—赵家堡子和金州断层一致，如果把两组断裂交汇区(震中区)中的异常点包括在内，则北东方向异常点占总数的 60%(图 1)。此外，沿辽东地区一些北北东向断裂都有地下水异常点的零星分布。值得注意的是，1974 年底前后一个多月的 20 个异常点主要发生于丹东地区，沿北北东向鸭绿江断裂分布，1975 年 1 月 80 个异常点主要出现于北西向构造带内，但北北东带内的鞍山一带也有水位变化，2 月 1 日至 4 日临震前的 140 个异常点则主要集中于北西西向的震中区。但此时，位于金山岭断裂带北段的鞍山汤岗子温泉却三次发生历史上从未记录过的断流现象。此外，营口县地震办公室所研究的、对海城地震序列前兆反应比较敏感的 5 口水井，也都位于北北东向的金山岭断裂带上(图 1)。

海城地震孕育过程中其他一些短临前兆异常也具有同样的分布特点，如动物习性异常的分布虽然亦以北西西方向为主，但沿北北东向金州断裂、金山岭断裂和鸭绿江断裂亦有分布。此外，沿北西西向主震断层带上尚有水氡、自然电场、地光及地下气体等多种异常，在震区及其附近的一些北北东向断裂带上也有若干观测点出现同类异常。

1976 年 7 月 28 日唐山地震($M=7.8$)

唐山地震发生于华北断块区内的燕山隆起带和华北平原断陷的过渡带上，这个过渡带是一组近东西或北东东向的阶梯状断裂带，被北北东和北西向构造所割切，并形成次一级地堑和地垒，唐山次级断块就是其中之一。唐山断块四周被具有新活动的四条深、大断裂所围限，成为一个北东东向的菱形块体[3]。正如前面所指出的，唐山地震发生于这一菱形断块内部的一条北北东走向的唐山断裂带上。

唐山地震形成了一条长 8 公里的北北东向右旋地震裂缝带，最大水平位移达 2—3 米。主震前没有前震，余震分布与主震断层面的分布大体一致。但在唐山断裂带的南、北两端，分

1) 同 19 页 1)。

别形成余震密集区，并在这两个余震密集区中分别发生了7.1和6.9级两个强余震，其中宁河6.9级余震断层面被认为是北西向，和该余震密集区方向一致。从唐山地震主震 P 波初动解来看，主压应力方位为北65°东[6]。北北东和北西向两组断裂面是一对共轭的剪切破裂面。

虽然唐山地震前兆的空间分布比较复杂，甚至有些尚难看出明显和规则的图象。从前兆的时间演化过程来看，海城地震后，辽宁地区的某些异常有所恢复，但京津唐地区某些前兆异常却继续发展，从1976年4月前后开始进入短期变化阶段[1]。这些异常大致沿着本区北东、北西和东西向构造分布，显示出前兆分布和地质构造的某些关系，其中最明显的是电阻率的变化。在以唐山为中心的200公里范围内，14个形变电阻率观测台中有9个自1973年、1974年先后出现长趋势性的下降异常，它们在地理位置上形成了一个南北宽约70公里，东西长约300公里的形变电阻率下降区，其中以唐山、马家沟和昌黎三个台下降幅度最大，至唐山地震前分别达5.5%、17.6%和6.4%。1975年12月，电阻率异常显示出一定的条带状分布，根据1976年7月唐山地震前 $\Delta\rho_s/\rho_s$ 异常等值线图[7]可以明显地看到，整个异常分布范围超

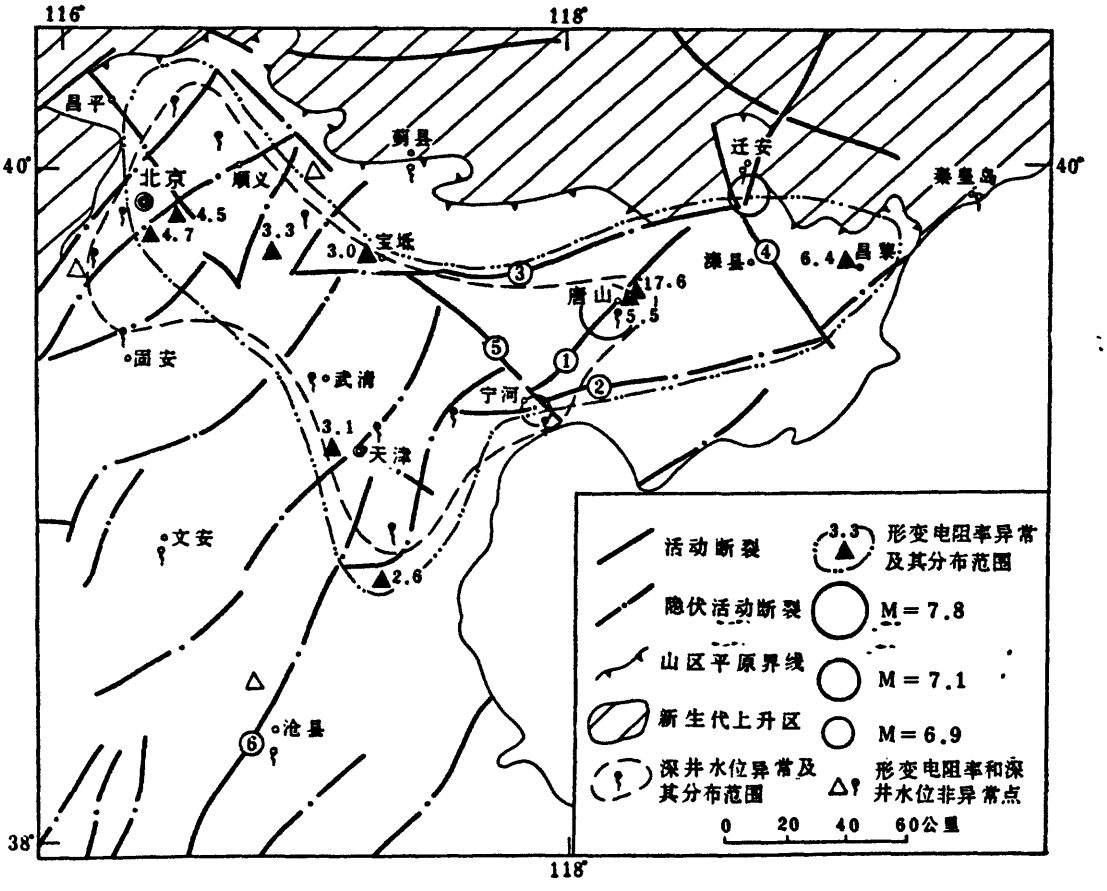

图2 唐山地震区地质构造及部分前兆分布图

1.唐山断裂，2.宁河—昌黎深断裂，3.丰台—野鸡坨大断裂，4.滦县—乐亭大断裂，5.蓟运河深断裂，6.沧东大断裂

1) 河北省地震局，1977，唐山地震短临前兆异常。

出了唐山震区的范围，异常大致沿天津—唐山—昌黎(北东向)和天津—北京(北西向)两个条带分布。这两个异常条带与唐山地震的余震及唐山地震前京津唐地区地震活动的分布[8]大体相同，也与唐山地震前二、三年内本地区的深井水位出现的长期下降异常的分布及以天津、宁河为中心的地下水异常逐步向外扩展的趋势相一致(图2)。几种异常呈一定方向的条带分布可能是因为本区北东和北西向两组共轭断裂震前滑动的影响。

唐山地震的临震宏观异常出现较晚，在震前一、二天才形成高潮[1]。异常种类和主要表现与海城地震临震异常种类和现象类似。震前地下水宏观异常波及唐山、天津、北京及附近地区，其中以唐山地区最为突出，震前16小时的地下水异常主要集中于震中区，其分布方向为北北东，并形成大致和唐山断裂带相平行的几个条带。70—80%的动物习性异常集中于临震前一天之内，有四个分布较为集中的条带，它们主要与唐山主震断层面及唐山断块边缘断裂有密切的关系。上述宏观异常点的分布和发育同样反映出在唐山地震前，除了唐山主震破裂面显示出强烈活动外，唐山断块周边大断裂也显示出一定的活动。

1976年8月(16日、22日、23日)松潘—平武地震($M=7.2$、6.7、7.2)

松潘—平武地震序列发生于四川龙门山断裂带西侧的虎牙断裂上，它发生于唐山大震以后仅仅三周，是一个第一次成功地进行了临震预报的无前震的7级大震。这个地震的中期预报主要是根据地震活动性特点及一些地壳形变和水氡含量变化等异常进行的。临震几天的预报大部分根据"宏观异常"，其中包括水位的变化及冒泡、动物习性异常、地声和火球等。这些异常主要沿龙门山断裂带分布而并未发生在大震断裂带上。

龙门山断裂带由三条走向北东的逆断层所组成，并具有右旋走滑特征，它是中国西部青藏断块东界的一部分。在这一断裂带的北段西侧，发育有近南北向和北北西向的岷江断裂和虎牙断裂，均属逆断层。1960年四川漳腊6¾级地震和1933年四川迭溪7½级地震就发生在岷江断裂带上，1976年的松潘—平武地震序列中的三个主要地震则是沿北北西向的虎牙断裂由北向南依次发生的。从P波初动解[9]的结果来看，地震的主压应力轴方位近东西，虎牙断裂和龙门山断裂虽然规模相差较大，但它们构成现代应力场中的共轭断裂面，并分别具有左旋和右旋滑动的特点。

在地震短、临前兆方面，直到地震前二、三天为止，震中地区基本上未见明显的前兆活动，但在外围地区的断裂带上，于6—7月相继出现了自然电场和水氡含量异常，其中以康定表现最突出，该地区是四川三条活动断裂的汇合地区[10]，似乎构成了一个前兆灵敏点。更突出的是3月到8月13日的宏观异常，主要沿龙门山断裂带发生，看来它似乎是与大震前伴随断裂的有震和无震滑动(蠕动)而出现的(图3)。

根据四川省地震局的调查，3、4、5三个月以地下水异常为主的宏观异常出现于龙门山断裂带的中南段，远离震中达200公里以上，包括矿物含量的变化、井水水位变化、井水变浑和冒气泡等。在大震发生前，于6月16日—6月底、7月18日—28日和8月4日—13日，先后在龙门山断裂带的南段、中段和北段形成三次宏观异常高潮，第一次高潮中发生的各种

1) 河北省地震局，1977，唐山地震短临前兆异常。

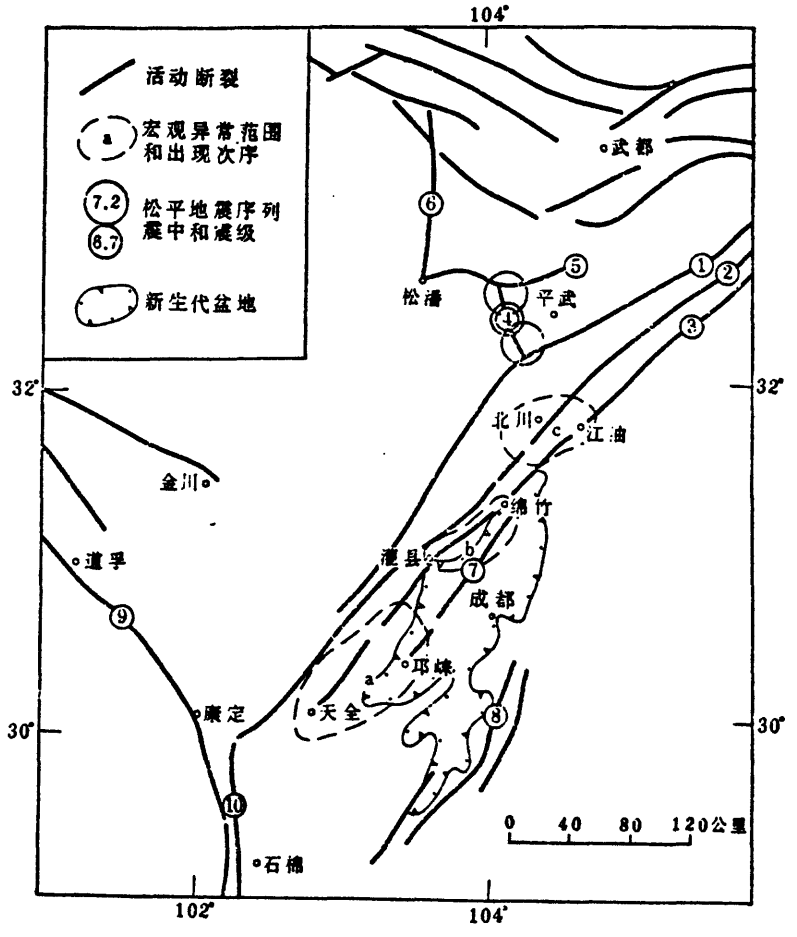

图3 松潘—平武地震区地质构造与宏观地震前兆分布图(宏观前兆分布区根据朱皆佐)

①②③龙门山断裂带，④虎牙断裂，⑤雪山断裂，⑥岷江断裂，⑦龙泉山大断裂，⑧绵竹—邛崃隐伏断裂，⑨鲜水河深断裂，⑩安宁河深断裂

类型异常达 192 起，第二次高潮出现各种类型异常约 133 起；第三次高潮中各种类型异常达 866 次，其中出现大量的动物习性异常行为。这几次宏观异常高潮沿断裂带向震中区移动，并且临近地震时异常数目增加。但在临震前两天，沿龙门山断裂带异常几乎消失(不管上述异常的实际情况如何，8 月 12 日发布的临震预报的范围包括了龙门山断裂带的中北段，并把这一地区列为重点监视的地区之一)。与此相对应的是，从 1975 年秋开始在未来震中附近地区就已经出现了某些异常，但其中平武县宏观异常从 76 年 1 月至 8 月 13 日仅 28 起。当 8 月14—16 日沿龙门山断裂带异常突然平静时，平武县异常却骤然增加，三天内达 100 起，异常一直延续到地震发生。

另一个地震前兆发生在虎牙断裂的西北方向，根据 1960 年和 1975 年两次水准测量结果比较，15 年内沿岷江断裂从松潘至南坪的 40 公里长的范围内相对上升了 312 毫米，说明在这一段时间内，松潘以东地壳上升，以西则下降，但虎牙断裂本身缺少资料。

结　　论

从中国以上几个板内地震资料来看，在地震孕育和发生过程中，区域性地质结构、区域构造应力场和地震前兆场彼此之间有着密切的关系。

首先，虽然这些地震似乎都位于板内断块的主要边界断裂所控制的地震带上，但主震的断层面并不直接就是这些断裂，而是一些与之相关的次一级断裂，从这些次级断裂的力学机制和区域断裂的关系来看，它们之间在成因上似乎有统一的力学条件。可能是因为板内地质构造的复杂性，使得不同方向构造的组合及某些特殊构造条件成为有利于应力集中的部位所致。在地壳结构破碎而复杂的华北断块区，这是一个十分值得注意的问题。

其次，在一定规模的断块区内，构造活动有统一的运动特征，这主要决定于不同地区的区域应力场。因此，在一定区域应力场的作用下，构造活动具有区域的概念，而不是某一条断裂的单独运动，所以，除发生主震的断层往往控制了前震、余震及大多数前兆以外，区内其他断层也会受该地区应力场的影响。它可以是平行于主震断层面的断层，也可以是在力学成因上有联系的与之共轭的另一组断层。在震中地区，这种与主震断层面共轭的断层面，也可以成为部分前震、余震活动的场所。前兆的分布范围可能存在于比震中区更广大的区域，彼此共轭的断层网络中的某些断层带成为地震前兆异常分布带或集中区。这种现象也可能存在于中长期的前兆异常场中，而对短临前兆异常场的影响似乎更加清楚。从地震孕育和发生的构造力学条件来看，这一现象也可以用区域应力场中由于地质结构的复杂引起应力集中及沿已有断层产生的有震或无震滑动来解释。当然，在时间非常短的临震宏观异常的高潮时刻，震中区的异常则占有最突出的地位。

第三，在地震孕育过程中，前兆异常区的迁移是一个值得注意的问题，这一点在三个地震中都存在，尤以松潘—平武地震最为突出。它很可能是在一个统一的构造应力场中，沿共轭断裂系的滑动成一定方向逐步发展、应力集中区的迁移(强化或减弱)及震源区应力集中程度不断加强所引起的。

承蒙中华人民共和国教育部、国家地震局和美中学术交流委员会、美国国际交流总署、麻省理工学院为我们提供了这一合作研究的机会，四川、辽宁和陕西省地震局提供了对松潘—平武、海城和1556年华县地震震区进行野外考察的方便，工作中助理研究员向宏发、魏顺民及张珍、唐荣昌、钟以璋、韩恒悦和王平安等工程师给予了很大帮助，谨致谢忱。

(1979 年 7 月收到)

参 考 文 献

〔1〕邓起东等，1976，关于海城地震震源模式的讨论，地质科学，3 期，195—204 页。
〔2〕邓起东等，1979，中国构造应力场特征及其与板块运动的关系，地震地质，1 卷，1 期，11—22 页。
〔3〕魏顺民等，1977，唐山地震区域构造背景和发震模式的讨论，地质科学，4 期，305—321 页。
〔4〕吴开统等，1976，海城地震序列的特征，地球物理学报，19 卷，2 期。
〔5〕朱风鸣等，1979，宏观异常及其对大地震预报的意义，1979年国际地震预报大会论文。
〔6〕邱群，1976，1976 年 7 月 28 日河北省唐山 7.8 级地震的发震背景及其活动性，地球物理学报，19 卷，4 期，259—269 页。
〔7〕赵玉林等，1978，唐山 7.8 级强震前震中周围形变电阻率的下降异常，地球物理学报，21 卷，3 期，181—190 页。
〔8〕张国民，1979，1976 年唐山地震($M=7.8$)的孕育过程和中期前兆的分析，1979 年国际地震预报大会论文。
〔9〕陈天长等，1979，1976 年 8 月 16 日松潘—平武地震的某些特点，1979 年国际地震预报大会论文。
〔10〕李坪等，1975，云南川西地区地震地质基本特征的探讨，地质科学，4 期，308—327 页。

THE IMPLICATION OF CONJUGATE FAULTING IN THE EARTHQUAKE BREWING AND ORIGINATING PROCESS

L.M. Jones
(MIT, U.S.A)

Deng Qidong and Jiangpy
(Institute of Geology, State Seismological Bureau)

(Abstract)

The earthquake sequence, precursory and geologo-structural background of Haicheng, Tangshan, Songpan-Pingwu earthquakes are discussed in this article. As we know that all these earthquakes occurred in a seismic zone controlled by the main boundary faults of a intraplate fault block. But the fault plane of a main earthquake is not the same faults rather a related secondary fault. They formed altogether a conjugate shearing rupture zone under the action of regional tectonic stress field. As to the earthquake sequence the foreshocks and aftershocks might be occurred on the conjugate fault planes within an epicentral region rather than limited in the fault plane of a main earthquake, such as the distribution of foreshocks and aftershocks of Haicheng earthquake. The characteristics of the long-, medium- and imminent term earthquake precursory anomalies of the three mentioned earthquakes, especially the character of well-studies anomaly phenomena in the electrical resistivity, radon emission, groundwater and animal behavior, have been investigated. The studies of these earthquake precursors show that they were distributed in an area rather extensive than the epicentral region. Some fault zones in the conjugate fault network appeared usually as distributed belts or concentrated zones of earthquake precursory anomalies, they can be traced in the medium-long term precursory field, but seem more distinct in the short-imminent term precursory anomalous field. These characteristics can be explained by the rupture and sliding originated along the conjugate shear network and the concentration of stress in regional stress field. Moreover, it is worthy to notice the migration of these precursory anomalies along the conjugate rupture zone in the earthquake-brewing process. The macroscopic precursory anomalies of the Songpan-Pingwu and Haicheng earthquakes did not appear first in the epicentral region, but emerged in a set of fault zone conjugated with the fault plane of main earthquake, or in a conjugate fault zone and their intersection region. These phenomena may be originated from the migration of stress-concentrated region and continuous concentration of stress in the earthquake source area. It is also possible that they were progressively initiated at a definite direction along the rupture zone and sliding caused by conjugate faulting.

It can be supposed that the effect of conjugate fault on the earthquake brewing and originating process is significant in theoretical studies of seismology and in predicting practice, it should be drawn public attention.

海城地震前震系列的研究

摘 要

本文研究了1975年2月4日海城前震系列的定位及机制。相对于一个基准地震，用四个台的p波对前震进行了相对定位。所有前震的位置很接近，相互距离约在不大于6公里的范围内。可看出前震位置有相对集中的两组，多数前震看来发生在基准地震以来，沿着NNE－SSW方向的一组中，且震级大于3.0的几个前震全下发生在这一组中，也可看出好像还有第二组前震，它位于第一组的北西方向。可能多数前震不发生在主震的破裂百中，而是在近于垂直于主震百的另一平百中。

通过分析各台的p波S波振幅比，本文还研究了前震的机制。在远些的台上（Δ≈100－200KM）振幅比相对为常数，在全个前震序列中营口台上（Δ≈20KM）都记到了两种相当不同的波形。还作了理论计标振幅比。似乎主震断层百解和最大前震断层百解计标的振幅比分别与营口台两种波形前震的实测振幅比相符合。在两种机制制和两组震中位置之间似可得出一定关系。

引 言

1975年2月4日海城地震（M＝7·3）获得比较成功的予报，在在种程度上是由于主震前四天开始发生了一个较大的前震系列，共记到500多个小地震〔1〕。这郑大的前震系列是很少见的一确实，海城前震系列是仅有的记录较好的前震系列之———我们不能奢望其他更多的地震也有这样的前震系列。然而很多大地震之前往往也有几个前震〔2〕，但是到目前为止，我们还只能事后来认识宅们。为了有效地予报，我们还需要研究在主震发生前如何从“正常的”震群中区分出前震。若某处发生了这样多的小地震，并不能像海城地震一样无可非议地认为是前震。正因为海城前震次数很多，宅提供了很好的机会来研究此问题。宅有大易地震系列的特性并与震群进行比较，这对于从事地震予报的人们可能是有所助益的。

作为地震学方曰中美合作研究工作的开始，进行了有关海城地震前震系列的研究。本工作有两个忘图，其一是试图测定主震发生前可识别的前震特性，以用于地震予测。因为前震是主破裂前大地发生形变的证据之一，本工作同时还作了地震机制方曰的研究。

本文发表的是合作研究的第一下结录，主要是研究了这个序列的两个主要特性，即地震的相对位置及其机制一后一特性主要是考虑了p波和S波波的振幅比，在另一文中〔3〕研究了序列有关的其他特性。

二、资料和方法

我们用了六个地震台的资料，其台站位置示于图一。除庄河台、草河掌台为垂直向外周期地震仪外，其余各台均为三分向外周期地震仪。地震仪记录纸走速都为120毫米／分，所以到时能测至0·1秒，仪口放大倍数约为105。

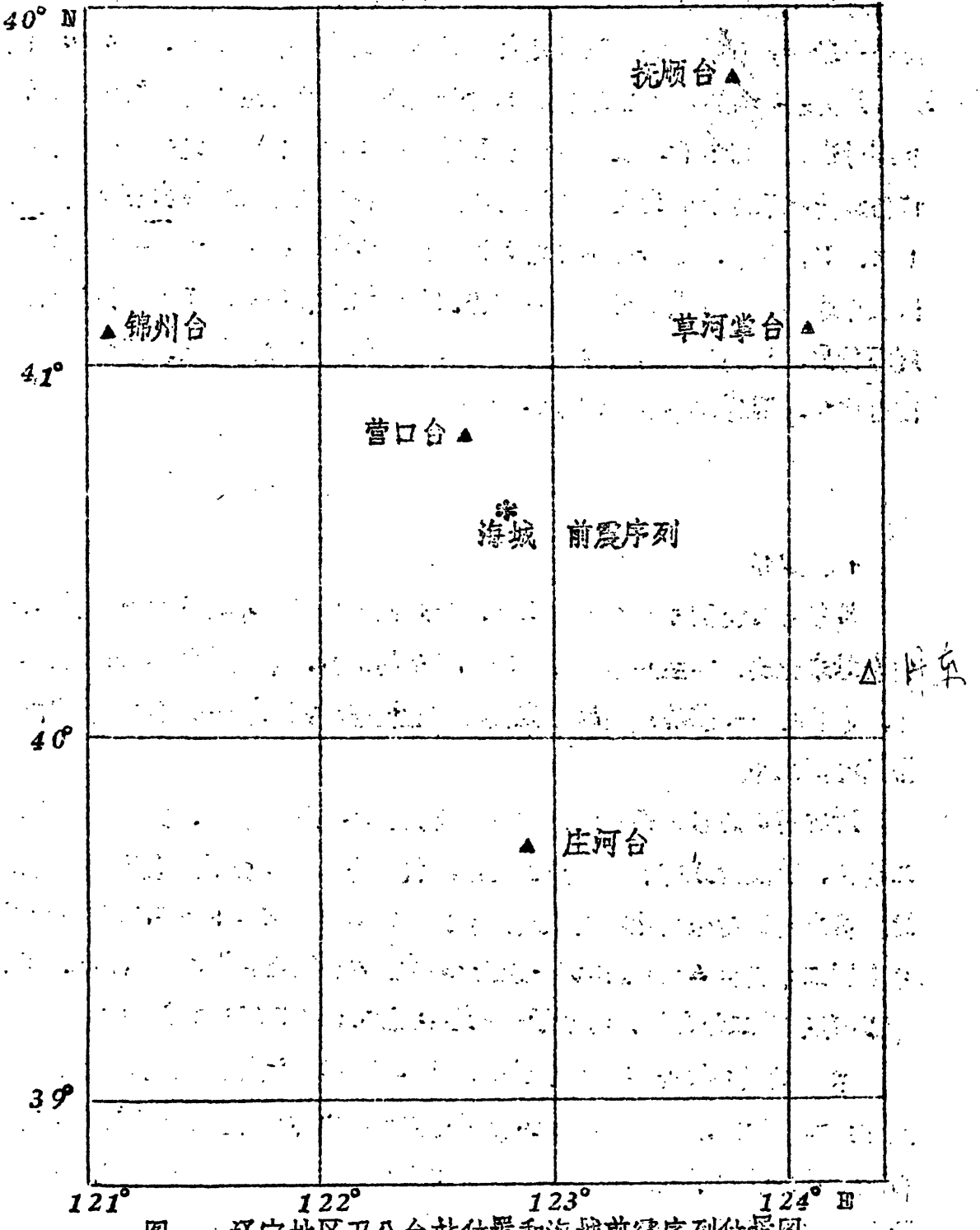

图一、辽宁地区下分台站位置和海城前震序列位置图

对75年2月3日19^{h}13^{m}的地震，用五个台（旅大台除外，因该台当时钟差有疑）的P到时定位，其各台残差均小于0.03sec 故取该震为基准地震，其他地震是相对于这个基准地震定位的。取四个台的p到时进行相对定位，求出各台p到时与基准地震p到时之差的平均值，该值加上基准地震的发震时刻取为该震的发震时刻。现需解出三个未知数（x，Y，h），而对四个台站可列出四个方程，每三个方程一组就可解出三个未知数，则共有四组，可解出四组位置；我们取其平均值为该震的震源位置，取其标准偏差为定位的误差。我们取营口、抚顺、庄河、锦州四台定位，因这四个台控制定位较好。

三、结　果

一、定位

虽然营口记到500多个前震，但是因为地震太小，大多数地震在其他台站未记到，在主震前26小时内发生的地震，我们能够定位的有34个。它们相对于基准地震的位置及其定位误差均列入表一，其相对震中位置画在图二中。

所有前震的位置很接近，相互距离约在不大于六公里的范围内。由图二看出，前震位置有相对集中的两组，虽然也可能是由于定位的误差引起的。多数前震看来发生在基准地震以东、沿着NNE－SSW方向的一组中（图二中记为A组中。）此外震级大于3.0的八个前震全下位于A组中，而且图中也看出好象有第二组前震，它位于第一组的北西方向（图二中记为B）。

主要的破裂面是沿着大多数余震发生的北西西方向〔1〕，而不是发生在如本文所指出的前震分布的主要走向北北东方向上。由于前震不够大前震断层面解能不能定得很准，有关文献中已测得了有所不同的前震断层面解，但都大体与主震相似（图三d）。然而由这些解可看到，沿主震的NWW面和上面给出的前震位置的NNE面的断层

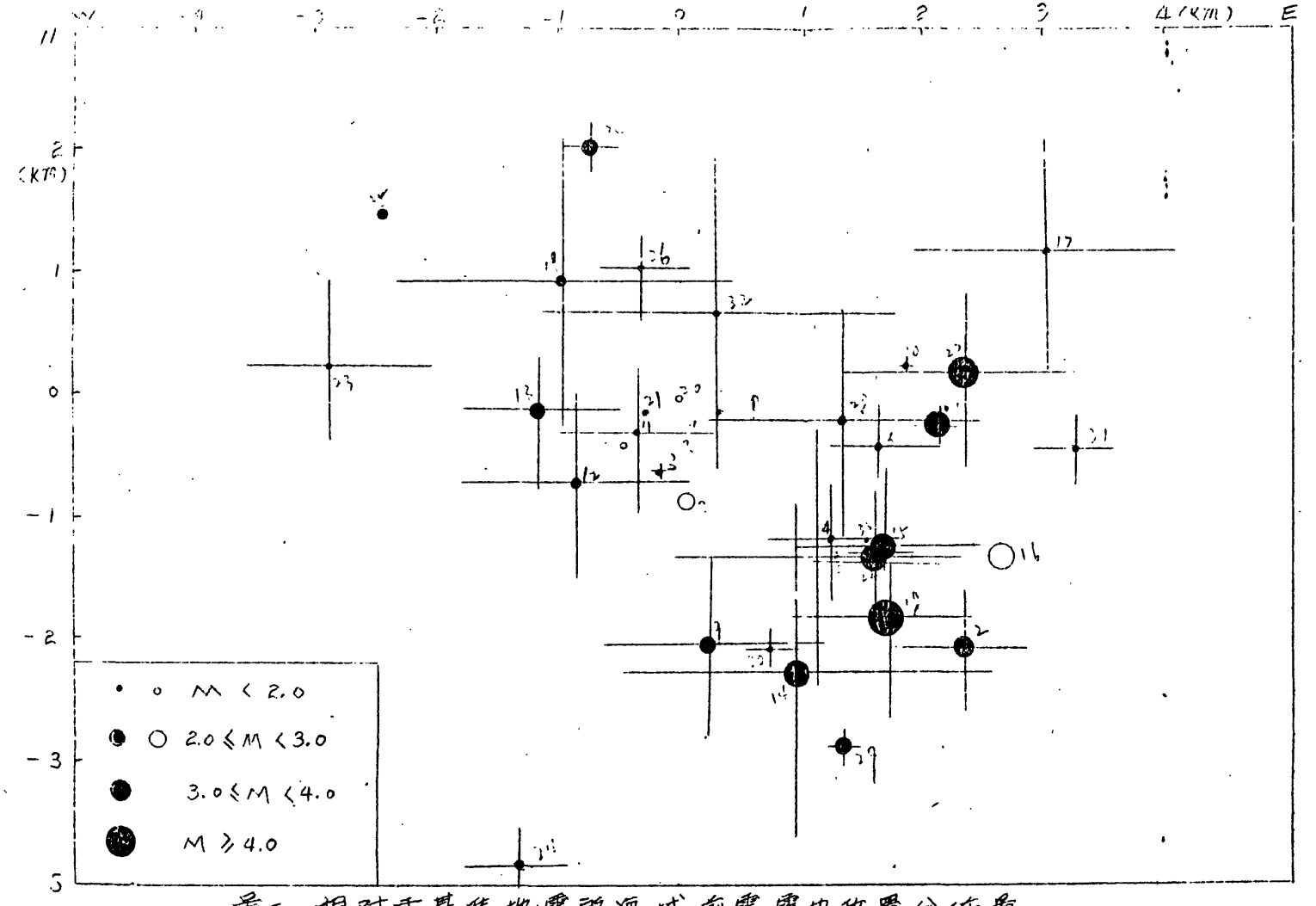

图二、相对于基准地震的海城前震震中位置分布图。十字线表示定位的林准偏差，空心圆表示林准偏差大于2 KM的前震

表 I 1 9　　1975年2月4日海城地震前震位置

编号	日期	发震时刻	震中位置 相对位置(KM) E－W	震中位置 相对位置(KM) N－S	震中位置 E°	震中位置 N°	震源深度(Km)	定位误差 E—W	定位误差 N—S	定位误差 深度	震**级	备注
1	3	19-13-39·5	0	0	122° 49′ 27″	40° 40′ 46″	14·9					
2		21-22-57·2	2·32	-2·04	51′ 07″	39′ 40″	11·5	·64	·55	2·0	3·1	
3		23-50-14·1	-·19	-·60	49′ 19″	40′ 27″	14·8	·05	·05	·2	1·6	
4		23-55-11·0	1·24	-1·18	50′ 20″	40′ 08″	12·9	·61	·52	1·91	1·5	
5		23-56-00·7	1·12	-1·28	50′ 15″	40′ 05″	14·1	31·2	1·1	3·5	1·5	
6	4	00-02-08·3	1·65	-·39	50′ 38″	40′ 33″	13·3	·5	·4	1·5	1·5	
7		00-58-50·2	2·11	-·12	50′ 58″	40′ 42″	12·8	·3	·2	·6	3·0	
8		02-18-16·0	·29	-·21	49′ 39″	40′ 39″	15·7	2·0	1·7	6·2	1·6	
9		03-22-14·6	·22	-2·03	49′ 36″	39′ 40″	14·8	1·0	·8	3·0	2·4	
10		03-54-43·1	1·86	·23	50′ 47″	40′ 53″	12·9	·05	·05	·1		
11		04-17-51·8	-·44	-·37	49′ 08″	40′ 34″	16·6	2·1	1·8	6·5	1·7	
12		05-33-19·5	-·84	-·71	48′ 51″	40′ 23″	15·1	1·0	·8	2·9		
13		06-11-47·2	-1·18	-·11	48′ 36″	40′ 42″	16·6	·6	·5	1·9	2·8	
14		06-13-05·7	·93	-2·32	50′ 07″	39′ 31″	12·5	1·6	1·4	4·9	3·1	
15		06-53-20·8	1·67	-1·26	50′ 39″	40′ 05″	12·3	·8	·7	2·4	3·3	
16		06-58-21·0	2·63	-1·34	51′ 20″	40′ 03″	12·8	2·0	1·7	5·8	3·7	
17		07-14-33·8	3·00	1·19	51′ 36″	41′ 25″	12·4	1·1	·9	3·3	1·2*	
18		07-50-48·2	1·68	-1·69	50′ 39″	39′ 51″	13·2	·8	·7	2·5	4·7	
19		08-11-12·4	-·98	·95	48′ 45″	41′ 17″	15·3	1·4	1·2	4·4	1·3*	
20		08-13-04·8	·05	-·85	49′ 29″	40′ 18″	16·4	2·8	2·4	6·7	2·3	
21		08-14-45·4	-·35	-·29	49′ 12″	40′ 37″	15·6	·7	·6	2·0	1·5*	
22		08-57-14·7	1, 57	-1·34	50′ 34″	40′ 03″	13·3	·7	·6	2·1	3·3	

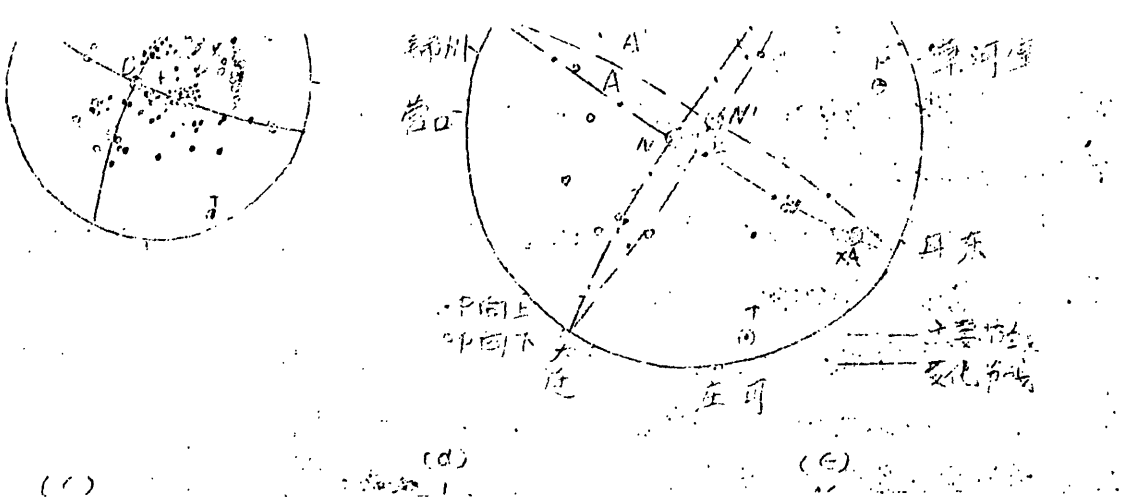

23	4	09-17-54·1	-2·88	·24	47′ 23″	40′ 54″	18·7	·8	·7	2·6	1·3*	
24		09-36-42·6	-1·38	-3·82	48′ 28″	38′ 42″	15·5	·4	·4	1·3		
25		10-28-32·2	-2·46	1·48	47′ 41″	41′ 34″	17·9	·01	·01	·04	2·6	
26		10-33-29·7	-·33	1·06	49′ 13″	41′ 20″	14·6	·4	·3	1·2	1·8	
27		10-35-28·9	2·34	·19	51′ 07″	40′ 52″	11·8	1·0	·7	2·5	4·3	
28		10-47-19·1	1·34	-·20	50′ 25″	40′ 40″	12·7	1·2	1·0	3·4	2·0	
29		11-25-17·9	1·35	-2·85	50′ 25″	39′ 14″	13·0	·2	·2	·7	2·3	
30		13-08-06·5	·75	-2·05	49′ 58″	39′ 40″	13·5	·3	·2	·8	1·6	
31		13-53-58·7	3·24	-·42	51′ 46″	40′ 32″	11·5	·5	·4	1·4	0·9*	
32		14-56-24·4	·28	·69	49′ 39″	41′ 08″	13·8	1·5	1·3	4·7	1·1*	
33		16-23-13·7	1·64	-1·28	50′ 37″	40′ 05″	12·5	·4	·3	1·1	0·8*	
34		16-24-39·5	-·73	2·05	48′ 56″	41′ 52″	16·3	·3	·2	·9	2·6	

102

**震级数据取自辽宁地震队所定震级（除*者外）

*带 号地震的震级取自营口台所定震级

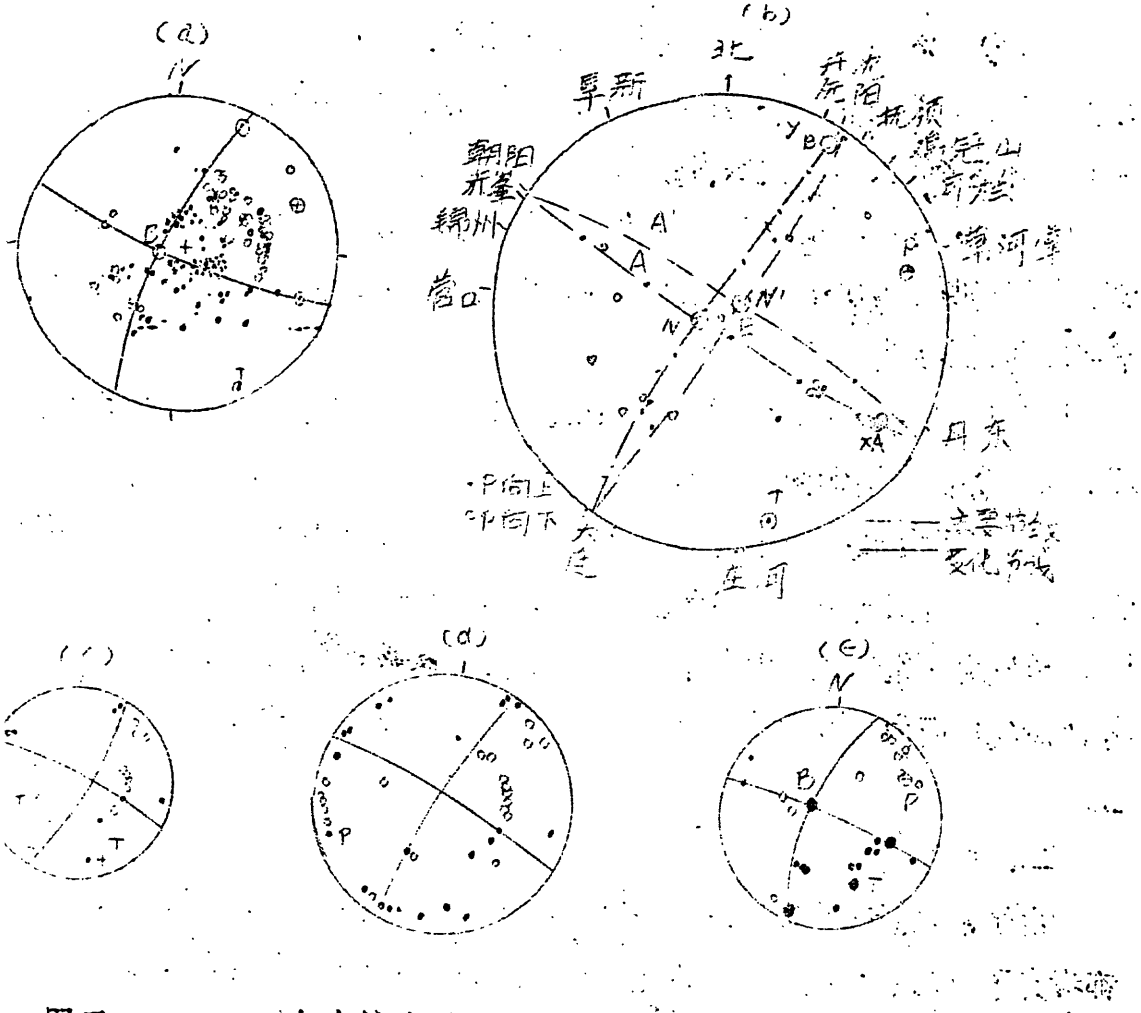

图三、1975年海城主震（a）和前震（b、c、d、e）断层面解（其中a、e根据〔5〕，b根据〔1〕，cd根据〔4〕）

活动，将产生相似的断层面解。在海城地区存在着NWW和NNE两个走向的断层构造。还有，余震区呈NWW走向，但略有从主震震中向NNE方向扩展的余震活动。因此，似乎可能：沿主震平面发生了一些前震（B组），而多数以及较大的前震也许是沿着大约垂直于主震的面发生的。

为了进一步考虑这个问题，我们将前震分别投影在N73°W及N28°E方向的垂直（于地表）平面中，作前震随深度的分布图（图四），以研究"前震面"和"主震面"。这些图的最明显的特性是有一个明显的倾向

于NWW方向的NNE百，且表明B组地震是发生在较深下位。然而我们不能很好地控制深度，一般来说，深度误差是震中位置误差的三倍（见表一）因此这个结果并非是很可信的。

图四a，投影在N73° W方向上垂直（于地表的）平百中的海城前震深度分布图。实心园表示位于A组的地震，空心园表示位于B组的地震。十字表示震中误差大于2 KM的地震。

图四b，投影在N28° E方向上垂直（于地表的）平百中的海城前震深度分布图。图例同（a）。

另外，由于仅有一个近台为营口台（Δ=20 KM），它位于前震的近正方向，所以这个明显的西倾下分层因可能是由此引起的。然而一般来说，前震的A组看来好象位于沿北北东方向的近于垂直地表的平百内的很小的深度范围内，B组地震较分散，可能与A组不同，位于主震百的方向上。

二、振幅比

由于常常假设前震系列的全下前震有同样的震源机制，很多研究工作都考文了系列中p波S波振幅比是否变化的问题，但结果不尽相同〔2〕〔4〕〔6〕〔7〕〔8〕〔9〕。此外有较多台记录到海城地震大易前震系列，这提供了研究此问题的良好机会。主震前24小时内，在前述6个台上所记到的前震，其p波S波振幅示于图五和图六中。每个台所记振幅比的平均值及标准偏差列入表二中。

除最近的营口台外，其他各台所记的前震，波形较相似，且直至最大前震（2月4日）07^h50^m $M_S=4.7$）发生前，振幅比变化不大。在最大前震发生后，波形有所不同（例如，可看图7a锦州台所记两个地震，及图7b抚顺台所记另两个地震），且振幅比较最大前震前略分散（图六），但是在震群中最大地震发生前和发生后的振幅比也有类似的结果。例如山东牡机震群近台记录作出的振幅比的标准偏差就比营口台所记海城前震的

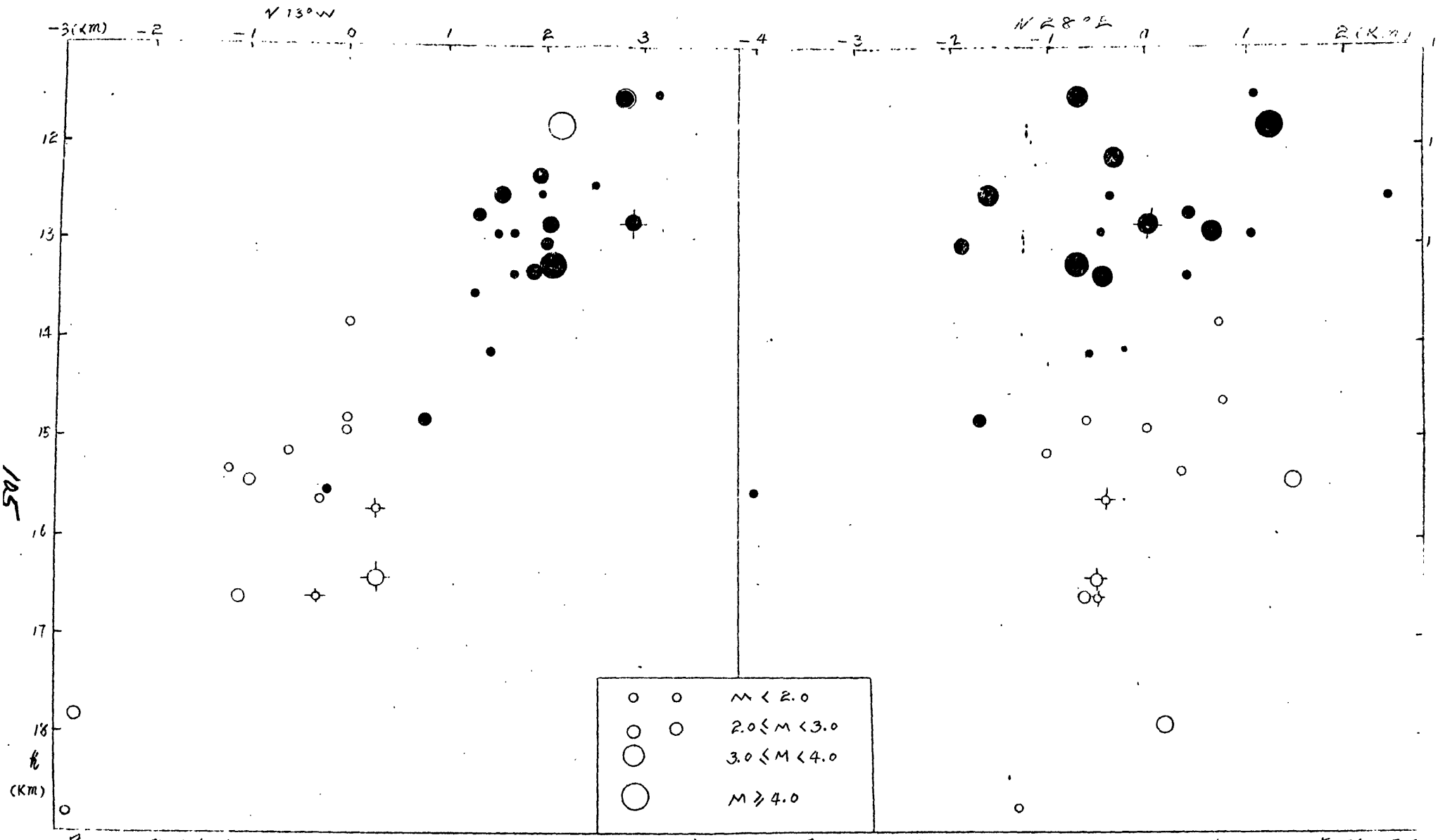

图四(a) 投影在N13°W方向上垂直(于地表的)平面中的海域前震深度分布图。实心圆表示位于A组。空心圆表示位于B组的地震。十字表示震中误差大于2Km的地震.

图四(b) 投影在N28°E方向上垂直(于地表的)平面中的海域前震深度分布图。图例同(a).

125

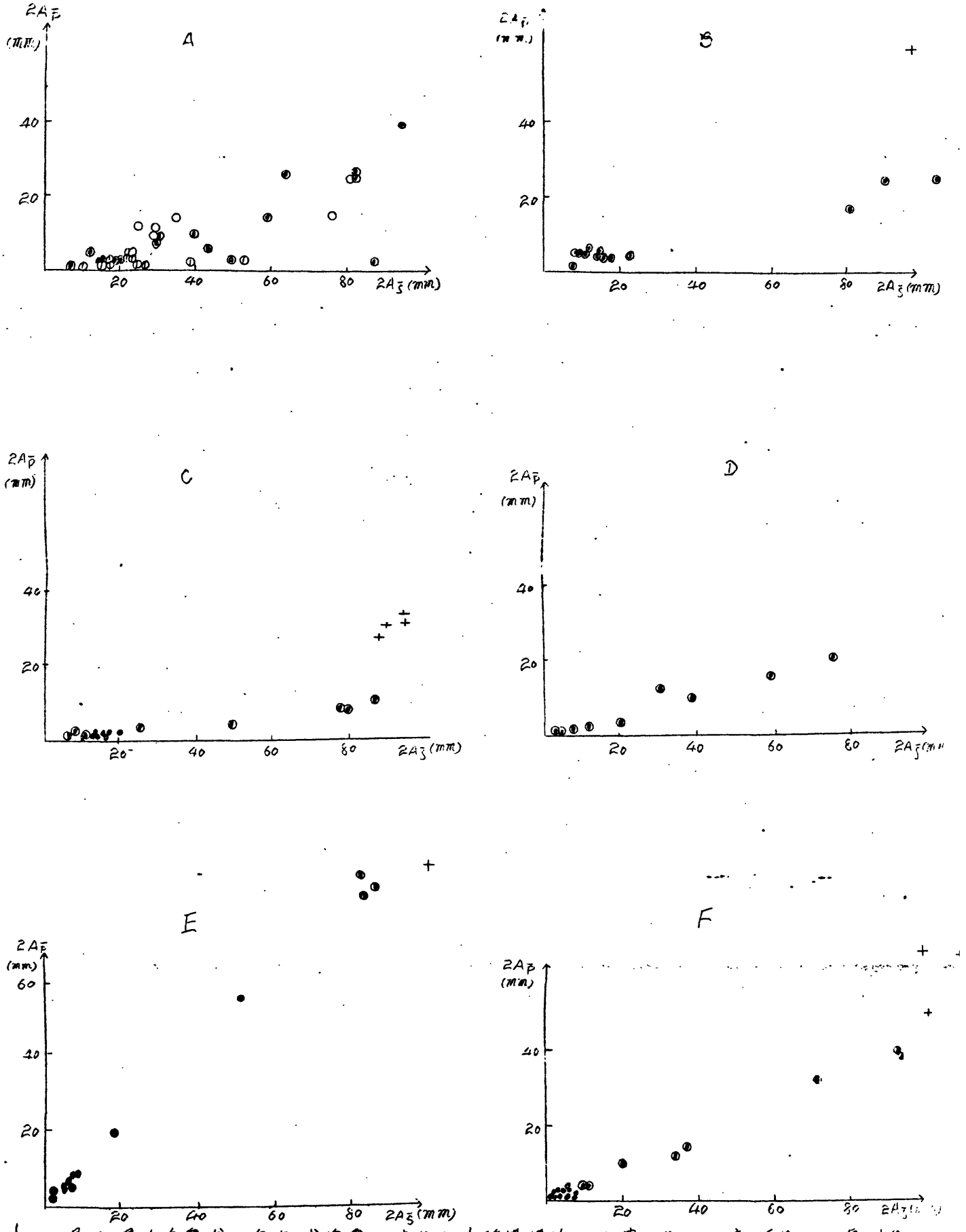

图五、最大前震发生前海城前震P波与S波的振幅比。(a)营口台、(b)庄河台、(c)锦州台
(d)抚大台、(e)鸡河台、(f)抚顺台 ⊙表营口台小P波形、○表营口台大P波形 +空表示P振幅

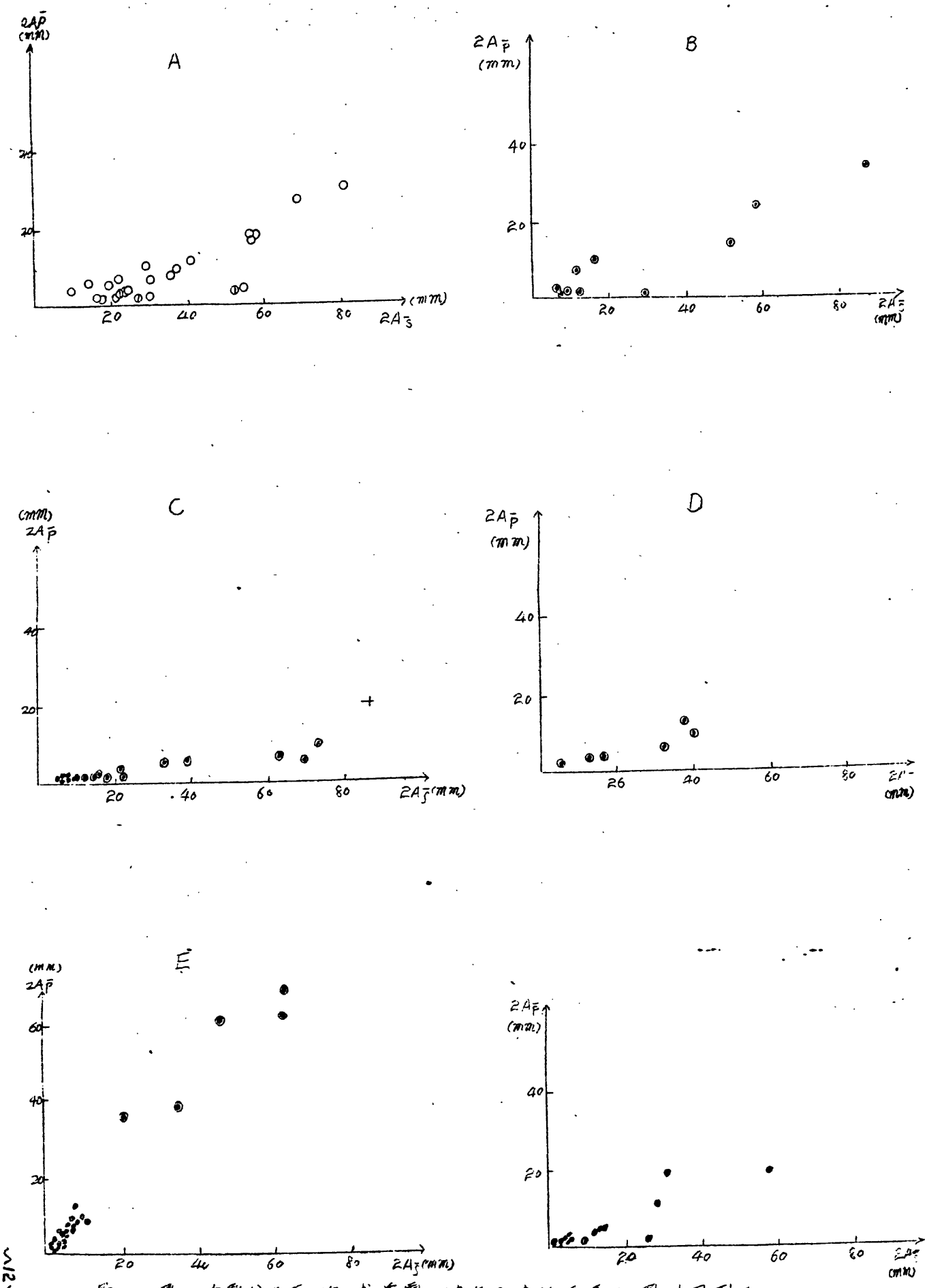

图六. 最大前震发生后，海城前震P波与S波的振幅比. 图例同图五.

表二、测易振幅比均值、方差表

		营口		抚顺	庄河	旅大	草河掌	锦州
		大P波形	小P波形					
75·2·4 07-50 地震前	均值 $\bar{x}$	0·30	0·08	0·36	0·28	0·20	1·01	0·11
	方差 6_x	0·10	0·04	0·12	0·14	0·10	0·17	0·07
75·2·4 07-50 地震后	均值 $\bar{x}$	0·35	0·06	0·35	0·31	0·26	1·03	0·12
	方差 6_x	0·04	0·03	0·14	0·19	0·07	0·28	0·10

振幅比的标准偏差小〔表三〕〔10〕。由此，振幅比的积定显可能是前震的一个特性，但似乎并不是区分一个系列是震群还是前震系列的可信标志特别是营口台的记录所作出的振幅比甚至明显地不同于由其他远台记录所作出的振幅比。在个前震系列，营口台都记到两种肯定不同的波形，一种有相对大的p波，另一种有较小的p波（图八）。直到最大前震发生以后，这两种中每一种的振幅比都相对不变。试图将营口台的两种波形与其他台对比，但有困难。因为，一般来说，如果一个地震相当大能在远台上记到，则在营口台上将记得很大并限幅。可识别为大p波形和小p波形的地震有六个可以定位（见表一），但在其他台上却仅有两个或三个地震可作出振幅比，所以不能比较。

表三、近台前震及震群测易振幅比的均值、方差表

		海城地震（营口台）	砣矶震群
最大地震（或前震）之前	均值 $\bar{x}$	0·22	0·26
	方差 6_x	0·17	0·11
最大地震（或前震）之后	均值 $\bar{x}$	0·21	0·23
	方差 6_x	0·12	0·12

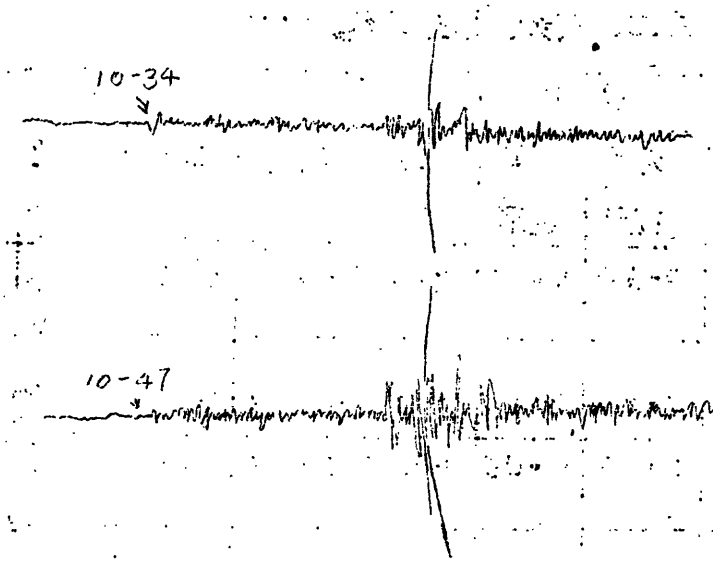

图七(a) 锦州台记录的两个海城前震(4日10h34m;
4日10h47m).

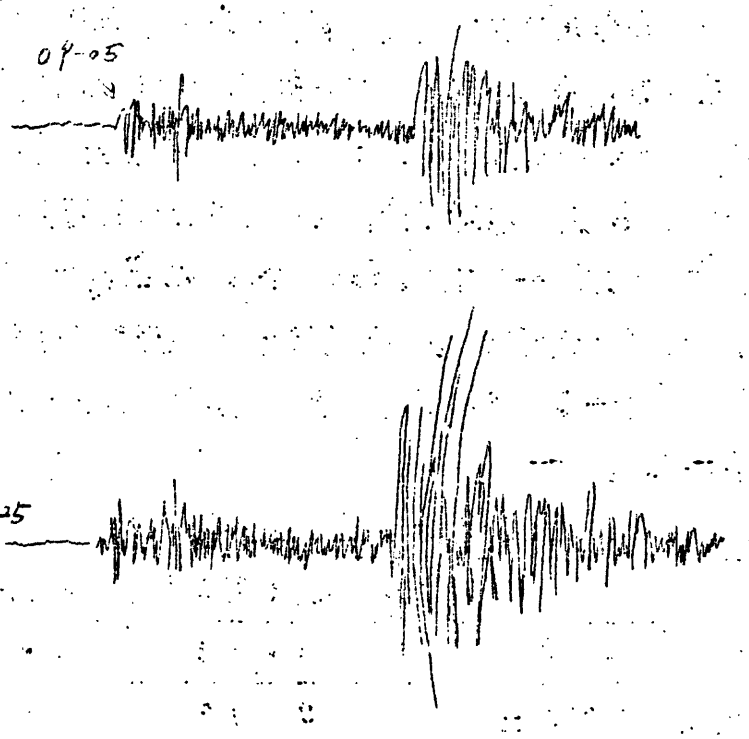

图七(b) 抚顺台记录的两个海城前震(4日09h05m;
4日16h25m).

表四、计标振幅比

NO	地　震	各台振幅比（A_p/A_s）						备　注
		营口	抚顺	庄河	旅大	草河掌	锦州	
1	75·2·4·19^{h}36^m 主　震	0·11	0·53	2·47	0·36	0·76	0·03	取〔5〕中主震断层面解，本文所定前震中心位置计标的
2	75·2·4·07^{h}50^m 前　震	0·47	0·24	0·92	0·38	0·75	1·14	取〔1〕中前震断层面解，本文所定前震中心位置计标的
3	75·2·4·17^{h}50^m 前　震	0·17	0·50	0·35	0·22	1·22	0·19	取〔5〕中最大前震断层面解，本文所定该震震源位置
4		0·15	0·53	0·38	0·22	1·48	0·07	震源位置相对于N03中的位置西移3KM，北移2KM，深2KM，其它同N03。

有几个迹象支持这个假设。如前所述在最大前震发生后，较远的各台振幅比较为分散，这可能由于最大前震后有较多的地震位于B组；同样，在测定断层百解中，在决定NNE的特确位置上，在西南方向的旅大台是具有控制作用的。我们考文旅大台几个较大前震的初动得到，在大多数情况下是膨胀波（断层百解的NNE百则应比较直立或倾向于北西方向），而对主震和B组前震（表一中N034），它是压缩波（断层百解则为南西倾向）；支持本假设的另一迹象是，在营口台所记大p波形地震的S与p到时差为2·5或2·6秒，它正好是A组南端S与p的到时差。另一方百，小p波形地震的S与p到时差比较分散，为2·2秒至2·8秒之间。

若不考虑上述资料，则得不到两种机制和两组位置之间的直接关系。

能定位的有确定波形的地震有六个，其中两个大p波形地震及两个小p波形地震A组，一个大p波形地震及一个小p波形地震在B组，故不同波形和两组地震并不是直接相关的。可能平百的内锁允许产生互相很接近的不同的断层机制，但也可能资料的误差产生了这种错觉。

五、结　论

本文研究了海城前震的定位和机制。所有前震均发生在互相不超过6公里的范围内。虽然不是肯定的结论，但很可能前震活动有两组，且多数前震不发生在主震的破裂百中，而是在近于垂直于主震百的另一平百上。有时近台所记震群的p波和S波振幅比也比较秋定，且标准偏差比营口台前震的p波S波振幅比的标准偏差还小。在最大前震发生前和发生后，在最近的台上记到了两种相当不同的波形。因此p波与S波振幅比似乎并不是判定前震的一个特确方法。在两种机制及两组震中位置之间似可得出一定的关系。

参考文献

(1)、吴开统、岳明生、武宜英"海城地震序列的特征"地球物理学报第十九卷 第二期，1976年。

(2)、Jones, Lucile M, and Peter Molnar。"Some Characteristics of Foreshocks and Their Possible Relation to Earthquake Prediction and Premonitory Slip on Faults"

J.G.R.1979。在印刷中

(3)、许绍燮、王碧泉、章光月（Lucile Jones）、马秀芳、沈佩文等"海城前震系列与震群"地球物理学报、在印刷中。

(4)、金严、赵毅、陈颙等"辽宁省海城地震前震震源错动方式的一个特点"地球物理学报 第十九卷 第三期 1976年。

(5)、顾浩鼎、陈运太等"1975年2月4日辽宁省海城地震的震源机制"地球物理学报 第十九卷 第四期 1976年

(3)、陈颙 "用震源机制一致性作为描述地震活动性的新参数"地球物理学报 第二十一卷 第二期 1978年

(7)、Bolt, B.A. etal B.S.S.A. Vol 67。

PP1555-1564。1977。

(8) Engdahl etal。J。Phy。earth 25。S243-S250。

1977。

(9) Lindh。A etal。Science 1978。

(10) 魏光兴、李秉锋、"1976年春山东庙岛群岛两次小震群"

(11)、Ben-Menahem etal。B.S.S.A. Vol55。

PP203-235 1965。

SEISMOTECTONIC ASPECTS OF THE MARKANSU VALLEY, TADJIKSTAN, EARTHQUAKE OF AUGUST 11, 1974

James Jackson
Department of Geodesy and Geophysics
Madingley Rise, Madingley Road
Cambridge CB3 OEZ, ENGLAND

Peter Molnar
Department of Earth and Planetary Sciences
Massachusetts Institute of Technology
Cambridge, MA 02139

Howard Patton
Lawrence Livermore Laboratory
P.O. Box 808
Livermore, CA 94550

Thomas Fitch
Applied Seismology Group
Lincoln Laboratory
Massachusetts Institute of Technology
42 Carleton Street
Cambridge, MA 02142

ABSTRACT

The Markansu Valley Earthquake of 11 August 1974 (m_b = 6.4) occurred in a structurally complex area of the northern Pamir. It was followed by more than 80 teleseismically recorded aftershocks, thirteen with $m_b \gtrsim 5.0$. Fault plane solutions for the three largest aftershocks differ from one another and from the mainshock and indicate both thrust and strike-slip faulting. Geological mapping and aftershock locations suggest that the strike-slip faulting occurred on both north and northwest trends. The region is one in which large northwest trending strike-slip faults converge. To the north and south these faults are very clear topographic features. As they approach the northeastern Pamir they become less distinct on the Landsat imagery, although they remain recognizable geologic features on the ground. The strike-slip faults may become less distinct towards their ends because the north-south motion is taken up progressively by east-west striking thrusts. It is not possible to fit orthogonal nodal planes to all of the observed first motions of the P waves from the mainshock. This earthquake is located at the intersection of two inferred fault systems and appears to be a multiple rupture. The discrepant P wave first motions are all nodal in character. If faulting occurred on more than one fault plane during the mainshock, then the apparent first motions in the nodal

directions of the first rupture may be anomalous and actually belong to a rupture later than the first one. We are aware of one other similar occurrence: the 1967 Mudurnu, Turkey earthquake, for which the few anomalous P wave first motions were also nodal and for which the fault plane solutions of the mainshock and the largest aftershock are very different. The concentration of large earthquakes near the intersection of two systems is also observed in Iran.

INTRODUCTION

Recent studies of continental deformation in the Alpine-Himalayan belt show that large scale horizontal motions often take place on narrow strike-slip systems of considerable length such as the North Anatolian fault and Altyn Tagh fault, which may bound relatively aseismic blocks [e.g. McKenzie, 1972, Molnar and Tapponnier, 1975, 1978, Tapponnier and Molnar, 1977, 1979]. These large strike-slip faults may curve in places along their length and sometimes motion changes from pure strike-slip to include a compressional or extensional component. Where deformation occurs primarily by strike-slip faulting it is often confined to narrow zones. However, where crustal extension or compression takes place, such as in western Turkey, northwest Iran, the Pamir and Yunnan, deformation appears to be spread out over large areas and motion is not confined to a single narrow fault system. Of particular interest is how one style of continental deformation changes into the other. Complexities are seen where well defined strike-slip systems meet or pass into compressional or extensional systems, such as in Yunnan and Szechwan of China [Tapponnier and Molnar, 1977] and at the eastern end of the North Anatolian Fault in Iran and Turkey [McKenzie, 1972]. This paper discusses the deformation associated with an earthquake sequence in a structurally complex region in the northern Pamir. This area is one of active thrusting towards which the large Altyn Tagh, Karakorum and Talasso-Fergana strike-slip fault systems converge (Figure 1.)

REGIONAL STRUCTURE

Burtman et al. [1963] and Ruzhentsev [1963] discuss in some detail the geology and structure of the southern Tien Shan and eastern Pamir. The main structural features are the large northwest trending right lateral strike-slip faults which cross the region (Figure 2). To the northwest the "Tien Shan - Kun Lun Fault" (TS-KL) of Burtman et al. [1963] includes the Talasso-Fergana Fault [Burtman, 1963], which is particularly active further north and stands out well on the Landsat Imagery [Tapponnier and Molnar, 1979]. As it enters the area of Figure 2. it becomes less distinct on the Landsat imagery and may not be active south of about 41°N. It is possible that its motion is then taken up by other northwest trending strike-slip faults further south. The Karakorum Fault (Figure 1), a right-lateral strike-slip fault [Peive et al., 1964] and a remarkably clear feature on the Landsat imagery [Molnar and Tapponnier, 1978] and topographic maps, lies to the southeast of the region in Figure 2. It seems to continue into the southeast corner of Figure 2 as a group of subparallel faults including the "Pamir-Karakorum Fault" (P-KK) and "Kungur Fault" (KF) of Burtman et al. [1963]. On the Landsat imagery, none of these are as obviously active as the Karakorum Fault itself further south. Since the installation of the World Wide Standard Seismograph Network (WWSSN) there have been no earthquakes on either the southern part of the Talasso-Fergana Fault or the northern part of the Karakorum Fault large enough for a fault plane solution to be determined, although the seismicity of the region is high.

To the west of the Pamir-Karakorum Fault in Figure 2 a number of east-west thrusts dominate the structure of the Pamir. Most of them dip to the south [Burtman et al., 1963, Ruzhentsev, 1963]. In addition a series of right-lateral strike-slip faults branches off to the west of the Pamir-Karakorum Fault at angles of 20-40° (Figure 2). The relationship between the strike-slip and thrust faults of the central Pamir was clarified in a detailed investigation in the Murgab region (about 38.5°N, 74°E) by Ruzhentsev [1963]. He noticed that towards the northwest the strikes of the northwest trending strike-slip faults became more westerly and that motion changed into thrusting. This change was accompanied by a decrease in displacement on the strike-slip faults. Burtman et al. [1963] describe a decrease in displacement towards the southeast along the Tien Shan - Kun Lun Fault and towards the northwest along the Pamir-Karakorum Fault. It seems that as the strike-slip systems approach the southern Tien Shan and Pamir from the northwest and southeast, displacement along them is taken up by a number of thrusts over a wide area. Correspondingly, displacement on these strike-slip faults decreases although they remain clear as geological features. This may explain why they are so indistinct on the Landsat imagery of this region (Figure 3), whereas to the northwest and southeast they are very clear [Molnar and Tapponnier, 1978, Tapponnier and Molnar, 1979].

Two prominent faults are observed in Figure 3. A major break of slope in the alluvial fan at 39.22°N, 74.5°E may be a

thrust dipping northwards on the curved continuation of the Kungur Fault (Figure 2). About 5 km further north is another fault (Figures 2 and 3), also marked on the map of Burtman et al. [1963]. Near 38.7°N, 74.2°E the Karakul Thrust is visible and dips northwards [Burtman et al., 1963]. Further south short segments of more northerly lineated drainage may perhaps indicate the smaller strike-slip faults referred to by Ruzhentsev [1963].

AFTERSHOCK LOCATIONS

The Markansu Valley earthquake of August 11, 1974 (m_b=6.4, M_s=7.3) was located at 39.34°N, 73.76°E by the International Seismological Centre (ISC). It was followed by more than 80 teleseismically recorded aftershocks, for thirteen of which $m_b \geq 5.0$. The mainshock and three of the aftershocks were large enough for fault plane solutions to be determined from first motions of P waves recorded by the long period WWSSN instruments. These solutions differ from one another and show both strike-slip and thrust faulting (see below).

The mainshock and its aftershocks were relocated using a technique, described in detail by Jackson and Fitch (1979), which locates earthquakes relative to a master event. Relative locations are not affected by a major source of error in absolute locations that arises from azimuthal travel time anomalies caused by upper mantle heterogeneities. This region is known to be heterogeneou and ray paths are very likely to be perturbed by the deep structure of the nearby Hindu Kush [Khalturin et al., 1977] as well as by

other deep structure in the Himalayan belt. The method used pays careful attention to the assumption behind all relative locations: that ray paths between source and receiver are essentially the same for different events. The source area of the 1974 aftershocks is small (Figure 4) and no earthquake further than 70 km from the master event was relocated. The technique is very effective in places where teleseismic travel time anomalies are high, as shown by Fitch and Jackson [1979] in the Tonga arc.

The pattern of relative locations can be positioned in space only when some a priori location for one of the events is known. The Markansu Valley earthquake occurred in a very mountainous and sparsely populated region, and we are not aware of any detailed reports of epicentral damage, surface faulting or isoseismal mapping that might constrain the location. The mainshock of August 11 was a complicated rupture producing complex seismograms (see Figure 6 and Zakharova and Chepkunas [1977]). The event of 27 August 1974 was chosen as a master because impulsive P wave onsets from it were reported at many stations. Relocations are shown in Figures 4 and 5 and listed in Table 1. We have no a priori information for the location of any of the shocks, so the locations are drawn in Figure 2 assuming the ISC location of 39.52°N, 73.82°E for the master.

All the earthquakes appear to be shallow but depths are not well constrained. The ISC reports a depth of 19 km for the master and no large event was relocated more than 20 km below it.

Surface wave analysis shows that depths for three shocks in this area are less than about 15 km [Patton, 1978]. No pP phases were unambiguously reported and we are not aware of evidence for subcrustal seismicity in the Markansu Valley region.

FAULT PLANE SOLUTION OF THE MAINSHOCK

We were unable to fit two orthogonal nodal planes to the P-wave first motions of the mainshock. As the radiation patterns of the three main aftershocks and of the event of 11 May 1969, which occurred near the mainshock, all differ from one another and from that of the mainshock (Figure 6 and 7 and Table 2), it is tempting to conclude that slip occurred on more than one plane during the mainshock. Before discussing this possibility, let us first discuss in more detail the radiation pattern of the mainshock.

Figure 6 shows the lower hemisphere equal area projection of the radiation pattern and some key seismograms. Three possible solutions are also shown - one with essentially pure strike-slip motion as for the event of 11 May 1969 (Figure 7), a second with essentially pure thrust faulting as for the first large aftershock (Figure 7), and a third given by Ni [1978] for the mainshock, showing oblique thrusting. This latter solution is crudely what one would expect if two earthquakes with the other two solutions occurred simultaneously. Notice that all three solutions shown in Figure 6 violate some of the first motions. Because the dilatations recorded at stations to

the south (in India and Pakistan) are clear, the pure thrust solution can be rejected. The main difference between the pure strike slip solution and Ni's oblique slip is from stations to the north (in northern Europe, Greenland and Alaska). The first half cycle is clearly weak for all of them, but at STU, VAL, KON, GDH and COL, it is clearly compressional (Figure 6). At the closer stations, NUR, KEV and KBS, we have interpreted the first motions as very weak dilatations. In any case the next two half cycles are both very small, suggesting radiation near a nodal plane. In all cases, our choices of the first motions were made from the long period records, as shown in Figure 6. The arrival times of the P waves on the short period records, however, agreed with the arrival times of the P waves that we picked on the long-period records. If the later, larger signals were chosen for the first motions, they would have arrival times later than the first arrivals on the short period records. We also disagree with Ni [1978] on the first motions at QUE and LEM. We think that we can see a very small dilatation preceding the large compression of QUE. We think that the first motion at LEM is dilatational, but we can see where one might pick the half cycle before it as a compression. Our choice of a dilatation is based in part on the arrival time of the P wave determined from the short period record, but this short period record is not particularly clear. Even if Ni's interpretation for the recordings were correct, a similar strike-slip solution could be found

consistent with compressions at these two stations.

We favor the strike-slip solution principally because of the first motions of S waves. There are many fewer first motions for S waves than P waves, because we could not reliably pick them at most stations. Those that we did determine, however, agree with the strike-slip solution, and those at COL and PMG, in particular, are inconsistent with Ni's oblique slip solution.

As a further check, we analyzed the surface waves at several stations. The results are reported in Appendix A. They do not favor any of these three fault plane solutions.

DISCUSSION OF THE MAINSHOCK

The Markansu Valley earthquake was unusual in that it was impossible to fit two orthogonal nodal planes to the P wave first motions. The July 22, 1967 Mudurnu earthquake in western Turkey is another example [McKenzie, 1972, Figure 26ℓ]. In common with the Markansu Valley shock, it was followed by large aftershocks with different fault plane solutions from the mainshock. At Mudurnu the change in mechanism was from strike-slip to normal faulting [McKenzie, 1972]. Thus in both these sequences more than one fault plane was active. The Markansu Valley shock appears to be a multiple rupture, as can be seen on the seismograms in Figure 6 [see also Zakharova and Chepkunas, 1977]. While this is not uncommon for large crustal earthquakes, ruptures are usually assumed to have occurred on the same fault plane, with substantially the

same mechanism as the initial event [e.g. Wyss and Brune, 1967, Fukao, 1972]. For the Markansu Valley event it is possible that the first rupture was closely followed by a second that ruptured a fault with a different trend. This is especially plausible as the mainshock occurred very close to the intersection of two belts of aftershocks, each of which is parallel to one nodal plane of one of the larger events in the sequence (Figure 4). If the two ruptures nucleated very close together in space and time, then P waves radiated to stations close to a node in the radiation pattern of the first might be lost in the noise, and the larger onset of the second event would be picked as the first motion. The discrepant observations radiated to the north (Figure 6) are close to nodal planes of each of the three possible solutions shown. This may account for the curious character of the records at NUR, KEV and KBS which seem to have "double nodal" onsets. It is significant that at Mudrnu the discrepant readings are also nodal [see McKenzie, 1972, Figure 26ℓ]. The explanation offered above would be unlikely to apply to discrepant observations far from the nodal planes of the first rupture because the second rupture would presumably be triggered by the arrival of energy from the first and the signal from the first rupture would clearly be recorded before the second. Only near a nodal plane is the arrival from the first rupture likely to be too small to be seen.

From Figure 6 it might appear possible that the closer stations such as NUR, KEV, KBS recorded the first motion of the initial rupture. Then, at the more distant GDH and COL the weak nodal signal of the first rupture may have been lost in noise and instead only a later rupture with a different mechanism was recorded. If this were so and the two ruptures were sufficiently separated in time, the distant stations should show a positive (late) travel time residual relative to the closer stations. Figure 8 shows the travel time residuals from the ISC location for the mainshock for northern stations in the azimuth range 320°-20°. Unfortunately, the data scatter, and no particular trend is observed. Both the Markansu Valley and Mudurnu earthquakes are too small for the second and subsequent ruptures to be relocated relative to the first, as done by Wyss and Brune [1967] and Fukao [1972].

An alternative explanation for the discrepant observations is that laterally heterogeneous velocity structures have refracted teleseismic ray paths and therefore that the stations are not plotted in Figure 6 in their correct positions on the focal sphere. This effect was inferred for earthquakes at ocean ridges [Solomon and Julian, 1974; Thatcher and Brune, 1971], and the upper mantle structure under the Pamir and western Tien Shan is thought to be anomalous [e.g. Khalturin et al., 1977].

FAULTING IN THE SOURCE REGION

The fault plane solutions from five earthquakes in the source region show three types of faulting. The preferred solution for the mainshock and that for 11.5.67 show strike-slip faulting on northwest-southeast or northeast-southwest planes. The trend of aftershocks (Figure 4) implies a northwest-southeast fault plane, therefore with right lateral motion parallel to the Pamir-Karakorum Fault [Burtman et al., 1963]. If the ISC location for the master event (27.8.74), by which the pattern in Figures 2 and 4 is positioned, were in error by 25 km, the northwest trend of aftershocks could lie on the extension of this fault. A systematic error of 25 km in the ISC location is possible.

The two largest aftershocks (8.11.74b and 8.11.74c) show thrust faulting, but in both the strike-slip component is not well resolved. The shallow dipping planes of Figures 4 and 7 are essentially those given by Patton [1978]. He inverted Rayleigh wave spectra to obtain moment tensors for these events, and the corresponding fault plane solutions agree remarkably well with the P wave first motions. It is possible, however, that a small component of strike-slip motion is also present. Ni [1978] shows fault plane solutions for these aftershocks, of which 11.8.74b is in general agreement with ours. We disagree about 11.8.74c, which he regards as a normal fault. This is principally because he read the onsets at some southeastern stations (e.g. BAG and LEM) as

dilatational, and to us they appear to be compressional. Three other thrust solutions of earthquakes from this general area are also known (Figure 4). The three westernmost solutions of Figure 4 all show a shallow southward dipping nodal plane consistent with southward underthrusting at the northern margin of the Pamir (Figure 2).

The fault plane solution for the master event (26.8.74) shows predominantly strike-slip faulting on either north-south or east-west planes, and is clearly different from those of the mainshock (11.8.74a) and 11.5.67. A northerly trend of aftershocks (Figure 4) suggests a north-south fault plane, therefore with left lateral motion.

The two thrusting aftershocks are on an extension of the northwest-southeast strike slip trend, a phenomenon observed for many continental earthquakes, e.g. Dasht-e-Bayaz, Iran [Jackson and Fitch, 1979]. Such intersections of fault trends appear to be areas of intense aftershock activity and stress concentration (Figure 5).

Figure 5 shows that the smaller aftershocks do not closely follow the trends delineated by the larger shocks. This is not necessarily because they are mislocated but is a general phenomenon where faulting is not confined to a single strike-slip system. Jackson and Fitch [1978] mention this effect at Gediz, Turkey and it has also been observed by local networks [e.g. Whitcomb et al., 1973]. The smaller aftershocks may represent internal deformation in blocks whose overall motion is controlled by larger faults.

CONCLUSIONS

The region affected by the August 11, 1974 event and its aftershocks is small. Thirteen shocks with $m_b \geq 5.0$ were concentrated in an area about 30 km wide. The inferred faulting during the 1974 Markansu Valley Sequence is similar to that described by Burtman et al. [1963] and Ruzhentsev [1963] for the northeast Pamir. In particular, right lateral strike-slip faulting on northwest striking planes is intimately associated with thrusting on east-west planes. Although we are not aware of persuasive evidence for north-south faulting, as is inferred for one trend of aftershocks, Ni [1978] interprets a north-northeast structure through the center of the lake Karakul (LK in Figure 2) as an active fault (Figure 3).

In contrast to most regions thrust faulting is more clearly seen on the Landsat imagery than the strike-slip faults. An explanation of this effect may be that at the ends of the strike-slip faults displacement decreases and is taken up on not one but several thrusts [Ruzhentsev, 1963]. This may cause the strike-slip fault to become a less distinct topographic feature towards its ends.

The mainshock occurred at the intersection of the two trends of aftershocks, and more than one type of faulting was active during the sequence. Motion on two or more fault planes during the mainshock may have contributed to the complexity of its seismograms, and made it impossible to fit orthogonal planes to the P wave first motions. Such a situation is rare but was noticed at Mudurnu Turkey [McKenzie, 1972]. There too the fault plane solutions of the principal aftershocks differed from those of the mainshock, and the discrepant first motions were nodal in character.

APPENDIX A

Here we report the analysis of surface waves from the mainshock. This analysis was frustrating because R1 and G1 were usually too large to be analyzed. Only at stations with very low magnifications, and apparently near nodes in the radiation patterns were R1 or G1 small enough to be digitized. At the same time G2 and G3 were clear at a few stations with high magnifications and apparently, in most cases, near maxima in the assumed radiation patterns. Our policy was to analyze all Rayleigh waves (R1) that were not too large and any G-wave that could be seen on the seismograms. Thus, the data analyzed are a mixture of Love and Rayleigh waves with varying path lengths (Table A1). We Fourier transformed the surface wave signal and estimated the spectral density at 100 sec (and in a few cases 150 and 200 sec). For this estimate, we used the mean of the spectral density between 80 and 120 sec (or between 130 and 170 sec or 180 and 220 sec). From Ben-Menahem et al. [1970], the amplitude spectral density $|\tilde{u}(T)|$ at a particular period T can be written as

$$|\tilde{u}(T)| = \frac{M_o}{\mu} \frac{T}{2\pi} \frac{G(f,p,s,h,A_Z)}{F(\Delta)}$$

where M_o = seismic moment, μ = shear modulus,

$$F(\Delta) = \sqrt{\sin \frac{\Delta}{a}} \exp(\gamma(T) \frac{\Delta}{a})$$

where Δ = epicentral distance in km, a is the radius of the earth, and $\gamma(T)$ is a measure of attenuation. Ben-Menahem et al.

[1970] tabulate $F(\Delta)$ and we used their values. G(f.p.s.,h, Az.) depends upon the parameters describing the fault plane solution (f.p the azumith to the station (Az.) and the focal depth (h). It can be written for Rayleigh waves as

$$G = \sqrt{(p_R P_R + s_R S_R)^2 + (q_R Q_R)^2}$$

or for Love waves as

$$G = \sqrt{(p_L P_L)^2 + (q_L Q_L)^2}$$

where lower case letters contain information about the fault plane solution and azimuth and upper case letters contain information about the depth of focus and earth structure. They are defined and tabulated in Ben-Menahem et al. [1970]. We used their tabulated values for a depth of 15 km in a "continental" earth structure.

For each of the three possible fault plane solutions we calculated M_o (Table A 1) from

$$M_o = \frac{2\pi\mu\tilde{u}(T)}{T} \frac{F(\Delta)}{G}$$

We assumed that $\mu = 3.3 \times 10^{11}$ dynes/cm^2. If the data were free of error and one of the assumed fault plane solutions were correct, then in principle the calculated values of M_o would be the same for each station. In fact, for each assumed fault plane solution the calculated values scatter a great deal and

do not support any of the solutions. Figure A1 shows the range of scatter. Part of the scatter is probably due to the proximity of some stations (eg. TRN or ALQ) to nodes in one or more of the radiation patterns. Therefore, slight errors in azimuth cause large errors in calculated spectral densities and moments. The data are probably of mixed quality also. The estimate of $|\tilde{u}(T)|$ are surely better for the recordings of G2 and G3 than for R1 and G1. However, because of the longer paths, the values of F (Δ) and their uncertainties are larger for G2 and G3. Because of the scatter, the surface waves do not help much to discriminate among the possible fault plane solutions.

Table A1 lists the calculated values of M_o for each station and for each of the three possible fault plane solutions in Figure 6. Although the scatter in values is large, the averages for each solution are comparable. Ignoring the high value from TRN for the strike-slip solution the geometrical average of eighteen estimates is 4.3×10^{26} dyne-cm. The very small value of G(f.p.s.,h,Az.) for TRN makes the uncertainty in M_o determined from it so large that it is excluded from the average. For the pure thrust solution, the geometrical average of nineteen estimates is 6.2×10^{26} dyne-cm, and for Ni's [1978] oblique slip solution, it is 5.2×10^{26} dyne-cm. Zakharova and Chepkunas [1977] estimate the moment to be 1.3×10^{26} dyne-cm, from recordings made at Obninsk, USSR.

Let us assume that $M_o = 5 \times 10^{26}$ dyne-cm. For a fault length $\ell = 30$ km and width $w = 20$ km, and with $\mu = 3.3 \times 10^{11}$ dynes/cm^2, the average slip would be $\bar{u} = 2.5$ meters. The stress drop given by Knopoff [1978]

$$\Delta\sigma = \frac{1}{2} \frac{\mu\bar{u}}{w}$$

would be twenty one bars. Given the uncertainty in w alone, this estimate is uncertain by at least a factor of four.

ACKNOWLEDGEMENTS

We thank K. Evans, G.C.P. King and D. McKenzie for helpful criticism. J.J. thanks Shell International Oil Company for a Scholarship and support in the United States.

This work was supported in part by the Advanced Research Projects Agency of the Department of Defense, by the U.S.G.S., Contract # 14-08-001-16758 and by NSF grant # 77-23017 EAR.

REFERENCES

Ben-Menahem, A. , M. Rosenman, and D.G. Harkrider, Fast evaluation of source parameters from isolated surface wave signals, 1, Universal tables, Bull. Seismol. Soc. Amer., 60, 1337-1387, 1970.

Burtman, V.S., The Talasso-Fergana and San Andreas strike-slip faults (in Russian), in Faults and Horizontal Movements of the Earth's Crust, Trans. Geol. Inst. Acad. of Sci. USSR, 80, 128-151, 1963.

Burtman, V.S., A.V. Peive, and S.V. Rushentsev, The main strike-slip faults of the Tien Shan and Pamir in Faults and Horizontal Movements of the Earth's Crust, Transactions of the Institute of Geology, Academy of Sciences of the USSR, Issue 80, 1963.

Chen, W.P., P. Molnar, Seismic moments of major earthquakes and the average rate of slip in central Asia, J. Geophys. Res. 82, 2945-2969, 1977.

Fitch, T.J., and J.A. Jackson, Fine structure of mantle seismic zones from differential arrival time residuals and relative locations, J. Geophys. Res. (in press), 1979.

Fukao, Y., Source process of a large deep focus earthquake and its tectonic implications - the western Brazil earthquake of 1963, Phys. Earth Planet. Int., 5, 61-76, 1972.

Jackson, J.A., and T.J. Fitch, Seismotectonic implications of relocated aftershock sequences in Iran and Turkey, Geophys. J. Roy. Astron. Soc., (in press), 1979.

Khalturin, V.I., T.G. Rautian, and P. Molnar, The spectral content of Pamir-Hindu Kush intermediate depth earthquakes, Evidence of a High-Q zone in the Upper Mantle, J. Geophys. Res., 82, 2931-2943, 1977.

McKenzie, D.P., Active tectonics of the Mediterranean region, Geophys. J. Roy. Astron. Soc., 30, 109-185, 1972.

McKenzie, D., Active tectonics of the Alpine-Himalayan belt, The Aegean Sea and surrounding regions, Geophys. J. Roy. Astron. Soc., 55, 217-254, 1978.

Molnar, P., T.J. Fitch, and F.T. Wu, Fault plane solutions of shallow earthquakes and contemporary tectonics in Asia, Earth and Planet. Sci. Lett., 19, 101-112, 1973.

Molnar, P. and P. Tapponnier, Cenozoic tectonics of Asia, effects of a continental collision, Science, 189, 419-426, 1975.

Molnar, P., and P. Tapponnier, Active tectonics of Tibet, J. Geophys. Res., 83, 5361-5375, 1978.

Ni, J., Contemporary tectonics in the Tien Shan region, Earth Planet. Sci. Lett., 41, 347-354, 1978.

Patton, H., Source and propagation effects of Rayleigh waves from Central Asian Earthquakes, Ph.D. Thesis, Massachusetts Institute of Technology, 277 pp., 1978.

Peive, A.V., V.S. Burtman, S.V. Ruzhentsev, and A.I. Suvorov, Tectonics of the Pamir-Himalayan sector of Asia, pp. 441-462, Repts. 22nd session, Int. Geol. Congr., Part XI, Himalayas and Alpine Orogeny, New Delhi, India, 1964.

Ruzhentsev, S.V., Transcurrent faults in the South East Pamir in Faults and Horizontal Movements of the Earth's Crust, Transactions of the Institute of Geology, Academy of Sciences of the USSR, Issue 80, 1963.

Solomon, S.C., and B.R. Julian, Seismic constraints on Ocean-ridge mantle structure: anomalous fault plane solutions from first motions, Geophys. J. Roy. Astron. Soc., 38, 265-285, 1974.

Tapponnier, P., and P. Molnar, Active faulting and tectonics in China, J. Geophys. Res., 82, 2905-2930, 1977.

Tapponnier, P., and P. Molnar, Active faulting and Cenozoic tectonics of the Tien Shan, Mongolia and Baykal regions, J. Geophys. Res. (in press), 1979.

Thatcher, W. and J.N. Brune, Seismic study of an oceanic ridge earthquake swarm in the Gulf of California, Geophys. J. Roy. Astron. Soc., 22, 473-489, 1971.

Whitcomb, J., C. Allen and J. Garmany, and J. Hileman, San Fernando earthquake series 1971, focal mechanism and tectonics, Rev. Geophys. Space Phys., 11, 693-730, 1973.

Wyss, M., and J.N. Brune, The Alaska earthquake of March 28, 1964. A complex multiple rupture, Bull. Seism. Soc. Am., 57, 1017-1023, 1967.

Zakharova, A.I. and L.S. Chepkunas, Dynamic parameters of the foci of strong earthquakes as obtained from Spectra of Longitudinal waves at the station at Obninsk, Izvestiya, Phys. of the Solid Earth, 13, 81-87, 1977.

FIGURE CAPTIONS

Fig. 1. Tectonic setting of the Pamir and Tien Shan. Adapted from Molnar and Tapponnier [1975] and Chen and Molnar [1977].

Fig. 2. Geological and structural map of the southern Tien Shan and Pamir, modified from Burtman et al. [1963] and Ruzhentsev [1963]. Filled circles indicate the relative locations of the main events in the 1974 sequence (see Figure 4) and the pattern could be displaced up to about 25 km. Thrust dips marked with filled symbols are from published reports, those with open symbols are inferred from Landsat Imagery. The area where the Pamir-Karakorum fault (P-KK) meets the Pamir Thrust (PT) is marked schematically. It is not clear from published work or from the Landsat Imagery whether the Pamir Thrust is continuous east of the Pamir-Karakorum Fault, which is also indistinct in this area. Molnar and Tapponnier (1975) mark a southerly dip for the western part of the Pamir Thrust, whereas a clear northerly dip is inferred from Figure 3 for the thrust east of the Pamir-Karakorum Fault. It is significant that the shock of 14.9.69 has a well controlled steeply dipping southerly plane whereas further west 11.8.74b has a shallow dipping plane to the south (Figure 4 and 5). The dashed area marks the extent of Figure 3. The Tien Shan-Kun Lun fault (TS-KL) includes

the Talasso-Fergana fault in Figure 1. The Pamir-Karakorum and Kungur (KF) faults continue southeast into the Karakorum fault. The Karakul thrust is marked by KT, Lake Karakul by LK, and Kashgar by K.

Fig. 3. Landsat imagery of the area marked in Figure 2. Latitude-longitude crosses marked on the photograph are approximate.

Fig. 4. Relocations of major events ($m_b \geq 5.0$) relative to 27.8.74 (number 51). All except 11.5.67 used more than 100 stations in the relocation (Table 1). Standard errors, checked by Chi-squared tests, are less than 5 km in any direction for these events (see Table 1). Station distributions are good for events of this size and so systematic errors in relative locations should be small. Sequence numbers identify the events in 1974 in Table 1. Earlier events are marked by open circles. 29.8.63 and 14.9.69 were not relocated. Their locations are those given by the ISC, and the fault plane solutions are from Tapponnier and Molnar [1979]. New fault plane solutions are shown in Figures 6 and 7 and parameters are listed in Table 2. No P wave solution is available for 24.7.71 and the solution shown is from a linear moment tensor inversion by Patton (1978). Dashed lines mark trends of aftershocks corresponding to one of the fault planes in the fault plane solution (see text).

Fig. 5. All relocated events in the 1974 sequence. Events are numbered in order of occurrence, and correspond to numbers in Figure 4 and Table 1. Large filled circles are major shocks in Figure 4 and small filled circles are shocks with more than 70 stations in their relocations. For each $m_b \geq 4.9$. Open circles used more than 23 stations in their relocations, and although their standard errors are less than 10 km, they are more likely to be affected by poor station distributions than the other two groups.

Fig. 6. Lower hemisphere, equal angle projection of first motions and selected seismograms for the mainshock 11.8.74a. Fault planes drawn as solid lines represent our preferred solution. The dashed lines are a pure thrusting solution and the dotted lines the solution of Ni [1978]. Seismograms are all from the long period instruments of the WWSSN. Upward first motions are compressional, and are plotted as solid symbols, dilatations are open symbols, X's denote nodal readings, and arrows give first motion of S waves. P and T show positions of the P and T axes of the preferred solution.

Fig. 7. New fault plane solutions of other earthquakes. Symbols same as figure 6. All were assumed to have occurred in the crust with a focal velocity of 6.5 km/sec. Table 2 lists the parameters of the solutions.

Fig. 8. ISC residuals from the mainshock vs. epicentral distance for stations in the azimuth range 320°-20°. Filled circles are those whose arrivals were reported as impulsive. Open circles were emergent or of unspecified quality.

Fig. A1. Moments for the mainshock calculated from Love and Rayleigh waves at different stations, assuming different focal mechanisms (see Table A1). The scatter does not support any particular solution. This may simply indicate that rupture occurred on more than one fault plane during this earthquake.

Table A1. Data for Surface Wave Analysis

Station†	Phase	T (sec)	Δ (o)	AZ (Δ)	$\tilde{U}(T)$ (cmsec)	F(Δ)	G* (10^{-19} cm^{-2})
ADE	R1	100	95	132	0.31	1.7	87
AFI	R1	100	118	85	0.19	1.9	658
ALQ	G3	100	466	0	0.052	31.3	209
		150	466	0	0.16	8.7	119
		200	466	0	0.20	3.5	80
ATU	G2	100	321	104	0.19	8.6	647
		150	321	104	0.16	3.6	363
BUL	R1	100	73	224	0.26	1.7	114
KIP	R1	100	102	48	0.12	1.8	203
KON	G3	100	404	319	0.10	16.6	946
		150	404	319	0.19	5.4	533
NUR	G3	100	397	321	0.091	14.6	919
RAB	R1	100	84	101	0.20	1.6	546
SJG	R1	100	111	319	0.17	1.9	224
SPA	R1	100	129	180	0.28	1.9	664
	G1	100	129	180	0.43	2.3	209
STU	G2	100	314	124	0.20	8.7	991
TRN	R1	100	115	310	0.28	1.9	23
WEL	R1	100	122	120	0.31	1.9	203

*Pure strike slip faulting. Strike = 129°, dip = 90°, slip = 180°
**Pure thrust faulting strike = 77°, dip = 22°, slip = 90°
***Oblique thrusting strike = 55°, dip = 66°, slip = 26°
†All R1 from vertical components, ALQ-EW (back-az = 0°), ATU-NS (back-az = 252°), KON-NS (back-az = 87°), NUR-NS (back-az = 102°), SPA-NS (back-az = 129°), STU-NS (back-az = 76°)

Mo* (10^{26}dyn-cm)	G** (10^{-19}cm^{-2})	Mo** (10^{26}dyn-cm)	G*** (10^{-19}cm^{-2})	Mo*** (10^{26}dyn-cm)
12.6	409	2.7	246	4.4
1.1	85	8.8	398	1.9
16.1	156	21.6	145	23.3
16.2	86	22.4	78	24.7
9.1	58	12.5	52	14.0
5.2	297	11.4	275	12.3
2.2	163	4.9	153	5.2
8.0	230	4.0	255	3.6
2.2	200	2.2	136	3.3
3.6	295	11.7	847	4.1
2.7	166	8.5	477	3.0
3.0	281	9.8	841	3.3
1.2	165	4.0	413	1.6
3.0	459	1.5	153	4.4
1.7	538	2.1	682	1.6
9.8	156	13.1	145	14.1
3.6	357	10.1	722	5.0
48.0	393	2.8	100	11.0
6.0	311	3.9	495	2.5

Table 1 Location of Major Earthquakes

Sequence No.	Date	Origin Time	Latitude	Longitude	Depth	m_b	Stations	Standard Errors (km) Lat.	Long.	Dep.
1	11.4.74	01 13 55	39.381	73.806	23	6.4	184	1.9	1.3	2.9
6	11.8.74	05 12 33	39.397	73.714	34	5.4	148	2.4	3.3	0.3
8	11.8.74	05 23 52	39.403	73.750	20	5.6	134	0.4	1.9	6.4
10	11.8.74	07 02 08	39.452	73.846	(-15)	5.2	118	0.8	1.7	4.8
12	11.8.74	09 08 58	39.333	73.859	31	5.1	100	3.7	1.0	1.8
20	11.8.74	20 05 30	39.472	73.662	23	5.8	165	0.5	2.4	3.2
21	11.8.74	21 21 33	39.492	73.645	28	5.9	179	0.6	3.3	1.8
51	27.8.74	12 56 03	(39.520)	(73.820)	(19)	5.8	(278)	-	-	-
54	27.8.74	17 33 58	39.412	73.848	17	5.3	130	0.3	1.2	3.6
60	3.9.74	19 41 19	39.466	73.709	22	5.4	153	0.1	2.6	3.1
68	16.9.74	16 45 57	39.532	73.582	16	5.0	103	1.4	0.3	4.1
	11.5.67	14 50 57	39.406	73.774	8	5.5	89	1.6	0.8	4.7
	24.7.71	11 43 39	39.405	73.208	56	5.5	108	0.2	6.6	1.7

Events in Figure 4 relocated relative to number 51. The sequence number identifies the event in Figure 4. Origin Time is from the ISC bulletin.

Table 2. Poles and axes for new first motion fault plane solutions

Date	Location °N	Location °E	Poles az	Poles pl	Poles az	Poles pl	P axis az	P axis pl	T axis az	T axis pl	B axis az	B axis pl
11 May 67	39.33	73.74	042	00	132	00	177	00	087	00	---	9
11 Aug 74 (01 13)	39.46	73.83	039	00	129	00	174	00	084	00	---	9
11 Aug 74 (20 05)	39.47	73.65	180	23	000	67	000	22	180	68	090	0
11 Aug 74 (21 21	39.47	73.63	175	00	355	90	355	45	175	45	085	0
27 Aug 74	39.67	73.83	262	04	172	00	307	03	217	03	082	8

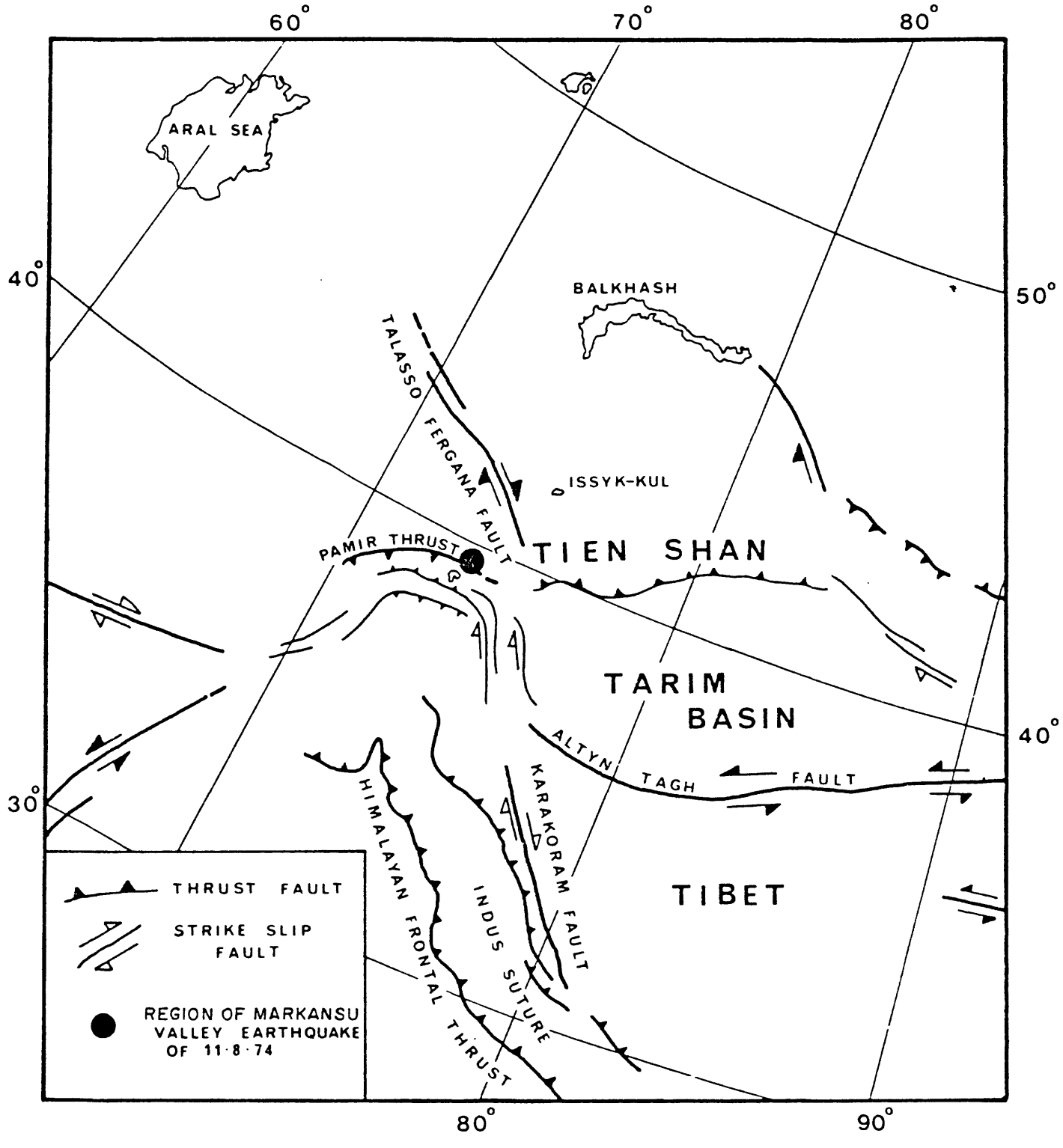
60°
70°
80°
40°
50°
30°
40°
80°
90°
ARAL SEA
BALKHASH
TALASSO FERGANA FAULT
ISSYK-KUL
PAMIR THRUST
TIEN SHAN
TARIM BASIN
ALTYN TAGH FAULT
KARAKORAM FAULT
HIMALAYAN FRONTAL THRUST
INDUS SUTURE
TIBET
THRUST FAULT
STRIKE SLIP FAULT
REGION OF MARKANSU VALLEY EARTHQUAKE OF 11·8·74

Fig 1

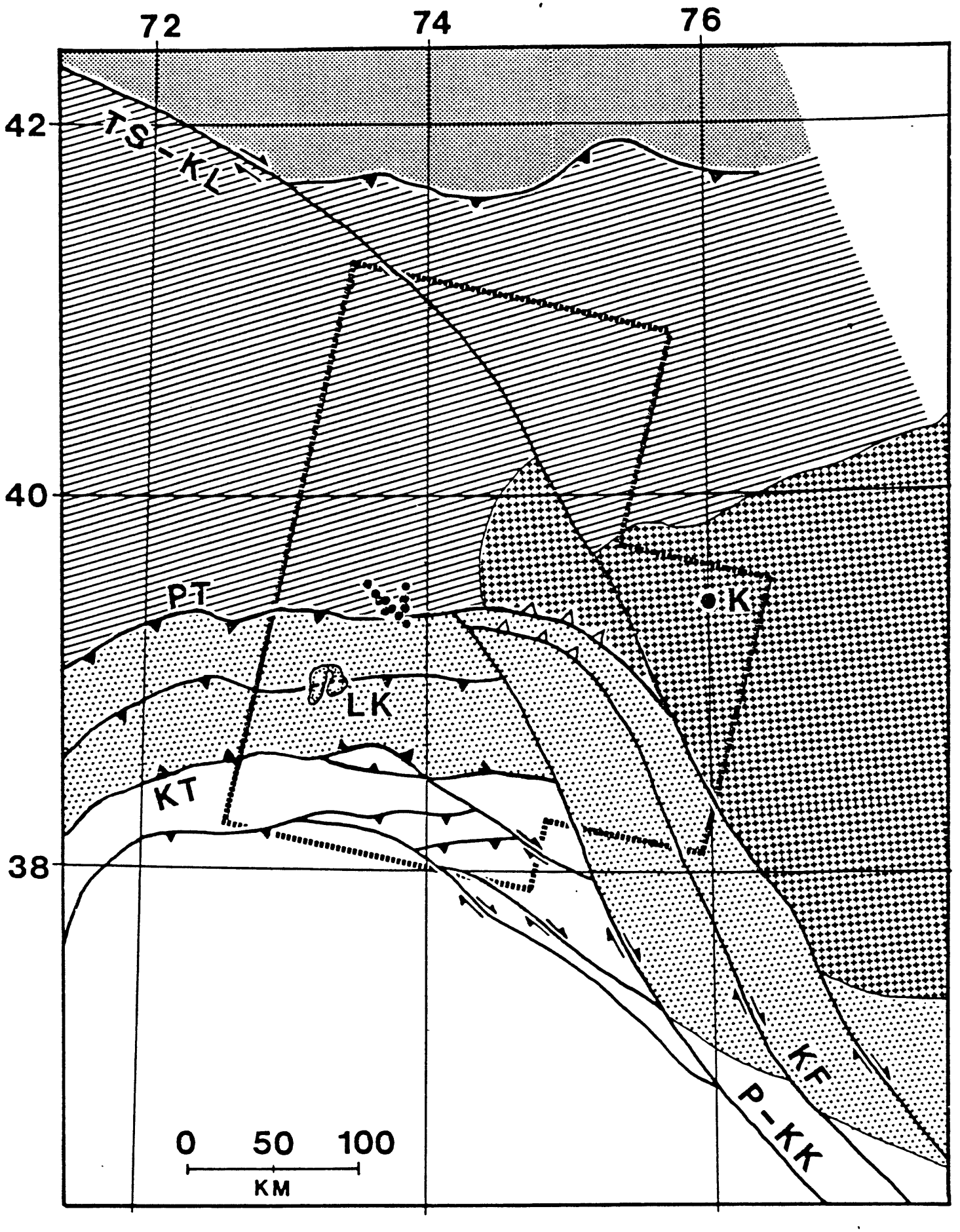

Fig 2

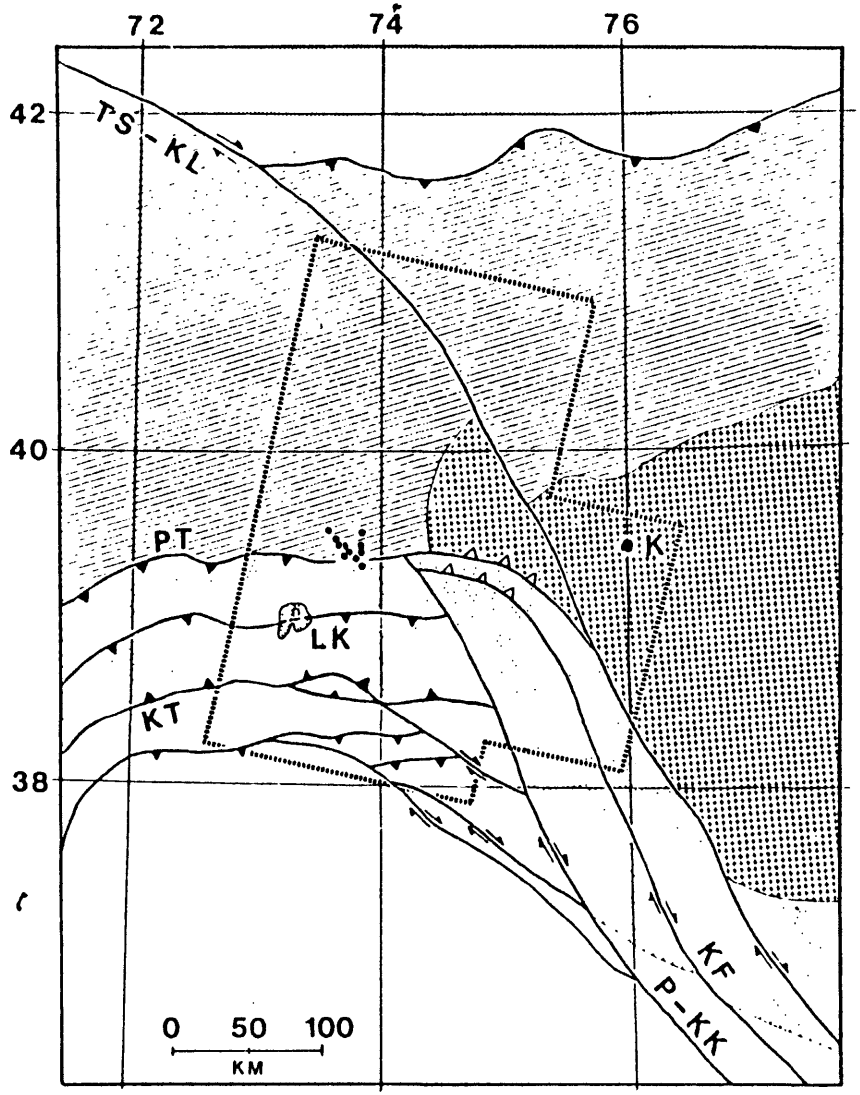

KEY TO FIGURE 2

"Caledonian" early Paleozoic metamorphic and igneous rocks in the axial region of the Tien Shan.

"Hercynian" late Paleozoic folded rocks of the Southern Tien Shan

Precambrian Tarim Platform.

"Hercynian" folded region of the Northern Pamir and Western Kun Lun.

Mesozoic folded region of the Central and Southern Pamir.

147

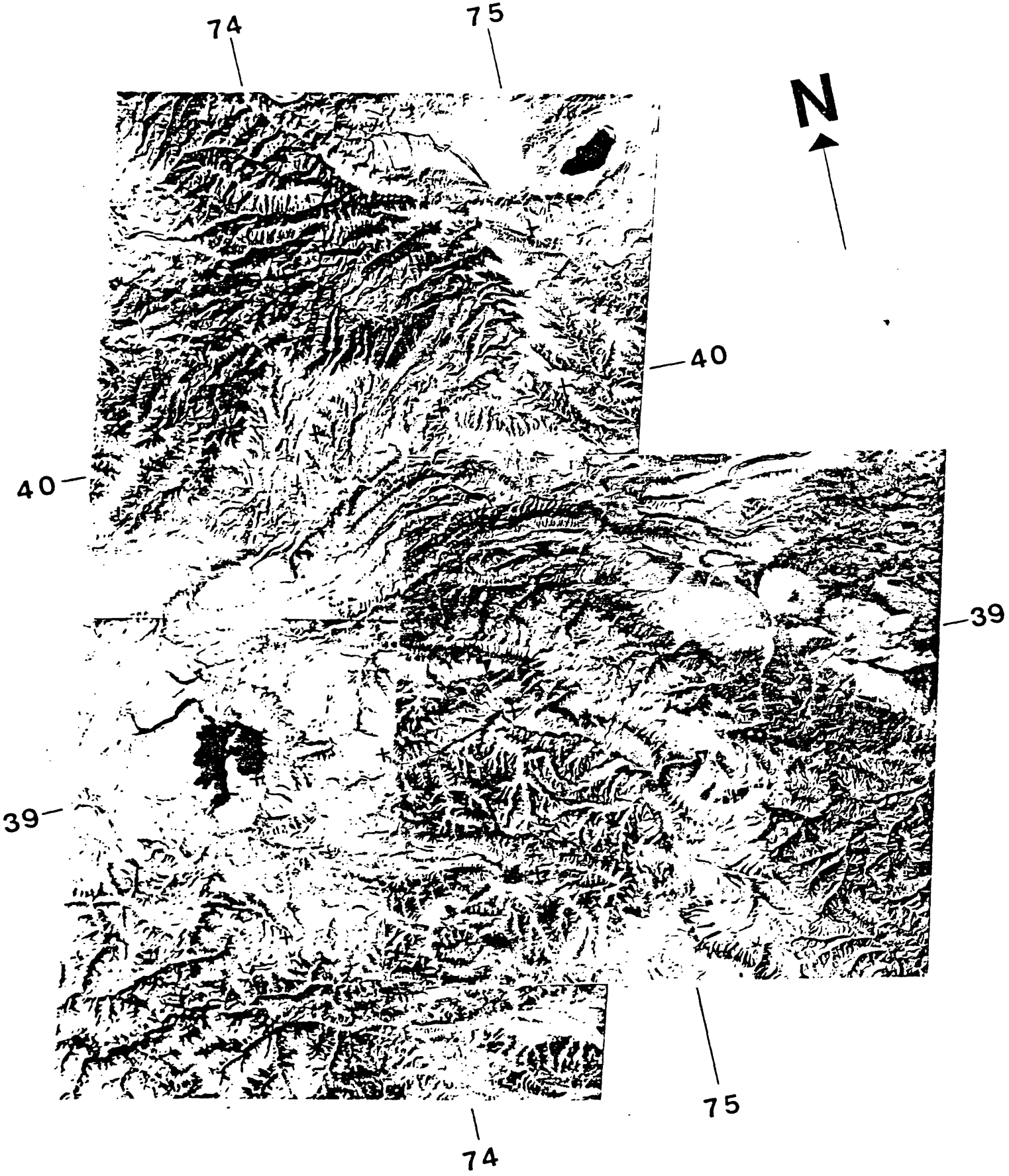

Fig 3

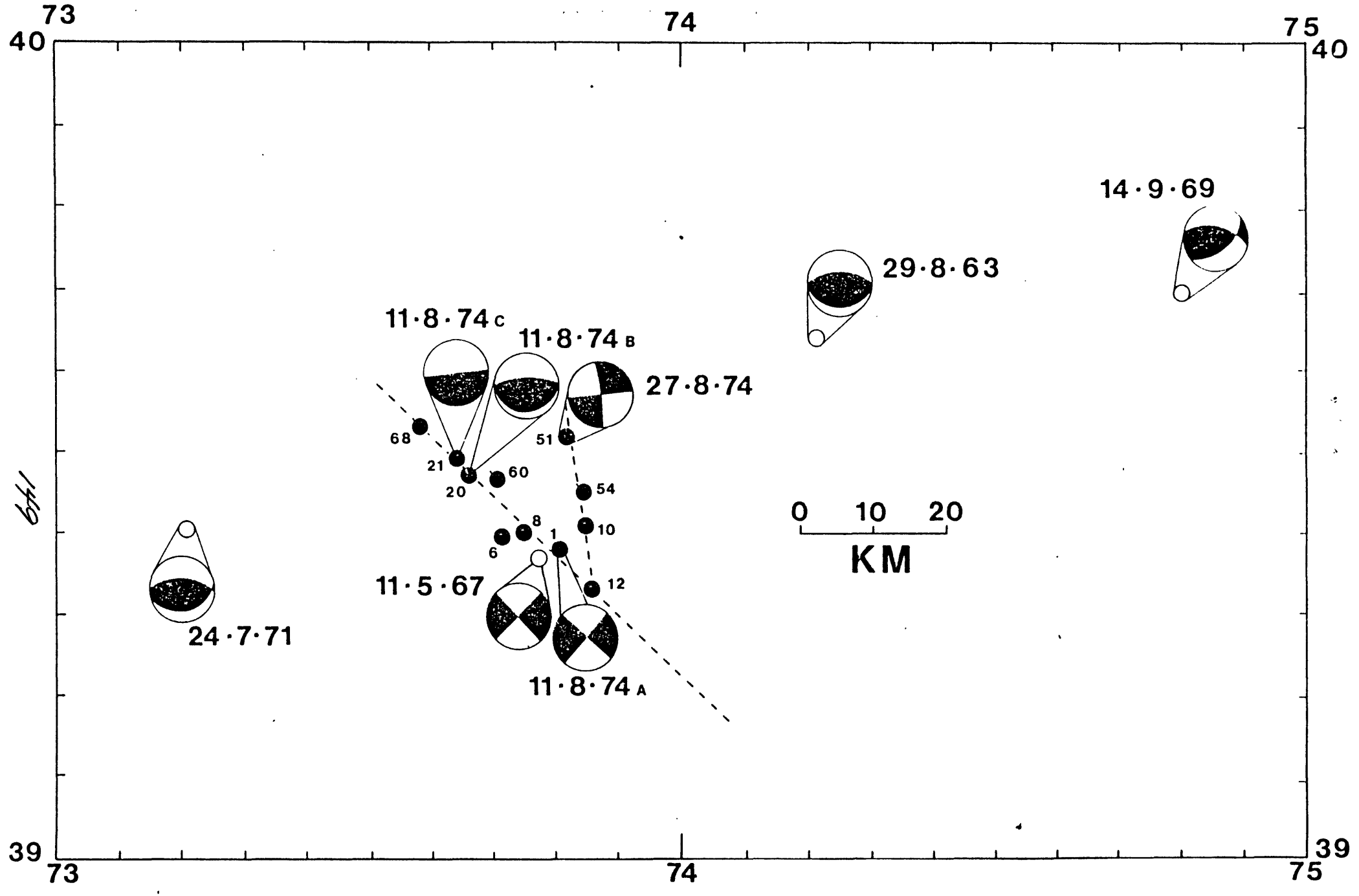
73
74
75
40
39
14·9·69
29·8·63
11·8·74 C
11·8·74 B
27·8·74
68
21
20
60
51
54
8
1
10
6
12
11·5·67
24·7·71
11·8·74 A
0 10 20
KM

Fig. 4

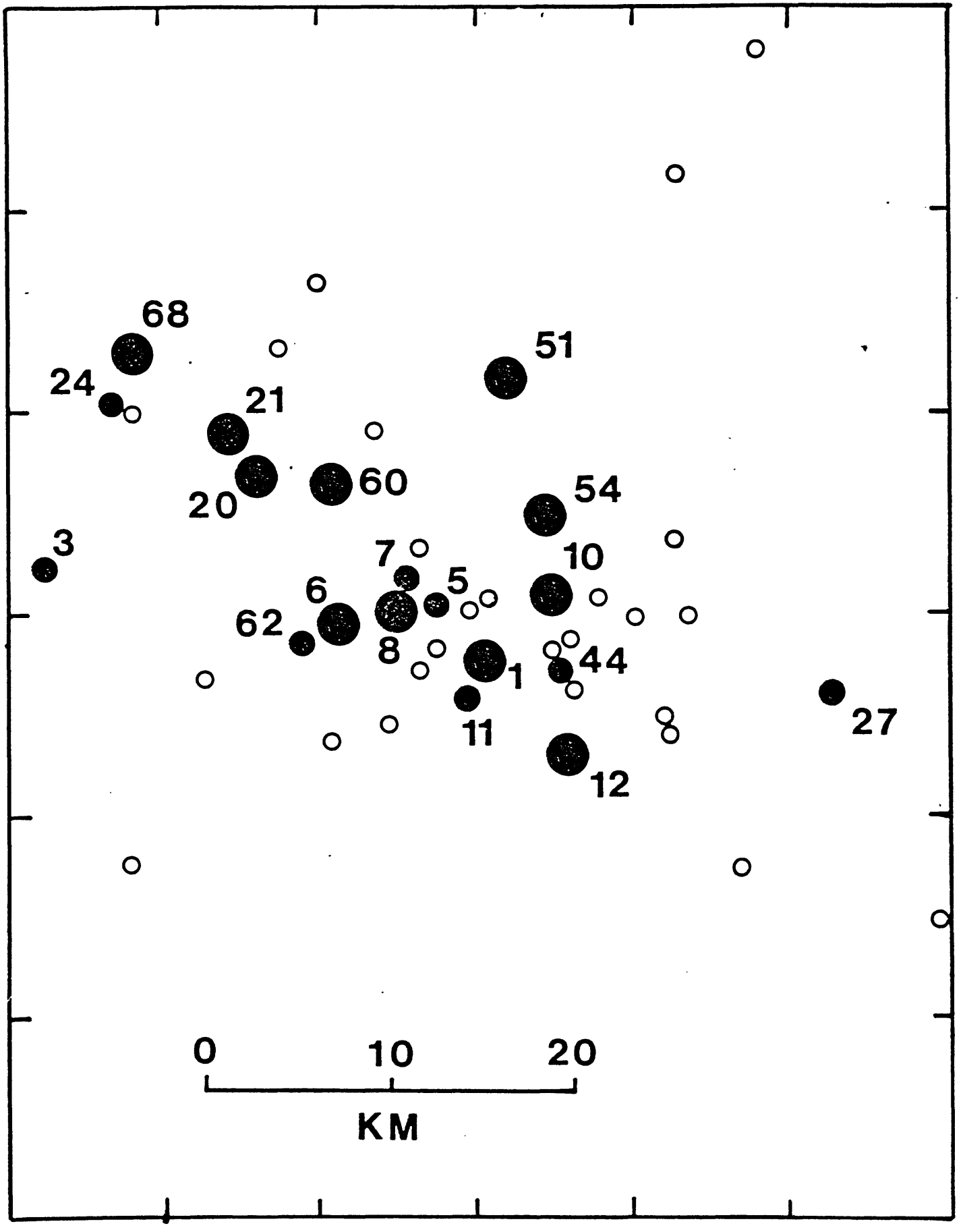

Fig. 5

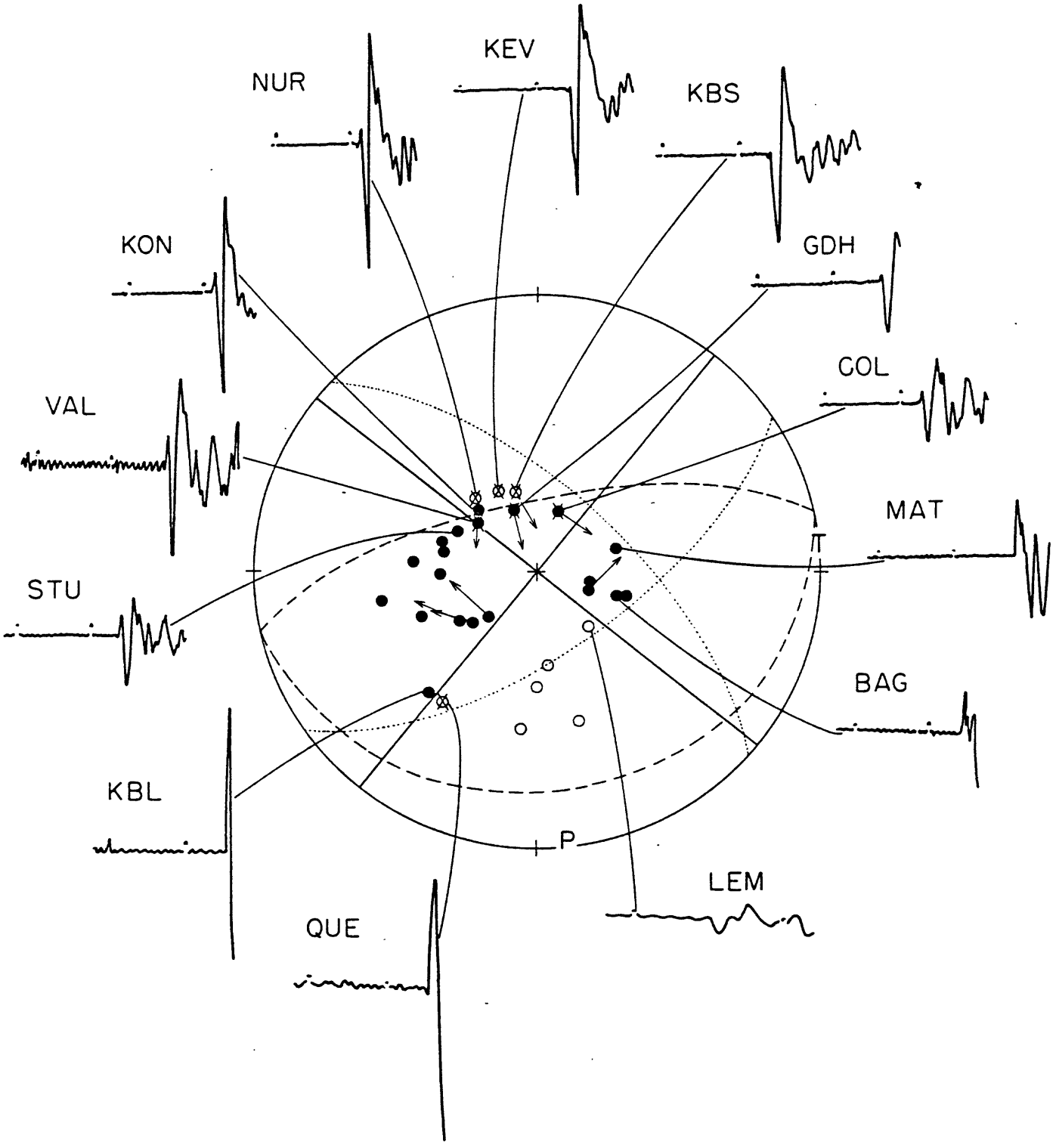

Fig. 6

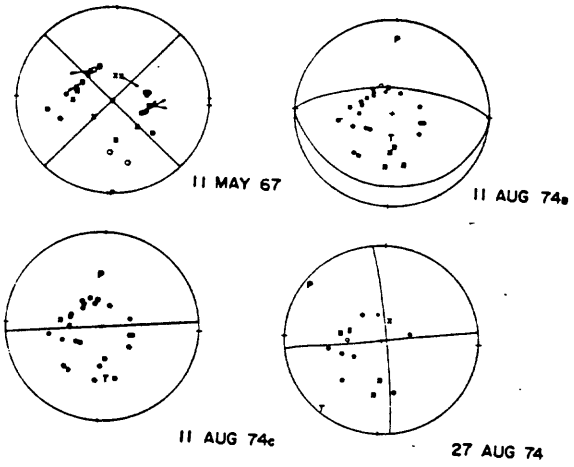

Fig 7

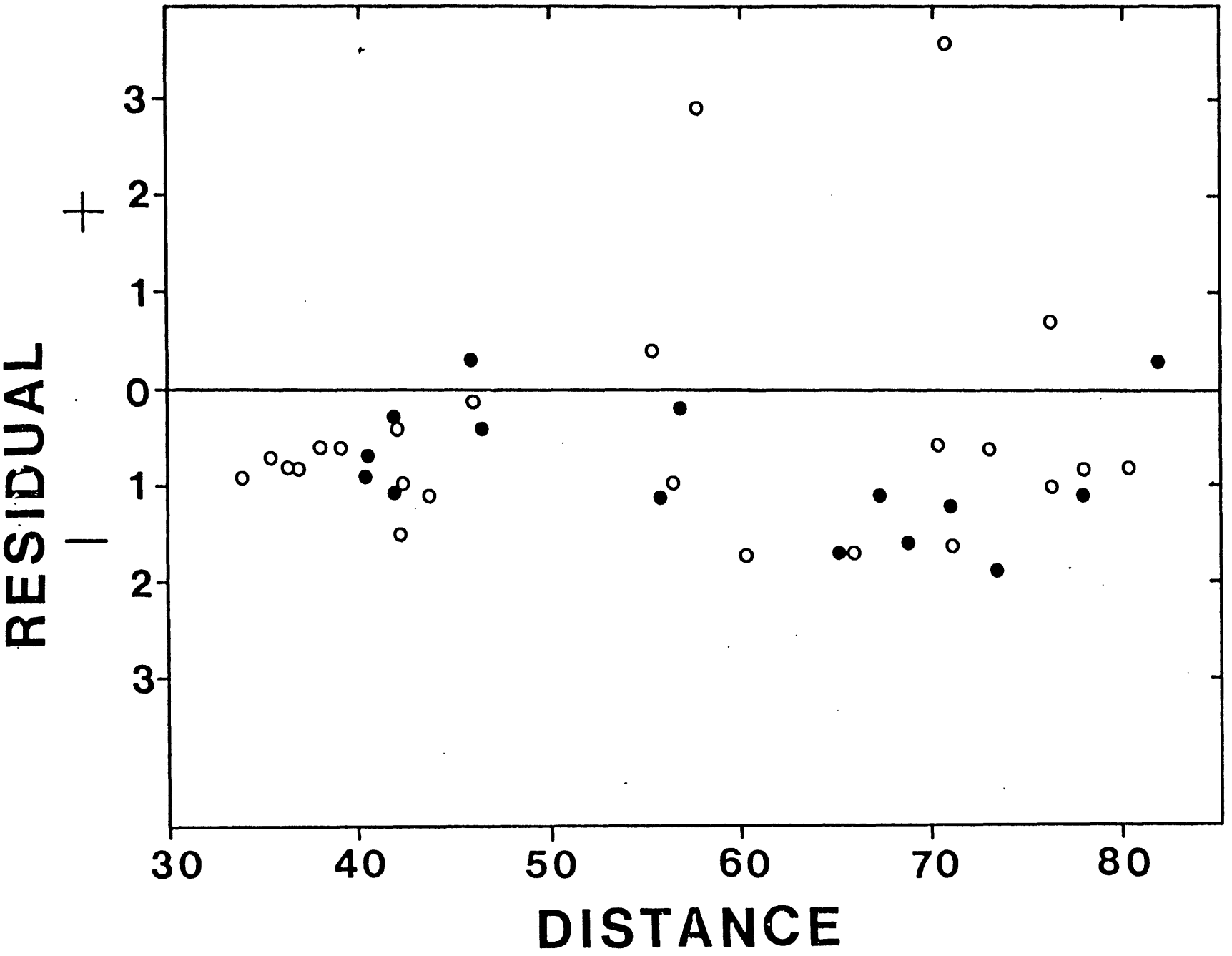

Fig 8

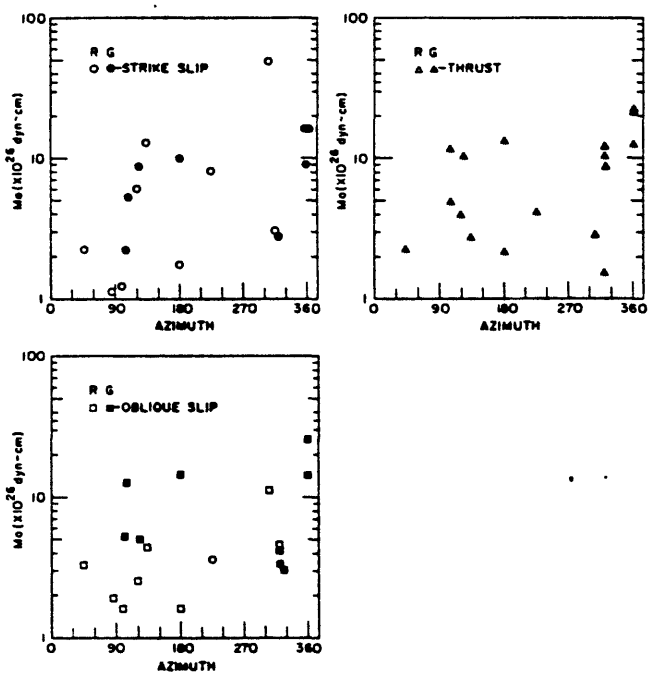
R G
○ ●-STRIKE SLIP
R G
△ ▲-THRUST
R G
□ ■-OBLIQUE SLIP
Mo(x10^25 dyn-cm)
AZIMUTH
100
10
1
0
90
180
270
360

Fig A1

PLEASE SUBMIT ONE ORIGINAL AND FOUR COPIES

6

The Geological Society of America
Telephone: (303) 447-2020

See instruction sheet for deadlines and addresses

CLASSIFICATION

You must specify one. If more than one category is appropriate, indicate your order of preference by numbers. Be specific.

ABSTRACT FORM

Exact format shown on instruction sheet must be followed.

Lucile Jones, Department of Earth and Planetary Sciences, Massachusetts Institute of Technology, Cambridge, Mass. 02139
Wang Biquan and Xu Shaoxia, Institute of Geophysics, Academia Sinica, Peking, People's Republic of China

We have examined the locations and mechanisms of the foreshocks to the 4 February 1975 Haicheng earthquake. The foreshocks were located using four stations relative to a master event. All occurred within 5 km of each other. There appears to be two clusters of foreshock activity. The largest with the larger foreshocks appears to form one trending north-northeast. The second cluster is more dispersed and lies to the northwest of the first. The mainshock rupture plane trends west-northwest but with a cluster of aftershocks trending north-northeast from the mainshock. Thus it is possible that the majority of the foreshocks occurred on a different plane from the mainshock.

We also examined the amplitude ratios (Ap/As) recorded at each station. While the ratios were relatively constant at the more distant (Δ=100-200 kilometers) stations, two very different waveforms were recorded throughout the sequence at Yingkou (Δ=20 kilometers). However, if the foreshocks did occur on two planes as suggested by the locations of the epicenters, because the two planes are almost but not quite perpendicular, the fault plane solutions for events on the two planes would be quite similar. Theoretically the slightly different fault plane solutions of the mainshock and the largest foreshock would produce relatively consistent ratios at the distant stations but two different ratios similar to ours at Yingkuo. However, a definite correlation between the different waveforms recorded at Yingkuo and the two clusters of activity could not be made.

archaeological geology
coal geology
economic geology
engineering geology
extraterrestrial geology
general geology
geochemistry
geology education
geomorphology
(geophysics)
geoscience information
history of geology
hydrogeology
marine geology
mathematical geology
mineralogy/crystallography
paleontology/paleobotany
petrology
  experimental
  igneous
  metamorphic
Precambrian geology
Quaternary geology
sedimentology
  sedimentary petrology
stratigraphy
structural geology
(tectonics)
volcanology
OTHER
_____
_____
_____

☒ Oral ☐ Poster ☐ Either

☒ Symposium Earthquake Prediction
(title of symposium for which abstract was invited)

PLEASE NOTE: All invited symposium abstracts (original plus two copies) must be sent to the organizers of the respective symposia according to deadlines established by symposium organizers.

Speaker Lucile Jones

GSA Member ☐
GSA Student Associate ☐
Member of Society Associated with GSA ☐ Which _____
Nonmember ☒

I will be available to serve as a cochairman for a technical session on or concerning _____

For correspondence purposes, I can be reached at the following address: _____

Phone numbers and dates where speaker can be contacted _____

155

Appendix B

The Role of Conjugate Faults in the Development and Occurrence of Earthquakes

Lucile Jones, Deng Qidong and Jiang Pu
(Massachusetts Institute of Technology)
(State Seismology Bureau Institute of Geology)

(English translation of a paper published in Di Zhen Di Zhi (Seismology and Geology), Beijing, 1980)

Fault plane solutions of the major earthquakes occurring within the China plate show that the events are consistent with their regional stress field as determined from geologic data (Deng et al, 1976, 1979). Nevertheless, these intraplate earthquakes can be divided into types. One type occurs on the boundary faults of the major fault blocks within the China plate and are clearly associated with the regional deep active faults of fault basins. For instance, the 7 February 1973 LuHwo earthquake (M=7.9) in Sichuan occurred on the Xian-Shuihe (Kanting) fault which is the northern boundary of the Sichuan-Yunnan fault block. The second type of earthquakes occurs not on the region's deep, active faults but rather on minor faults, in some cases on faults not previously recognized. For instance, although four major faults that all have evidence of large Quaternary movement exist in the Tangshan area, the 28 July 1976 Tangshan earthquake (M=7.8) was located on a minor fault (40 km long) with little evidence of recent activity (Guo et al, 1976). This type of earthquake usually occurs within a fault block or an area of complex geological structure.

It appears that for the second type of earthquake, the main shock plane often is not the only plane active during the earthquake generating process. Besides concentrating along the mainshock plane, the precursors, foreshocks and aftershocks for this type of event also appear along conjugate faults within the area. Moreover, for this type of event, earthquakes precursors are, as a rule, distributed over a large area, although concentrated along the regional tectonic structures of different orientations. The precursor field is often larger than the epicentral area and its distribution and size may be determined by the pertubations of the stress field by the regional tectonic structures (Deng et al, 1976; Jiang et al, 1979).

The first author of this paper researched characteristics of the Haicheng forshock sequence with Wang Biquan and Xu Shaoxie of the Institute of Geophysics of the State Seismology Bureau (L. Jones et al, 1979) and on the basis of the previous work of the second authors (Deng et al, 1979; Jiang et al, 1979 studied the temporal distribution and relation to geologic structures of the short term and imminent precursors of several earthquakes

including the Liaoning Province Haicheng, Hebei Province Tangshan and Sichuan Province Song pan earthquakes. These events are all of the second type of earthquake mentioned above. Naturally, types of earthquake precursors are varied and their characteristics very complicated, so that in our limited time we have researched only a small part of the problem. It was, therefore, impossible for us to consider all precursory phenomena.

4 February 1975 Haicheng Earthquake (m=7.3)

The geologic structure of Liaoning Province where the Haicheng earthquake occurred is dominated by two sets of nearly perpendicular faults (Figure 1). The more fundamental system trends NNE, one of the main structural trends of eastern China. Faults of the other system trend WNW. These are structurally more minor features often limited by the NNE trending faults.

The predominant structure of western Liaoning is the Xialiaohe faulted depression which is controlled by the NNE trending faults, the largest of which is the Niujiu-Youyangou Fault. Within the epicentral area, the boundary between the Xialiaohe depression and the E. Liaoning uplift is composed of the Jinshingling and the Shuangtaizi-Zahejiabazi faults, which could be extensions of the major Tangcheng-Lujiang fault of northeast China. Within the E. Liaoning uplift there are several other NNE trending faults (Figure 1). Near the epicentral area is the NW trending Dayanghe fault whose western terminus coincides with the epicenter.

The Haicheng earthquake occurred in the area between the terminus of the NW Dayanghe fault and the Niujiu-Youyangou fault (Figure 1). The instrumentally determined epicenter of the mainshock was located just at the western end of the Dayanghe fault and the after shocks lay primarily along a line WNW from that epicenter (Figure 2). The intensity distribution also followed this WNW direction. Moreover, nine compressive enechelon fractures along this direction indicating left-lateral slip in the WNW direction. Therefore, this WNW direction is believed to be the mainshock fault plane and possibly fracture of fresh rock (Deng et al, 1976).

Fault plane solutions of the Haicheng earthquake show that the two planes lay N22^{o}E and N68^{o}W, with right-lateral and left-lateral movement respectively, (Wu, 1976) and the P axis trends N67^{o}W. These two planes are consistent with both the WNW mainshock fault breaks and the regional NNE structures.

Although the main faulting occurred on the WNW fault, evidence exists that the NNE faults experienced activity or were at least affected by the stress concentration. It appears that some of both the foreshocks and aftershocks occurred on a NNE trending plane. The foreshocks occurred very close together (approximately within 5 km of each other) and essentially at the epicenter of the mainshock. However, they do appear to have occurred in two separate clusters one of which has the appearance of a NNE trending plane (Jones et al, 1979). They were located at the western edge of the Ximu river valley. Also, although most of the aftershocks were distributed along a WNW plane, there were also a few that followed a NNE direction. There were several magnitude 2 and 3 events northeast of the mainshock epicenter at Shisi and southwest at Gaixiam Xiongyu (Figure 2). The location of the former cluster is consistent with an extension of the NNE plane determined by the foreshock epicenters; the latter are on the southern portion of the NNE trending Jinshanling fault.

The foreshocks are located in Proterozoic schists and no fault has been directly observed in this area. However, a very straight, NNE trending river valley with obvious triangular facets along the western boundary hills (the above mentioned Ximu river valley) coincides with the locations of the foreshocks. Moreover, in these schists in the western hills, relatively well developed small fractures with approximately a N20^{o}E orientation occur. Therefore, it is quite possible that a NNE trending fault runs along the Ximu river valley probably reaching the Shisi area (where aftershocks occurred).

Other precursors also seem to have been affected by the NNE structures. The precursor field of the Haicheng earthquake was extensive, possibly extending as far as 400 or 500 kilometers (Deng et al, 1975), although the anomalies were mainly concentrated along the WNW and NNE trending faults of the Haicheng area (Jiang et al, 1979). The effect of the two tectonic systems was very evident for the short term and imminent precursors, especially the ground water anomalies - these including changes in the water level, in taste and color, and bubbling, muddying and swirling of the water (Zhu et al, 1979; Haicheng Seismological Brigade, 1975). These phenomena

began ten weeks before the mainshock but were concentrated in the few days immediately preceding it. Again, the majority of anomalies occurred along the eventual mainshock plane (74% of the reported points) but a large number of anomalies were distributed along a NNE direction, coinciding with the Jinshanling, Shuangtaizi-Zahojiabazi, and Jinzhou faults (60% - points lying at the intersection of the two trends were counted in both) (Figure 2). Also, several other NNE trending faults in the East Liaoning area had separate ground water anomalies. It is worthwhile to note that when the anomalies began to appear in December 1974, the 20 reported anomalies were concentrated along the Yalu river fault near Dandong in the eastern part of the peninsula. The eighty anomalies reported in January, 1975, occurred primarily along the northwest belt but the NNE trending Anshan belt also had anomalies. The 140 anomalies reported between 1 February and 4 February were concentrated in the northwest trending epicentral area but also appeared along the NNE trending Jinshangling fault which intersects the epicentral area. Thus the anomalies migrated towards the epicenter as the earthquake approached. Indeed, the Jinshangling fault had some of the most obvious anomalies. The Tanggangzi hot spring (on the northern section of the fault) stopped flowing for the first time ever known, three times before the earthquake. Moreover, the five wells found to be the most sensitive earthquake precursors during the Haicheng sequence lie within this fault zone (Figure 2).

Several other short term precursors of the Haicheng earthquake had a similar pattern of distribution. For instance, although the animal anomalies primarily followed the northwest trend of the mainshock plane, anomalies also appeared along the Jinzhou, Jinshanling and Yalu River faults. As well, both the mainshock plane and several NNE trending planes near the epicenter had radon, strain, telluric field, earthquake lightening, underground gas and other anomalies.

28 July 1976 Tangshan Earthquake (M=7.8)

The Tangshan earthquake occurred in the boundary zone between the Yanshan uplift belt and the North China Plain faulted depression. This boundary zone is composed of a stepping series of approximately EW or ENE trending faults but is also cut by NW and NNE trending structures forming grabens and horsts of which the Tangshan secondary fault block is one. The Tangshan block is bounded on all sides by four deep, large faults that all show evidence of recent activity so as to form a ENE trending parallelogram (Guo et al, 1977). However, as mentioned before, the Tangshan earthquake occurred not on one of these faults, but on a minor NNE trending fault within the Tangshan block.

The Tangshan earthquake produced a NNE trending surface rupture eight kilometers long. The trace showed right-lateral motion had occurred, reaching a maximum amplitude of 2-3 meters. No foreshocks were recorded (Hebei Provincial Seismology Bureau, 1977). The aftershock distribution was in general coincident with the fault plane of the mainshock. However, the aftershocks were concentrated at the north and south ends of the Tangshan Fault. Moreober, the two largest aftershocks (M7.1 and 6.9) were located in these two concentrations of aftershocks and the rupture plane of the M=6.9 aftershock trended northwest consistent with the trend of that area of aftershock activity. The fault plane solution of the Tangshan mainshock showed that the direction of the P axis was N65^{o}E (Qin Qun, 1976) corresponding to a maximum shear stress on both NNE and WNW trending planes.

Although the spatial distribution of the precursors to the Tangshan earthquake is quite complex, some definite patterns can be observed. Looking at the temporal development of the precursors, one can see that after the 1975 Haicheng earthquake, the anomalies in the Liaoning area diminished but the anomalies in the Beijing-Tianjin-Tangshan area continued to develop. By April, 1976, they had begun to enter the short-term stage (Hebei Provincial Seismology Bureau, 1977; Jiang Pu, 1979). In general, these anomalies were distributed along the northeast, northwest, and east-west trending geologic structures of the Tangshan region.

The change in electrical resistivity of the ground was most closely associated with the regional structures of all the anomalies. Within a 200 km area centered on Tangshan, nine of the fourteen operating electrical resistivity stations were in continuous operation since 1973. A long term drop in resistivity was recorded beginning in 1974, forming an area of anomalously low resistivity extending approximately 70 kilometers north-south and 300 kilometers east-west (Figure 3). The largest anomalies were at the three stations of Tangshan, Majia and Chang which showed a drop in resistivity before the earthquake of 5.5%, 17.6% and 6.4% respectively. By December 1975, the resistivity anamalies showed a definite linear pattern. On a map of the anomalies recorded before the earthquake in July 1976, one can see that the anomalous area followed both a northwest and northeast trend out from Tangshan and was larger than the epicentral area of the earthquake. These two anomalous areas coincide both with the aftershock area and the area of high seismic activity prior to the Tangshan earthquake, (Chang et al, 1979). The spatial distribution and temporal development of the resistivity anomaly also corresponds to the distribution and development of a long term (two to three years before the earthquake) precursory drop of the water table in the Tangshan area, (Jiang et al, 1979). This linear pattern in the anomalies could be in part due to the increase in seismic activity along nothwest trending faults prior to the earthquake.

The imminent macroscopic precursors[1] to the Tangshan earthquake appeared relatively late (compared to the Haicheng precursors), only reaching a high level one or two days before the earthquake (Hebei Provincial Seismology Bureau, 1977). The phenomena were similar to those of the Haicheng earthquake. Macroscopic ground water anomalies were recorded in Tangshan, Beijing, Tianjin and other areas but were most obvious in Tangshan. Large anomalies were seen sixteen hours before the earthquake primarily in the

---

[1]Macroscopic anomalies refer to phenomena reported by local observation groups rather than by instruments.

epicentral area distributed along a north-northeast direction. They appeared along the Tangshan fault which lies along an anticline and along other parallel anticlines. Seventy to eighty percent of the reported animal anomalies occurred within one day of the earthquake. Four trends had concentrations of anomalies but the largest was clearly associated with the Tangshan Fault. Except for the distribution of anomalies along the Tangshan Fault, all of the other above mentioned trends of anomalous areas were coincident with faults showing high levels of seismic activity prior to the Tangshan earthquake.

16, 22, 23 August 1976 Songpan Earthquakes (M=7.2, 6.7, 7.2)

This series of earthquakes occurred on the Tiger Tooth Fault which is an offshoot of the Dragon Gate Mountain faulting belt of western Sichuan. The focus of little attention because of the Tangshan earthquake that occurred three weeks before it, the first event of the series is the largest earthquake not preceded by foreshocks to have been successfully predicted within a few days. While the medium term prediction was based primarily on regional seismicity patterns (as well as some strain and radon anomalies), the imminent prediction was in a large part based on reported macroscopic anomalies. These anomalies included well water changes, animal anomalies, earth noises, gas bubbles in ponds and rice paddies and fire balls (balls of fire approximately one foot in diameter, possibly composed of methane, that came out of the ground and burned for several seconds in the air) (Personal communication, Sichuan Provincial Seismology Bureau, 1979). These anomalies were distributed primarily along a fault in the Dragon Gate Mountain belt but not the fault on which the earthquakes occurred.

The Dragon Gate Mountain fault belt is composed of three right-lateral, northeast trending faults and is the eastern boundary of the Tibetan fault block of western China. Along the western side of the northern part of this fault belt are the north-south to north-northwest trending Minjiang and Tiger Tooth faults. The 1933 Maowen earthquake occurred on the Minjiang fault and 1976 Songpan earthquake sequence occurred on the Tiger Tooth fault. A first motion study of the Songpan events showed that the principal stress trended east-west. Although the left-lateral Tiger Tooth fault is much smaller than the right-lateral Dragon Gate Mountain fault belt, they could be considered conjugate as both are consistent with the same stress system.

The epicentral area had no short term or imminent precursors to the earthquakes until two or three days before the fist event. However, telluric current and radon anomalies were recorded for six or seven months prior to the mainshocks along the Dragon Gate Mountain fault belt. The most obvious anomaly was recorded at Guzan station which is located at the intersection of the three

major seismic belts of Sichuan and is thus considered to be at a sensitive location (Li, 1975). Even clearer were the macroscopic anomalies that were reported from March until 13 August almost all occurring along the Dragon Gate Mountain fault belt accompanied by both seismic and aseismic slip along one of the faults within the belt (Figure 4).

Three large anomalies appeared in wells located along the south-central section of this fault during March, April and May. These included changes in mineral content, muddying of the water and the appearance of gas bubbles. These occurred more than 200 km away from the eventual epicenter but as mentioned above slip may have been occurring along the fault at the time. Nearer in time to the earthquake were three periods of anomalous activity, 16 June to 30 June, 17 July to 28 July, and 4 August to 16 August in the south, central and northern sections of the Dragon Gate Mountain fault belt, respectively. Many types of anomalies as described above, were reported with 192 reports in the first period, 133 reports in the second and 866 reports in the third. (Abnormal behavior by large animals appeared only in the last period.) Thus the anomalies moved up this auxilary fault towards the eventual epicenters and increased in number as the time of the earthquake approached. Two days before the earthquake anomalies along this fault almost completely ceased. (This was in spite of the fact that because of the previous anomalies, the area targetted with imminent prediction issued on August 12 included the central Long Men Shan belt which would presumably make the local observation groups especially observant.) At that time, anomalies appeared for the first time since the fall of 1975 in the immediate epicentral area and continued to increase until the earthquake occurred, with more than 100 anomalies reported in that three day period.

One other precursor occurred on a fault other than the Tiger Tooth fault. Strain data showed an uplift of the Min Jiang fault, NW of the Hu Ya fault, for several years prior to the earthquake. There was a total of 310 mm of uplift along a 40 km long stretch of the fault from 1960 to 1975. No data was collected for the Tiger Tooth fault itself.

Discussion

From the above data, it appears that during the development and occurrence of earthqukes, the regional geologic structures, regional stress fields and earthquake precursors are all closely related.

First, although all of the above earthquakes were controlled by the boundary fault systems of the intraplate faulting blocks, none of the mainshocks occurred on the major faults themselves but rather on secondary faults conjugate to the main fault system, responding to the same stress system as the primary faults. It could be that the complexity of intraplate tectonics allows pecularities in regional tectonic conditions to play a large role in determining concentrations in the local stress field (and thus which fault is most likely to slip). In an area as complex tectonicly as northern China, this is a very important consideration.

Second, within a definite fault block area, the tectonic activity shares certain characteristics, primarily determined by that region's local stress field. Thus, within the area influenced by a given stress field, the tectonic activity is regionally determined and an individual fault cannot be said to be moving independently. Therefore, besides the mainshock plane itself, on which foreshocks, aftershocks and premonitory acitivity occur, other planes in the area can be influenced by the regional stress field, be they parallel or conjugate to the mainshock plane. Thus it seems that the precursor field could be larger than the epicentral area of the earthquake by being distributed along faults conjugate to the mainshock plane that intersect the epicentral area. Such a distribution of premonitory phenomena is possible for long and medium term precursors but is more clear for short term and imminent precursors. Looking at the tectonic conditions for an earthquake's development and occurrence, these phenomena could be explained by considering the stress field, tectonic complexities and seismicity of the region. Naturally, in the time immediately prior to an earthquake, the premonitory phenomena are overwhelming concentrated at the epicenter.

Third, migration of the precursory field is a very important

point. Movement of the field occurred before all three of the earthquakes in all cases, moving towards the epicentral area as the earthquake approached - but it is especially clear for the Somgpan earthquake. It could be that a local concentration of the regional stress field propagates throught the region - perhaps increasing in strength - until it is sufficiently strong and in a sensitive enough area to produce an earthquake.

Acknowledgements

This work was the first cooperative work between Chinese and American geoligists. We thank the Ministry of Education and the State Seismology Bureau of the People's Republic of China and the Committee on Scholarly Communication with the People's Republic of China of the National Academy of Sciences of the United States of America for arranging this exchange. We also thank the Seismology Bureaus of Sichuan, Liaoning and Shaanxi Province for helping us carry out field investigations of the sites of the Songpan-Pingwu, Haicheng, and 1556 Huaxien earthquakes. We also appreciate the help of the researchers, Xiang Hongfa, Guo Shunmin, Zhang Zhen, Tang Rongchang,and Zhung Yizhang.

References

1 Deng Qidong et al, A discussion on the source of model of the Haicheng earthquake, Scientia Geologica Sinica, No. 3, p.195-204, 1976.

2 Deng Qidong et al, On the tectonic stress field in China and its relation to plate movement, Seismology and Geology, Vol. 1, No. 1, p. 11-22, 1979.

3 Guo Shunmin et al, Discussion on the regional structural background and the seismogenic model of the Tangshan earthquake, Scientia Geologica Sinica, No. 4, p. 305-321, 1977.

4 Jiang Pu et al, The anomalous field change and structural mechanical conditions in the prepatory process of the Tangshan-Haicheng earthquake series, unpublished, 1979.

5 Jones, L. et al, A study of the Hiacheng foreshock sequence, in press, Journal of Seismology, 1980.

6 Wu Kaitong et al, Certain characteristics of the Haicheng earthquake (M=7.3) sequence, Acta Geophysica Sinica, Vol. 19, No. 2, p. 95-109, 1976.

7 Deng Qidong et al, A preliminary investigation of the epicentral stress field, seismogenic structure and developmental process of the Haicheng, Liaoning earthquake, unpublished, 1975.

8 The Haicheng Earthquake Work Brigade, A preliminary study of the Haicheng earthquake, Vol. III, Earthquake precursors, unpublished, 1975.

9 Zhu Fengming, et al, Macroscopic anomalies and their significance in the predictions of large earthquakes, International Symposium on Earthquake Prediction, Paris, France, 2-6 April, 1979.

10 Hebei Provincial Seismology Bureau, Short-term and imminent precursors of the Tangshan earthquake, unpublished, 1977.

11 Qin Qum, On the background and seismic activity of the M=7.8 Tangshan earthquake, Hebei Province of 28 July, 1976, Acta Geophysica Sinica, Vol. 19, No. 4, p. 259-269, 1976.

12 Zhao Yulin et al, Electrical resistivity anomaly recorded in and around the epicentral area prior to the Tangshan earthquake of 1976, Acta Geophysica Sinica, Vol. 21, No. 3, p. 181-190, 1978.

13 Chang Guomin et al, An analysis of the process of preparation and the medium-term precursors of the 1976 Tangshan earthquake (M=7.8), International Symposium on Earthquake Prediction, Paris, France, 2-6 April, 1979.

14 Chen Tianchang et al, Some characteristics of the seismicity of the Songpan-Pingwu earthquake of 16 August, 1976, International Symposium on Earthquake Prediction, Paris, France, 2-6 April, 1979.

15 Li Ping et al, Exploration of the seismo-geologic features of the Yunnan-West Sichuan regions, Scientia Geologica Sinica, No. 4, p. 308-327, 1975.

All of the above articles except 9, 13, and 14 are in Chinese.

Figure Captions

Figure 1. Map of the epicentral area of the Haicheng earthquake showing the major faults of the area, the mainshock and location of the aftershock zones. The faults are numbered 1 - Niuju-youyangou Fault; 2 - Jinshanling Fault; 3 - Shuangtaizi Fault; 4 - Jinzhou Fault; 5 - Dayanghe Fault; 6 - Ximu River Valley Fault; 7 - Zhuanghe Fault; 8 - Yalu River Fault.

Figure 2. Map of the epicentral area of the Haicheng earthquake showing the mojor faults of the area and the location of water anomalies at various times prior to the earthquake. Faults numbered as in Figure 1.

Figure 3. Map of the epicentral area of the Tangshan earthquake showing the mainshock and major aftershock epicenters and electrical and well water precursory anomalies.

Figure 4. Map of the epicentral area of the Songpan earthquake showing epicenters of the three mainshocks, major faults of the area, and the locations of the macroscopic anomaly clusters. The June cluster occurred in the (a) area, the 17-28 July cluster in (b) and the 4-14 August cluster at (c). The faults are numbered: 1,2, and 3 - the Long Men Shan Fault Belt; 4 - Huya Fault; 5 - Leishan Fault; 6 - Minjiang Fault; 9 - Xianshuihe Fault; 10 - Anninghe Fault. Towns and cities are given letters: C - Kangding (Guzan nearby); G - Guanxien; H - Minzhu; I - Jiangyou; J - Beizhuan; K - Pingwu; L - Songpan.

include
west line on A+B

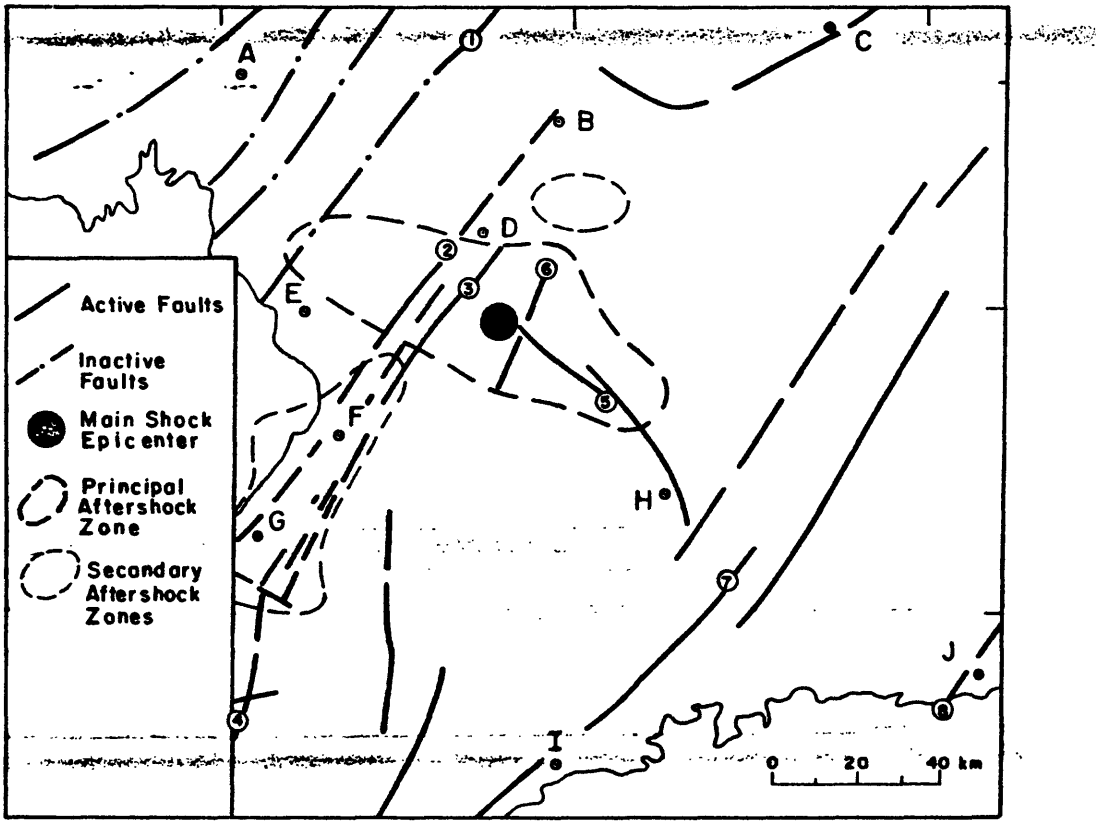

ment to USE, S in color,

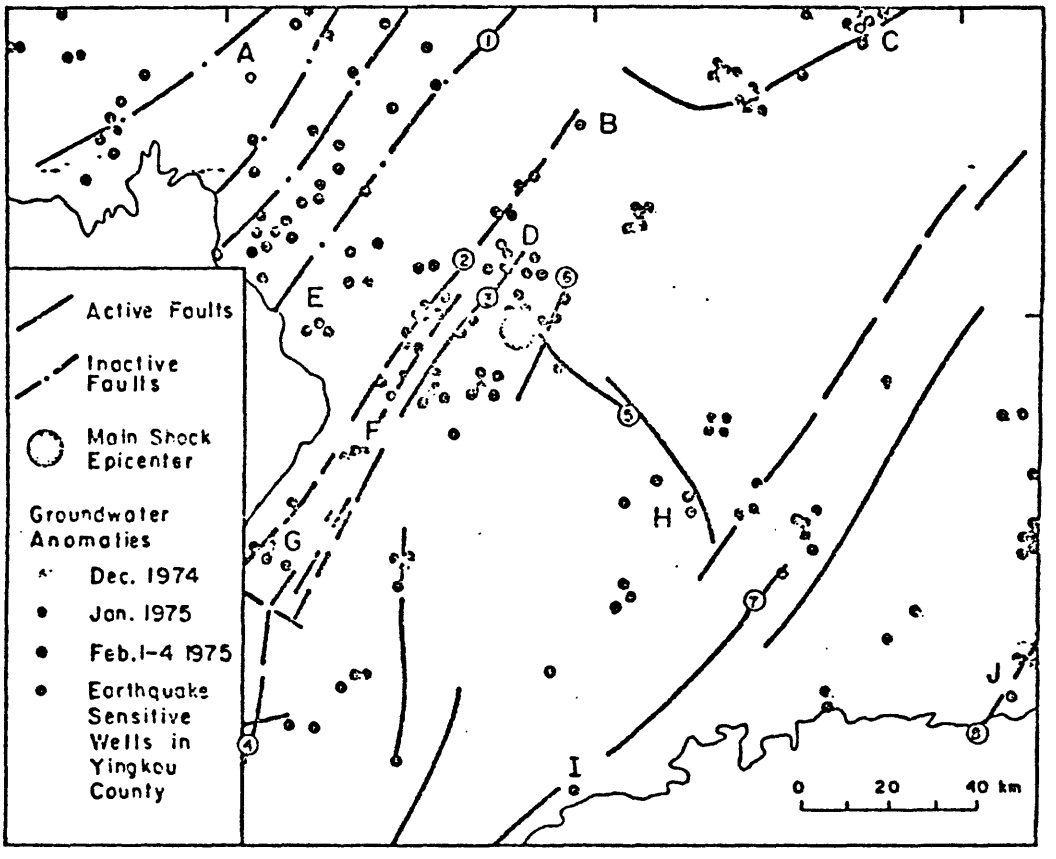

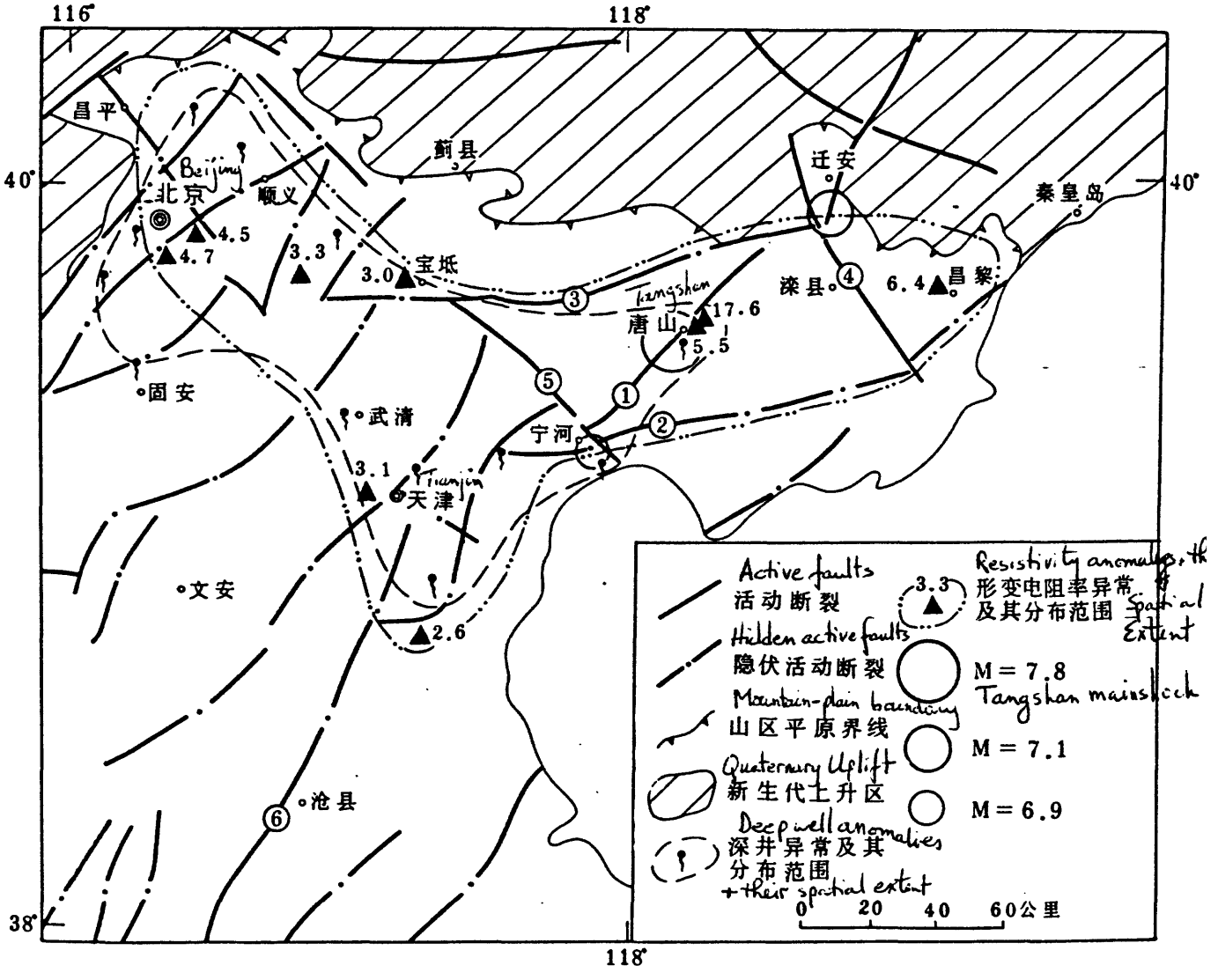

Tangshan Fault

① 唐山断裂；
② 宁河—昌黎断裂；
③ 丰台—野鸡坨大断裂；
④ 滦县—乐亭大断裂；
⑤ 蓟运河深断裂；
⑥ 沧东大断裂。

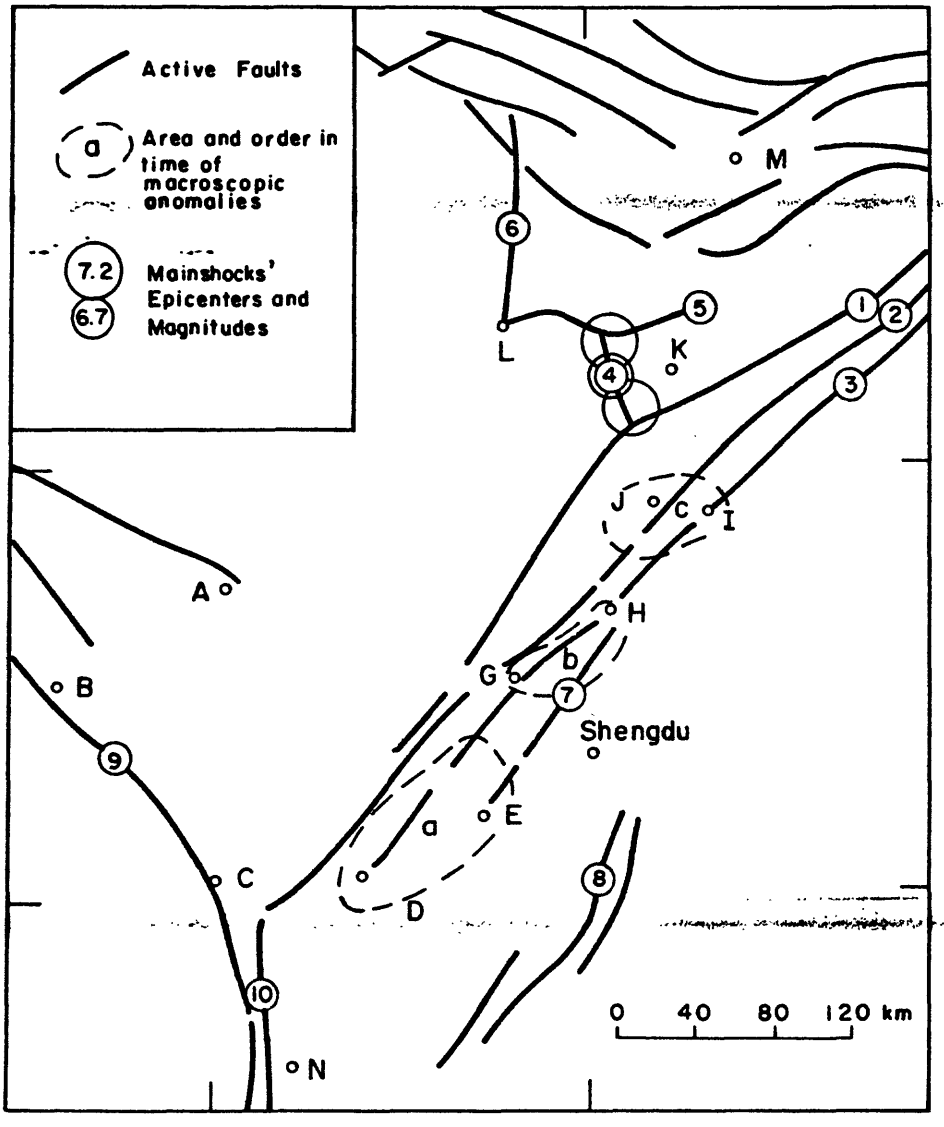
Active Faults
a
Area and order in time of macroscopic anomalies
7.2
6.7
Mainshocks' Epicenters and Magnitudes
M
L
K
J
C
I
A
H
B
G
b
Shengdu
a
E
D
C
N
0 40 80 120 km